UNIVERSITY OF COPENHAGEN

FACULTY OF SCIENCE

NIELS BOHR INSTITUTE

Ph.D. Thesis

Selective Area Growth Modes of Semiconductor Nanowire Networks and Defect Characterization

Martin Espiñeira Cachaza

Principal supervisor: Professor Peter Krogstrup Jeppesen

Co-supervisor: Researcher Elisabetta Maria Fiordaliso

Assessment committee:

Professor Jesper Nygård

Professor Jonas Johansson

Professor Ray LaPierre

September 2021

This thesis has been submitted to the
Ph.D. School of the Faculty of Science,
University of Copenhagen

Martin Espiñeira Cachaza

Selective Area Growth Modes of Semiconductor Nanowire Networks and Defect Characterization

Ph.D. Thesis

September 2021

Principal supervisor: Professor Peter Krogstrup Jeppesen

Co-supervisor: Researcher Elisabetta Maria Fiordaliso

University of Copenhagen

Faculty of Science

Niels Bohr Institute

Blegdamsvej 3B

2200 Copenhagen N

Abstract

This thesis presents results on the different selective area growth (SAG) modes of in-plane III-V semiconductor nanowire (NW) networks, their modelling and their structural characterization. SAG networks are candidates to become a scalable hosting platform of a universal quantum computer based on the topologically protected qubit. Challenging requirements are demanded for this approach, such as the reproducible growth of homogeneous NW networks and very low density of crystal defects.

The first part of the thesis explores the different growth modes arising during SAG and their impact in NW material incorporation. The transition that defines the growth mode during SAG is the sign of the flux of adatoms between the mask and crystal $\Delta\Gamma_{a_m a_c}$. SAG growth modes are experimentally observed and defined as source if $\Delta\Gamma_{a_m a_c} < 0$, sink if $\Delta\Gamma_{a_m a_c} > 0$ and balance if $\Delta\Gamma_{a_m a_c} = 0$. These growth modes affect the incorporation of NWs in arrays and their faceting. Two proposals for the growth of reproducible arrays of NWs are presented: a fine compensation of growth modes on buffer layers and to increase the number of structures around the transport NWs creating an adatom density saturation region. In addition, two models are presented based on mass conservation and coupled diffusion equations, predicting the observed experiments.

The second part studies the defects appearing in SAG NWs and a new characterization technique to observe them. DFT calculations are performed on InAs, suggesting a mild effect of stacking faults in the semiconductor properties and a more detrimental effect of dislocation cores, which introduce electron states in the band gap. It is also developed a new characterization technique based in electron channeling contrast SEM, using the design properties of the

immersion lens and allowing for a high resolution characterization of NW stacking faults.

In summary, the findings presented expand the understanding of the SAG mechanism, the effect on the semiconductor of the defects generated and a new way of observing them. Although this helps to accomplish some of the material requirements for a topological qubit, more optimization needs to be performed in the defect reduction of the structures.

Dansk Resume

Denne afhandling præsenterer resultater vedrørende forskellige typer af selektive områdedyrkning (SOD) af III-V nanowires (NWs) i planet, deres modellering og deres strukturelle karakterisering. SOD-netværk er udpeget som kandidat til at agere skalerbar platform for en universel kvantecomputer baseret på topologisk beskyttede qubits. Der sættes udfordrende krav til denne tilgang, såsom reproducérbar dyrkning af homogene netværk af NWs og meget lav densitet af krystaldefekter. Krystal desorganisering genereret af inhomogeniteter og defekter har vist sig at have ødelæggende indvirkninger på qubitydeevne og forstyrrer de topologiske faser, der er nødvendige for at udføre beregninger.

Den første del af afhandlingen undersøger de forskellige vækstyper, der opstår under SOD og deres indvirkning på NW materialeindkorporering. Den vigtigste overgang, der definerer vækstypen under SOD, er fortegnet på fluxen af adatomer mellem masken og krystallen ($\Delta\Gamma_{a_m a_c}$). SOD-vækstilstande observeres eksperimentelt og defineres som 'kilde', hvis $\Delta\Gamma_{a_m a_c} < 0$, som 'dræn' hvis $\Delta\Gamma_{a_m a_c} > 0$ og i ækvilibrium hvis $\Delta\Gamma_{a_m a_c} = 0$. Disse vækstyper påvirker materialeinkorporering i NWs positioneret i matricer og deres facetter. To forslag til dyrkning af reproducerbare matricer af NWs præsenteres: en fin kompensation af vækstype på bufferlag og for at øge antallet af strukturer omkring NWs, hvilket skaber en adatom densitetsmætningsregion. Derudover etableres to modeller baseret på analytisk massebevaring og koblede diffusionsligninger, der forudsiger de eksperimentelle tendenser.

Den anden del studerer effekten af de observerede defekter, der forekommer i SOD NWs og en ny karakteriseringsteknik til at observere dem. DFT-beregninger udføres på InAs, der indikerer en mild effekt fra stablingsfejl på

halvlederegenskaberne og en mere skadelig indvirkning af dislokationskerner, som introducerer elektrontilstande inde i båndgabet. Der er også udviklet en ny karakteriseringsteknik baseret på 'elektronkanaliseringskontrast'-SEM, der anvender nedsænkningslinsens egenskaber og muliggør karakterisering af NW-stablingsfejl i høj opløsning.

Sammenfattende udvider de præsenterede resultater forståelsen af SOD-mekanismen, defekters indvirkningen på halvlederen og en ny måde at observere dem på. Selvom dette bistår med at opfylde nogle af materialekravene til en topologisk qubit, skal defektreduktionen i strukturerne optimeres yderligere.

Acknowledgements

First I want to thank Peter Krogstrup for giving me the opportunity of doing both my master and PhD thesis in this world-class group. This has been the best possible place to launch my career and I am very grateful for that.

These 3 years journey would have been impossible without the great daily support, patience and understanding of the other PhD fellows in the group: Gunjan, Harry, Steffen and Tobias. My friends. You are one of the most valuable things I take with me from the PhD.

Some work that is usually unnoticed is the great support that the administrative team in QDev offers. Thanks to your dedication, quick action and availability the academic people can focus entirely in the research. A thing that I will for sure miss are the coffee breaks and chats together with QDev people like Joachim, Lukas and Sabbir. Special thanks to Mohana and Jordan from the MQML team for all the support, help and nice words. I will also take you with me from the PhD. I had the privilege to learn all the characterization techniques that I know thanks to great people like Erik Johnson, Jordi and Sara from the Barcelona team and Elisabetta Fiordaliso, Alice Fanta and Jens Kling from DTU.

Looking back at my whole academic life, I feel particularly thankful to the teachers that vocationally spend time and effort teaching with pasion. Among all the teachers that I had, there are only a few of them that really made an impact in my life with their enthusiasm and way of explaining things. Thank you so much Elena Navarro, Jose Miguel García, Yves Huttel, Julio, Begoña and Luis Alfredo Caro for sparkling my curiosity about physics and science.

Last and most important. Thanks to my family for supporting me during this 11 years long trip, for celebrating my victories and upholding in my defeats. Thanks to my friends in Madrid, *Los Chavales*, for having always been with me even after a long period without seeing each other. It will be needed something bigger than a pandemic to destroy our life-time friendship. Finally, the biggest thank you to my partner in life: María. I realised in this time how lucky I am by having you by my side.

You all make me as a person, this thesis is also yours.

List of Publications

This thesis uses results from the following publications:

1. **Martin Espiñeira Cachaza**[*], Anna Wulff Christensen[*], Daria Beznasyuk, Tobias Særkjær, MortenHannibal Madsen, Rawa Tanta, Gunjan Nagda, Sergej Schuwalow and Peter Krogstrup. "*Selective Area Growth Rates of III-V Nanowires*". Physical Review Materials, 5, 9, 094601, 2021

2. **Martin Espiñeira Cachaza**, Ribka Balakrishnan, Alice Bastos da Silva Fanta, Marco Beleggia, Peter Krogstrup and Elisabetta Maria Fiordaliso. "*Inmmersion Mode Assisted Electron Channeling Contrast Imaging*". In preparation.

3. Dominik Gresch, Rafał Rechciński, **Martin Espiñeira Cachaza**, Dmitry Pikulin and Georg W. Winkler. "*Twin Planes and their Terminating Dislocation Cores in InAs – Effects on Transport and Charge Disorder*". In preparation.

4. Sabbir A. Khan, Charalampos Lampadaris, Ajuan Cui, Lukas Stampfer, Yu Liu, Sebastian J Pauka, **Martin Espiñeira Cachaza**, Elisabetta Maria Fiordaliso, Jung-Hyun Kang, Svetlana Korneychuk, Timo Mutas, Joachim E Sestoft, Filip Krizek, Rawa Tanta, Maja C Cassidy, Thomas Sand Jespersen and Peter Krogstrup. "*Highly Transparent Gatable Superconducting Shadow Junctions*", ACS Nano, 14, 11, 14605–14615, 2020.

5. Yu Liu, Saulius Vaitiekenas, Sara Marti-Sanchez, Christian Koch, Sean Hart, Zheng Cui, Thomas Kanne, Sabbir A. Khan, Rawa Tanta, Shivendra Upadhyay, **Martin Espiñeira Cachaza**, Charles M Marcus, Jordi Arbiol,

Kathryn A Moler and Peter Krogstrup. "*Semiconductor-Ferromagnetic Insulator-Superconductor Nanowires: Stray Field and Exchange Field*", Nano Letters, 20, 1, 456-462, 2019.

List of Figures

Contents

1 Introduction

The history of modern semiconductor devices starts with the invention of the point contact transistor by Bardeen and Brattain, in 1947 at the Bell laboratories [1]. Their revolutionary idea, together with the previous contributions from Shockley, got patented the same year [2] and the three of them became Nobel laureates soon after for this invention and its potential applications. Since then, humanity has witnessed the period of highest technological development in its history.

The next milestone achieved in the semiconductor devices field was the invention of the metal-oxide semiconductor field-effect transistor (MOSFET) by Atalla and Kahng [3, 4], in 1960 also at the Bell laboratories. The building materials and layers design of the MOSFET allowed a higher scalability and mass production, together with a low consumption and reliable operability [5]. The first strategy used to increase the power of MOSFET circuits was the miniaturization of the transistor [6], increasing the density per chip area. In 1961, Noyce contributed to this approach by introducing the concept of monolithic integrated circuit (microchip), an idea that also got patented due its high commercial potential [7]. This approach allowed to improve from the first model chips containing several transistors, up to billions in the modern ones.

In 1964, Moore predicted the exponential growth of the number of MOSFETs contained in microchips, doubling up every two years [8]. To this day, Moore's predicted exponential growth has been achieved thanks to the development and improvement of the chip fabrication techniques used to massively and

accurately fabricate the newer generations of MOSFETs [9]. However, due to the fast improvement of these techniques, the field is reaching a physical inherent limitation on scaling down the size of the transistors. If the MOS gate width becomes < 9 nm or its oxide layer < 2 nm the electrons can transmit between source and drain even if they have an energy lower than the voltage applied to the gate, due to quantum tunneling [10, 11]. In this scenario, it is impossible to control the transitor's states in a reliable way, impeding any useful calculation. Some solutions to overcome this limitation have been proposed, like tunnel FETs or devices that compute with magnetic dipoles (spintronics) [12].

To this date, the most advanced transistor technology is the "2 nm node" from IBM which stacks up transistor electron channels completely surrounded by the metallic gate [13]. Although the gate width is still > 9 nm, it allows to pile up a higher density of transistors per chip [14] and considerably reduce the chip energy consumption [15]. Other approaches improve the performance of microchips while maintaining the transistor size, by using artificial intelligence driven design of more efficient chips networks [16]. However, the approach to the classical transistor's theoretical limit and the lack of new revolutionary designs [17] only postpone the date of Moore's law failing, inevitably leading to a stagnation of the computer power increase.

1.1 Why Quantum Computing?

The scenario of the end of Moore's law was envisioned decades ago by Feynman [18] and Deutsch [19]. They concluded that the only known solution to keep the computational power exponential growth in force was to create a quantum transistor (qubit) that makes use of the quantum theory and its benefits. With a universal fault-tolerant quantum computer we could address problems and challenges that otherwise would be impossible with classical super computers, like: prime factoring [20], materials development [18, 21] or database search [22], among other potential applications. The requirements needed for such qubit to be useful are detailed in DiVicenzo's criteria list [23]:

1. A scalable physical system with well defined states.
2. The ability to restart the qubit.

3. Decoherence times larger than operation times.
4. Any operation can be performed by a finite sequence of gate operations.
5. Ability to read out the qubit states.

There are different approaches on how to build such a transistor. Each of them use a different physical platform to generate the embodiment of the qubit which are typically a two energy levels system, such as: ground and excited state of an atom, spin up or down, vertical and horizontal light polarization... The basis of the most used qubit platforms are: linear optics [24], the spin of impurities [25, 26], trapped ions [27, 28], superconducting circuits [29, 30] and topological states [31, 32]. Each platform has its pros and cons.

Recently, in an experiment conducted by the Google Artificial Intelligence department, they claimed to solve with their 53 superconducting qubit chip prototype a problem that would require years to solve in a classical supercomputer [33]. Although IBM later refuted these results for not being completely accurate [34], this milestone set the start of the quantum supremacy era. The biggest challenge about multi qubit superconductor chips are their typically low coherence times. This makes them prone to computing faults causing a qubit fidelity below the required operation threshold [35]. Solutions like software error correction have been demonstrated useful to correct faults and bring fidelity to very high values [36]. However, this is no longer applicable when the number of qubits on a chip is increased to outperform Shor's algorithm [37].

The topologically protected qubit approach was first proposed by Kitaev [38]. Among its remarkable benefits compared to other qubit approaches, it would be protected against errors caused by the perturbations generated in the local environment [39, 40]. This is possible due to the generation of an energy gap separated from the rest of the spectrum where degenerate zero energy ground states can exist, making the qubit states immune to decoherence and imprecise gate operations [41]. Majorana Zero Modes (MZM) emerging in solid state platforms are exotic neutral excitation quasi-particles that are bounded to zero energy due to its electron-hole symmetry [42]. As a consequence of their nature, they obey non-Abelian statistics, which is a key requirement for topological quantum computation [41].

1.2 III-V Semiconductor Nanowires

Fu predicted in 2008 that MZMs would appear in topological superconductors, formed by an ordinary s-wave superconductor proximitized to the surface of a semiconductor [43]. Soon after, this approach was extended to any 1D semiconductor-superconductor hybrid system that fulfills the following requirements: high semiconductor Rashba spin-orbit coupling, high semiconductor Landé g-factor, a superconductor providing proximity effect and an in-plane magnetic field applied to the structure [44]. These hybrid heterostructures have been developed and optimized since then with multiple types of semiconductors, superconductors and platform geometries [45–49]. Most of the semiconductors used for these hybrid structures are III-V semiconductor nanowires (NWs) due to their useful bulk properties that fulfill the requirements, high electron mobility, direct band gap and the already developed techniques to grow such structures [50].

The three most used methods to grow III-V NW platforms for topological quantum computation are: vapour liquid solid (VLS), selective area growth (SAG) and 2 dimensional electron gases (2DEG). Each of them offer advantages and disadvantages towards their implementation in potential qubit based devices. VLS is a mature platform [51, 52] used for proof of concept experiments, although its drawbacks are the lack of scalability and the difficulty defining superconductor junctions [53]. Although the SAG method has been studied decades ago [54, 55], it has recently gained more attention due to its potential for qubit platform, intrinsic scalability and hard confinement of electron states [49, 56, 57]. 2DEG offers offers good quality of semiconductor growth with a top down definition of NWs, although with a general lower state confinement [58, 59].

One of the most promising NW designs to host and do computation with MZMs protected from quasiparticle poisoning was proposed by Karzig et al. in 2017 [60]. These networks of semiconductor NWs and quantum dots with superconductor depositions, called "hexons", could form the building block of an scalable universal quantum computer and they can be built with crystal growth mechanisms that we have nowadays.

1.3 Thesis Structure

SAG of III-V NWs is a candidate platform to grow and fulfill the requirements described by Karzig et al. for the hexon network based topological qubit [60]. This thesis focuses on the study of SAG growth modes, their implications on the incorporation of material into the arrays of NWs, the impact of crystal defects into the semiconductor quality and the development of a scanning electron microscopy (SEM) defect characterization technique.

Figure 1.1 shows the optimization loop workflow used for the development of the III-V semiconductor NWs presented in the following chapters. The results contained in this thesis live in the post-growth characterization and data analysis bubbles. Samples grown by molecular beam epitaxy (MBE) are received from a crystal grower, characterized with different techniques and the obtained data is analyzed to understand the outcome of a sample, to feed the loop again starting in the pre-growth fabrication of new samples to be grown.

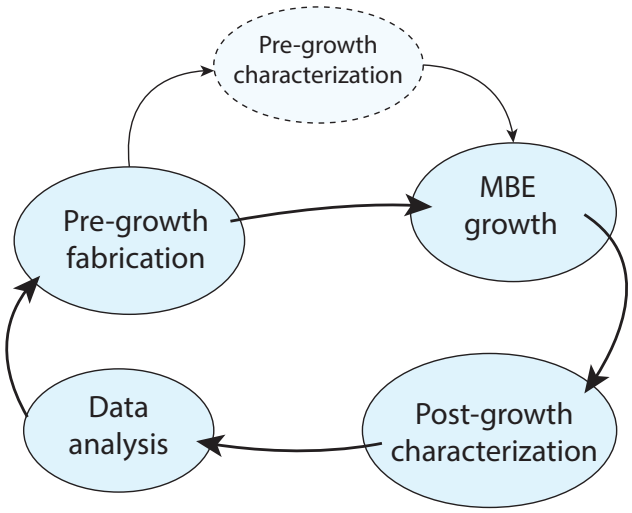

Figure 1.1.: Material optimization feedback work loop.

Chapter 2 describes the basics of III-V semiconductor crystals and the MBE growth method in order to understand the mechanisms that govern the growth of VLS and SAG NWs.

Chapter 3 describes the pre-growth fabrication processes performed on the III-V semiconductor substrates used to grow SAG NWs by MBE. It also reports

on the post-growth characterization techniques used for the analysis of the studied SAG NWs. Daria Beznasyuk, Rawa Tanta, Dmitrii Viazmitinov and Gunjan Nagda collaborated in the substrate fabrication flow.

Chapter 4 focuses on the description of SAG adatom kinetics and the impact they have on material incorporation. The chapter also describes the different SAG growth modes arising from adatom kinetics. Two growth simulation models are presented, one based on adatom diffusion coupled equations and other in an analytical approach of NW growth incorporation. These models are developed to describe the results obtained from experiments. The SAG growths discussed in this chapter were grown by Daria Beznasyuk, Rawa Tanta and Mohana Rajpalke. This chapter contains NWs of different III-V semiconductor compositions and grown on different substrates.

Chapter 5 focuses on crystal defects appearing in SAG NWs. The first part is about the DFT calculations performed to model the influence of certain defects on quantum transport through such NWs. The second part describes a new electron microscopy characterization technique developed for a faster characterization of the defects presented in the first part of the chapter.

Chapter 6 concludes the thesis with an outlook and an overview of the future steps in the field, based on the results presented.

2 Crystal Synthesis

The overlapping parts from this chapter with Publications 4 and 5 (references [48] and [61]) are adapted with permission of the American Chemical Society, Copyright 2020.

III-V semiconductors are a family of materials made of group III and group V elements that show semiconducting properties. Nowadays, they are synthetically produced for a wide variety of applications in epitaxial growth setups like liquid phase epitaxy [62], metalorganic chemical vapour deposition [63] and MBE [64]. The two main crystal structures that these semiconductors show are space group $F\bar{4}3m$ zincblende (ZB) and space group $P6_3mc$ wurtzite (WZ).

This chapter presents the crystallographic structure and the growth mechanisms used for the synthesis of the III-V semiconductors shown in this thesis.

2.1 Crystallography of III-V semiconductors

Bulk III-V semiconductors show a ZB bulk crystal structure, except some III-nitrides having a WZ strucutre [65]. Figure 2.1 shows the crystal unit cell of a GaAs ZB crystal structure. The atomic arrangement is equivalent to the double base FCC diamond structure, but substituting the two C atoms by a group III and a group V atom. The crystal structure was computed on the freeware Vesta [66].

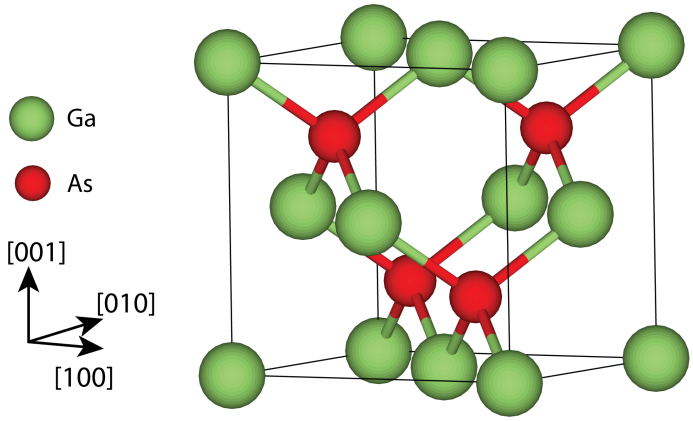

Figure 2.1.: Crystal unit cell of GaAs ZB F$\bar{4}$3m structure.

ZB crystal growth can be understood as a stacking sequence of $\{111\}$ close packed planes. Figure 2.2 shows the stacking sequence of (111) planes, in a top-view (111) zone axis perspective. For visualization purposes, each of the spheres represents a group III and group V atomic dimer.

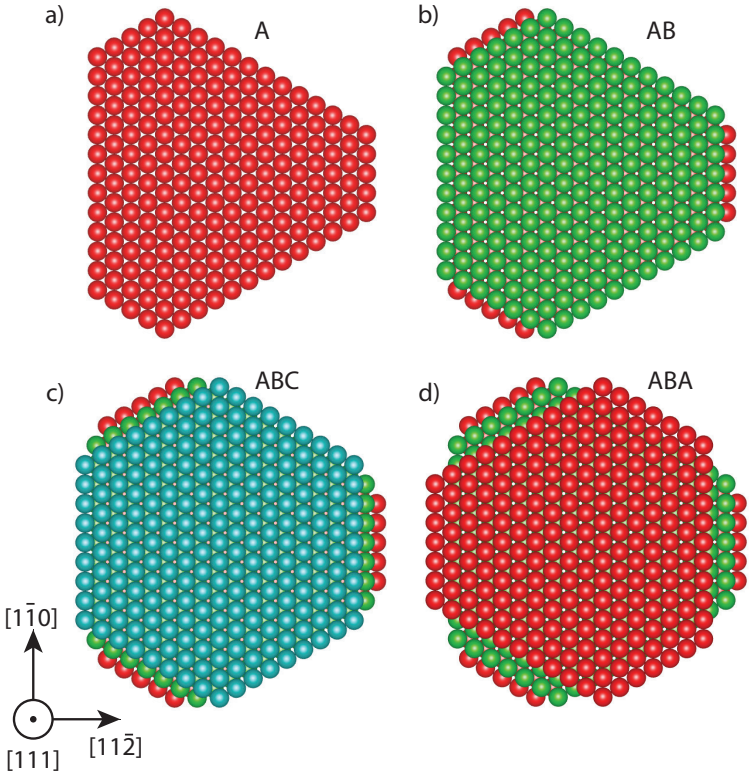

Figure 2.2.: Stacking sequence of (111) ZB planes, considering the III-V dimers as spheres. a) (111) as an "A" plane in the stacking sequence. b) "B" (111) atomic plane (green) on top of the "A". c) "C" (111) atomic plane (blue) making the whole ZB stacking sequence. d) Example of an ABA sequence, where the top "A" plane is an stacking fault.

Figure 2.2a shows a top view (111) plane along the $[111]$ zone axis, defined as "A". Figure 2.2b shows a second (111) plane, defined as "B" displaced a distance $a/6 < 11\bar{2} >$ with respect of "A". Figure 2.2c describes the complete ZB stacking sequence, where a "C" plane is placed on top of "B", displaced $a/3 < 112 >$ from the original "A". Thus, a ZB crystal can be described as a correct piling of (111) planes following the stacking sequence ABCABCABC... Figure 2.2d shows a typical coherent crystal defect appearing in ZB structures, called stacking fault. A plane deposited on top of "B" at the same position than the original "A" is a fault in the stacking sequence. If the ZB on the ABAB stacking continues with the intended sequence ABABCABC, the first four planes generate a region in the crystal with similar crystal structure than the hexagonal WZ (ABABAB...).

2.2 Molecular Beam Epitaxy

The samples presented in this work are grown by MBE in a Varian GEN II system. MBE is a versatile crystal growth technique for semiconductor epitaxial layers. Its low pressures of $\sim 10^{-10}$ Torr allows to control very precisely the growth compositions, doping profiles and sharp layer interfaces [64].

In order to maintain such a high purity inside the system, a series of interconnected chambers are needed. The first chambers allow to clean the introduced sample from any remaining humidity or impurity from the pre-growth fabrication process. A bake-out process is performed to the sample and sample holder before opening the gate that connects to the rest of the MBE, until a low pressure level of $\sim 10^{-10}$ Torr is achieved. Before growth, it is also needed to remove the native oxide layers from the surface of the III-V semiconductor substrate. For this purpose, H_2 plasma cleaning is used in the high-end MBE systems [67]. At this point, the substrate can enter the MBE chamber for growth. Figure 2.3 shows an sketch of the parts that conform a MBE chamber.

Inside the MBE chamber, the growth substrate is placed in a rotating sample holder that heats the substrate up to the required growth temperature T_{sub}. Effusion cells are heating systems containing elements of high purity, that generate the flux f of atoms that will reach the substrate for crystal growth. The equivalent pressure of this flux of atoms can be controlled very precisely

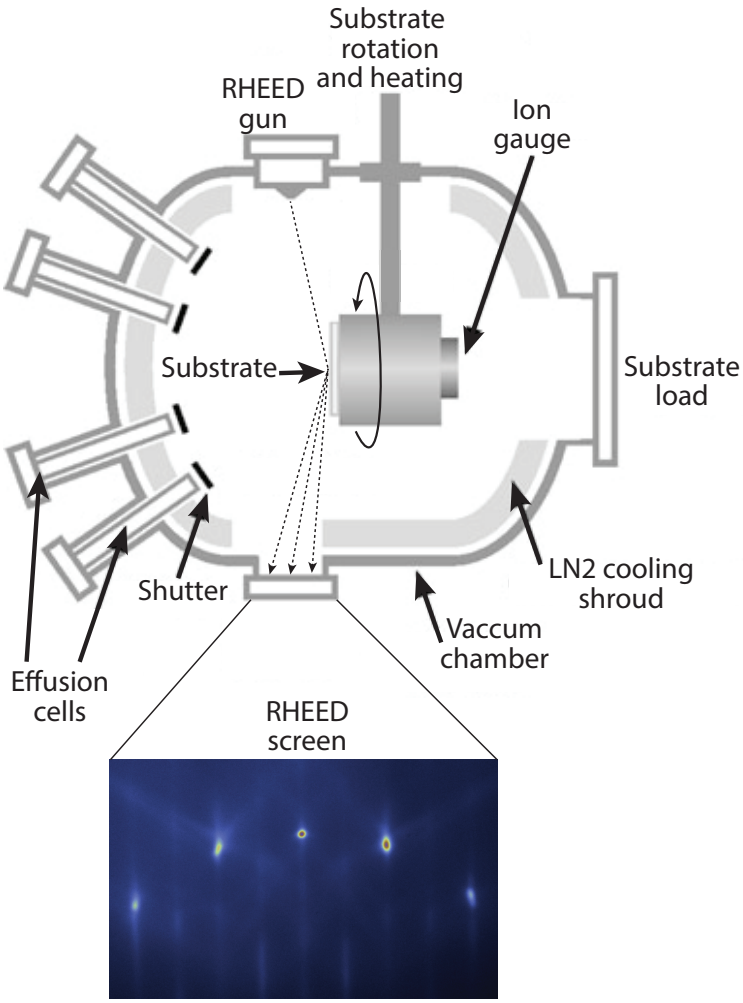

Figure 2.3.: Sketch of the different components that make up a MBE system, similar to the one used for the growth of the samples presented in this work. The RHEED pattern shows an InAs(001) (2x4) surface reconstruction along the [110] crystallographic orientation. MBE sketch adapted from reference [68].

with the ion gauge placed at the back of the substrate holder. Reflective High Energy Electron Diffraction (RHEED) is a system in MBEs that allow to monitor the state of the growth. Consisting in an electron gun pointed at a grazing angle on the substrate, a phosphorus screen detects the level of monolayer termination occurring on a big area of the sample with the so-called RHEED oscillations [69]. A LN2 cooling shroud is installed at the walls of the ultra high vacuum chamber that acts as a cold trap, improving the vacuum level and adsorbing all the remaining atoms that are not absorbed by the sample. This generates temperature gradients of hundreds of °C within the chamber, to offer the cleanest possible growth conditions with atomic flux mean free paths of $\sim$ 1 m [70].

2.2.1 Adatom kinetics

Atoms coming from effusion cells impinge on the substrate and get adsorbed on the surface, becoming adatoms. Adatoms diffuse on the crystal growing surface until desorbing back to vapour phase, being captured on a growing island or meeting other atoms to nucleate. All these processes heavily depend on thermodynamic quantities such as Gibbs free energy, chemical potentials and surface energies [71]. The termination of the adatom state on the crystal is defined by the desorption lifetime τ_{av} and the incorporation to the solid crystal lifetime τ_{as}. Depending on which of these two lifetimes is bigger, the adatoms will perform preferential transitions to vapour or solid. In general, lifetimes can be expressed as:

$$\tau = \frac{1}{c_\tau \cdot \exp\left(-E_\tau / \left(k_B T_{sub}\right)\right)}, \tag{2.1}$$

where c_τ is the atomic surface vibration frequency and E_τ is the activation energy required for the adatom to perform the transition. Depending on T_{sub} and the activation energies for incorporation E_{ac} and desorption E_{av}, adatoms are incorporation limited if $\tau_{av} > \tau_{as}$ and desorption limited if $\tau_{av} < \tau_{as}$. This implies that the general adatom lifetime on an surface is $\tau^{-1} = \tau_{ac}^{-1} + \tau_{av}^{-1}$.

Adatom diffusivity D is a quantity related to the mean displacement of the adatoms diffusing on a substrate. It can be expressed as:

$$D = c_D \cdot \exp\left(-E_D / \left(k_B T_{sub}\right)\right), \tag{2.2}$$

where c_D is a pre-exponential constant depending on available neighbour diffusion states, adatom density and the Zeldovich factor [72], and E_D is the activation energy of the transition. Then, adatom diffusion length λ can be described as

$$\lambda = \sqrt{D\tau} = \lambda_0 \cdot \exp\left(\left(E_\tau - E_D\right) / \left(2 k_B T_{sub}\right)\right), \tag{2.3}$$

where λ_0 is effectively an elementary jump distance gathering the rest of pre-exponential factors.

However, adatom incorporation to crystal phase is not only dictated by τ_{ac} but also to the local structure of the substrate plays a role. Crystal steps, terraces

and kink sites have an effect on adatom nucleation by modifying the local surface energy. Kink sites and steps are the positions on a surface crystal where adatoms nucleate more easily at, having a higher number of nearest neighbours than terraces. The Ehrlich-Schwoebel barrier generated at crystal steps also act as preferential nucleation sites for adatoms, promoting a layer by layer type of growth at the right f and T_{sub} conditions [73].

2.2.2 Growth modes in MBE

MBE growth of epitaxial crystals for electronic device purposes usually requires the growth of homogeneous layers. However, it is not straightforward to achieve such high film quality for a given MBE flux and T_{sub}. The homogeneity depends on the relative surface energies between the substrate, nucleus and vapor phases, having an influence on the wetting angle of the nucleus. The contact angle between the nucleus and the substrate can be expressed as $\cos\Theta = (\gamma_{vs} - \gamma_{ns})/\gamma_{vn}$, where γ_{vs} is the surface tension between the vapour and the substrate phases, γ_{ns} between the nucleus and the substrate phases, and γ_{vn} between the vapour and nucleus phases.

The relation between γ_{vs}, γ_{ns} and γ_{vn} determines the growth mode of the epitaxial layers. Figure 2.4 shows the three different growth modes achieved by MBE. For the case of $\gamma_{vs} > \gamma_{ns}+\gamma_{vn}$, the growth layer can wet completely the substrate, allowing a 2D growth mode. This desired growth condition, called Frank - Van der Merve, is described in figure 2.4a. If the surface energy of the nucleated adatoms and the substrate is larger than the others $\gamma_{ns} > \gamma_{vs} + \gamma_{vn}$, the layer does not wet the surface of the substrate leading to a 3D growth. This growth regime is called Volmer-Weber and it is represented in figure 2.4b. For any other intermediate relation between the surface energies, the growing layer will show a mix behaviour by growing layer by layer and 3D islands on top, called Stranski - Krastanov and described in figure 2.4c.

2.3 Vapour Liquid Solid

More sophisticated MBE growth methods were developed decades ago, like the vapour-liquid-solid (VLS) method [74]. This method allows to grow high

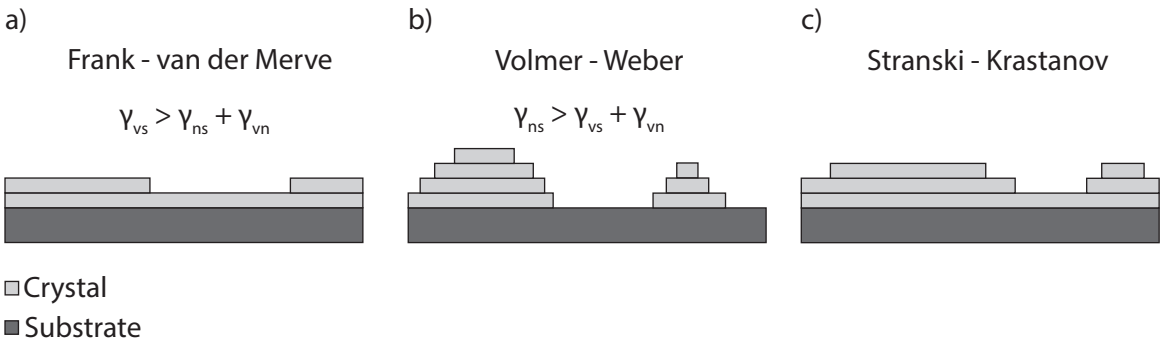

Figure 2.4.: Sketch of the three growth modes in MBE. a) Frank - van der Merve. b) Volmer - Weber. c) Stranski - Krastanov.

crystal quality free-standing NWs on substrates by using a catalyst nano-droplet. Usually made of Au, the droplet becomes liquid at the growth temperatures and starts absorbing the precursor fluxes (vapour) until it reaches a supersaturation state. Using substrates with a (111)B orientation out of plane that will be inherited by the NW, the droplet nucleates a circular monolayer of the growing species with the same diameter as the original melted droplet. By repeating this process, a vertical NW is grown along the (111)B direction of the same composition as the precursor fluxes.

The VLS method offers the possibility of tuning the crystal structure of the resulting NWs between ZB and WZ, even on semiconductor materials that do not show a stable WZ bulk structure, like as InAs and GaAs. The determining parameter of the crystal structure is the contact angle of the triple phase: between Au droplet, the vapour and the solid phases [75]. It can be achieved by changing the supersaturation conditions and the V/III ratio of precursor pressures.

Due to the intrinsic limitation of the growth direction of the NWs, recent improvements on VLS growth have been developed to realize superconductor junctions on semiconductor NWs. The use of different out of plane orientation substrates allows to perform selective etch of (111)B planes to grow NWs from there [48, 53]. Figure 2.5a shows a SEM image of an array of $InAs_{0.3}Sb_{0.7}$ NWs growing from selectively etched $\{111\}$B planes, on an InAs(001) substrate. By properly designing the geometry of the arrays, NWs will grow next to each other allowing to shadow the deposition of Al and generating junctions, as shown in figure 2.5b.

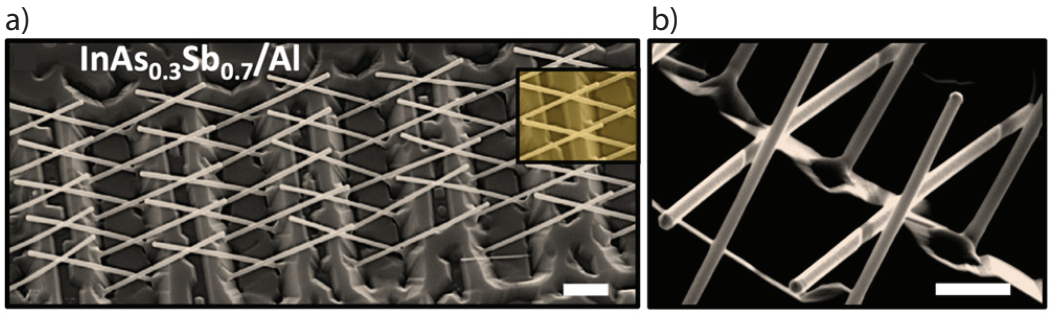

Figure 2.5.: VLS method for fabricating in situ Al shadow junctions on NWs. a) SEM images of $InAs_{0.3}Sb_{0.7}$ NWs grown in selectively etched (111)B trenches on InAs(001) substrate. b) High magnification view of pairs of NWs used to create Al shadow junctions along one side of the NW. Scale bars are 100 nm. Figure adapted from Publication 4 with permission from American Chemical Society, Copyright 2020.

The quality of the junction generated by the shadowing approach is dependent on the relative distance between the shadowed and shadowing NWs, l_s. Figure 2.6a and b are atomic force microscopy (AFM) images showing two $InAs_{0.3}Sb_{0.7}$ NWs with Al shadow junctions deposited at $l_s > 500$ nm and $l_s < 250$ nm, respectively. The quality of the smaller l_s junction is better with no Al islands. Figure 2.6c is a high resolution transmission electron microscope (HR-TEM) image of the junction presented in 2.6b. The Al thickness shows a spread over a distance Δ_b, caused by a not completely directional flux of Al during the deposition. The inset shows the perfect epitaxy between the $InAs_{0.3}Sb_{0.7}$ and the Al.

VLS can be used as platforms to explore the deposition of stacks of materials, creating exotic combinations such as ferromagnetic insulator, superconductor and semiconductor NWs [61]. The ferromagnetic insulator effect on this composite of materials is expected to supply the Zeeman splitting needed to develop a superconducting topological phase, instead of using an external magnetic field [76]. Figure 2.7 shows SEM and HR-TEM images of such a NW stack of materials, using EuS as ferromagnetic insulator, Al as superconductor and InAs semiconductor WZ NWs. In figure 2.7c the epitaxial match between the three different materials is observed.

VLS growth of NWs is a reliable way to grow low density defect structures and to explore new material combinations. However, the main limitation of the VLS method is the scalability and the design constrictions. As mention in

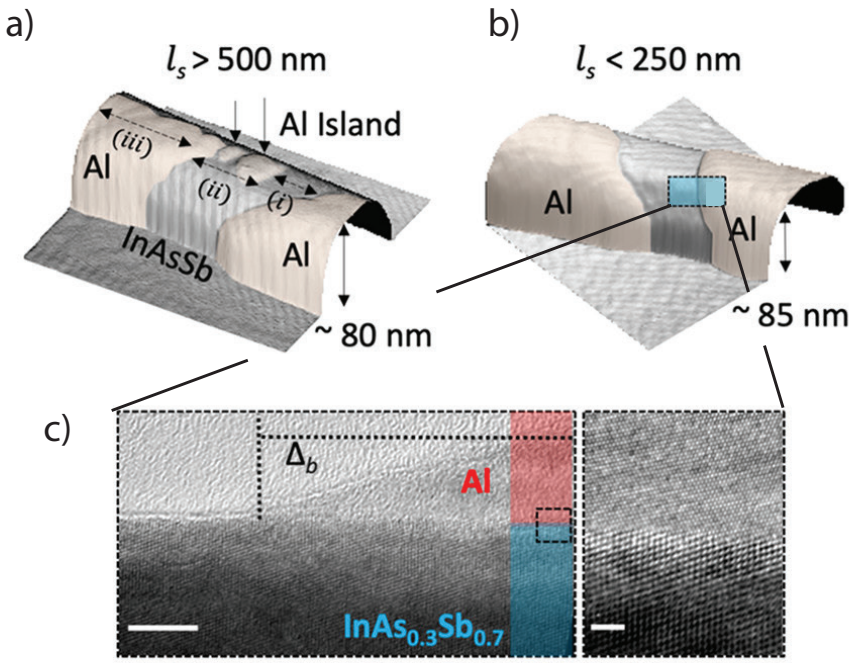

Figure 2.6.: AFM images of two NWs with shadow junction created by a nearby NW placed at $l_s > 500$ nm in a) and $l_s < 250$ nm in b). c) High Resolution TEM image of the junction, where the Al thickness broadening Δ_b and a good interface epitaxial match are observed. The scale bars are 5 nm (left) and 1 nm (right). Figure adapted from Publication 4 with permission from American Chemical Society, Copyright 2020.

chapter 1, for the realization of Karzig et al. approach of a topological quantum computer it is needed the scalable growth of NW networks. Some experiments have been performed in this direction [77], but more development is needed in order to consider the VLS method as a truly scalable solution.

2.4 Selective Area Growth

SAG is an MBE growth method that was first investigated decades ago [54, 55]. Nowadays it has gained again attention due to its promising benefits on the area of quantum computing [49, 56]. The main advantages of SAG compared to VLS is the freedom of design of the grown structures and the scalability of the required NW networks.

The platform concept of SAG consists on covering the growth substrate with a mask of an amorphous layer, such as SiO_2, and opening windows by means of electron lithography where growth occurs selectively. In order to grow

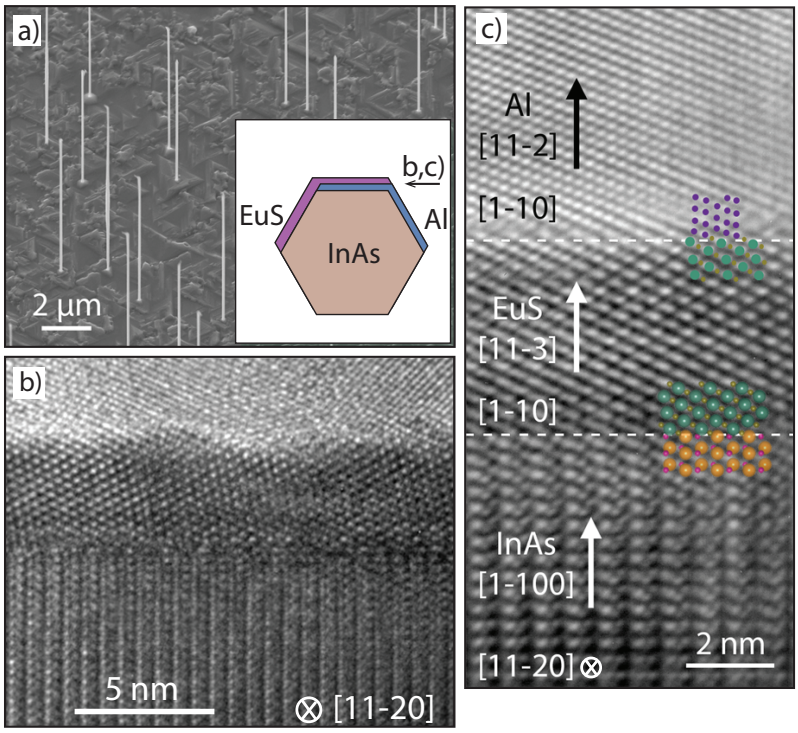

Figure 2.7.: Semiconductor-ferromagnetic insulator-superconductor VLS NWs. a) Tilted SEM image of InAs NWs grown on InAs (111)B substrate with EuS and Al depositions as described in the sketch inset. b) HRTEM image of the three different layers InAs-EuS-Al, at the $[11\bar{2}0]$ zone axis described in a) inset. c) High magnification of the different interfaces and their crystallographic epitaxial directions. Superposed are atomic models to show the atomic arrangement near the interface. Figure adapted from Publication 5 with permission from American Chemical Society, Copyright 2019.

only in the opened masks, adatom desorption is required on the mask while allowing the growth in the openings. This condition is known as selectivity and it imposes constrictions on the growth control parameter space. Figure 2.8 is a qualitative SAG selectivity window describing the different regions that arise based on the precursor fluxes and substrate growth temperature. The SEM images in the background illustrate the growth result on each of the 3 areas of the SAG window: crystal growth and nucleation on the mask (left), selectivity with crystal growth and no nucleation on the mask (center) and no growth on the mask nor the crystal (right).

The precise location of the boundaries presented in the SAG window in figure 2.8 would be dependent on substrate out plane orientation, mask composition and roughness, and growth species composition [57, 78]. The mask critical

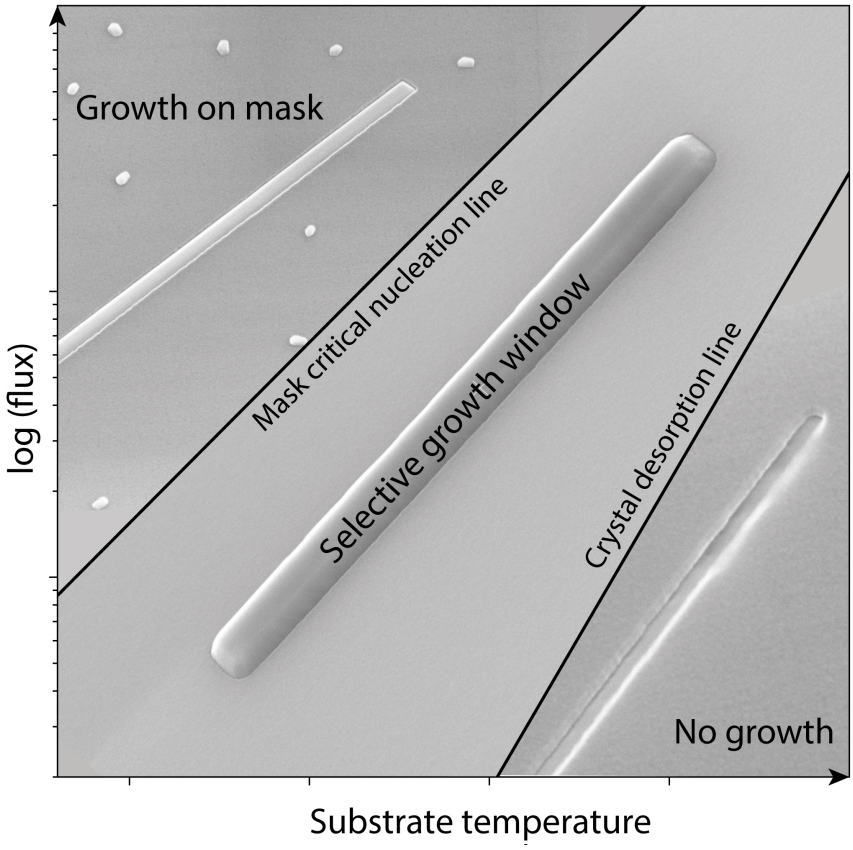

Figure 2.8.: Conceptual sketch of the SAG selectivity window. Selective growth happens inside the region limited by the mask critical nucleation line and the crystal desorption line.

nucleation line of GaAs and InAs SAG NWs on GaAs(001) was studied in depth in references [55, 79]. Similarly to VLS growth mechanism, in SAG it is used an over pressure of group V flux, making the growths limited by the group III flux and its kinetics. This point is of importance and it will studied in depth in chapter 4.

Figure 2.9 is an SEM image of an example of a SAG growth of an array of four InAs - $In_{0.7}Ga_{0.3}As$ NWs on InP(001) showing selectivity. As opposed to free standing VLS NWs that can relax elastically to all sides, SAG NWs need to accommodate the strain generated by the lattice parameter misfit of both substrate and NW via plastic and elastic deformation. The growth of buffer layers with a gradient composition between the substrate and the InAs transport channel, like GaAs(Sb)[56] and $In_xGa_{1-x}As$ [80], helps to relax the strain and minimize the appearance of misfit dislocations. Also, SAG allows to choose between different III-V semiconductor substrates to start the epitaxial

growth of NWs, such as GaAs, InP and GaSb, each of them with their different family of out of plane orientation. The choose of the right substrate is not a trivial decision since it will affect the growth conditions, the outcome crystal quality and the device performance made with them.

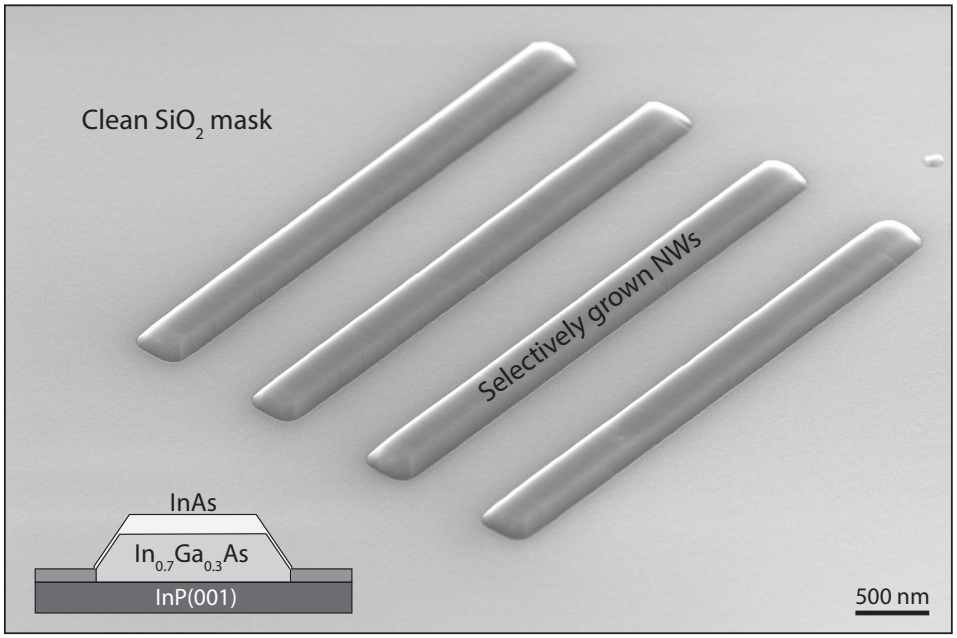

Figure 2.9.: SEM image of an array of four multilayer NWs grown selectively. A buffer layer of $In_{0.7}Ga_{0.3}As$ is grown on the InP(001) substrate to allow the elastic relaxation of the InAs transport channel grown on top.

Figure 2.10a and b show high-angle annular dark-field scanning TEM (HAADF-STEM) cross-sectional example images of NWs with different side faceting. The faceting will vary depending on substrate orientation of the NW, chemical composition, layer stack and how far the NWs are from the equilibrium shape. These dependencies will be studied in depth in chapter 4.

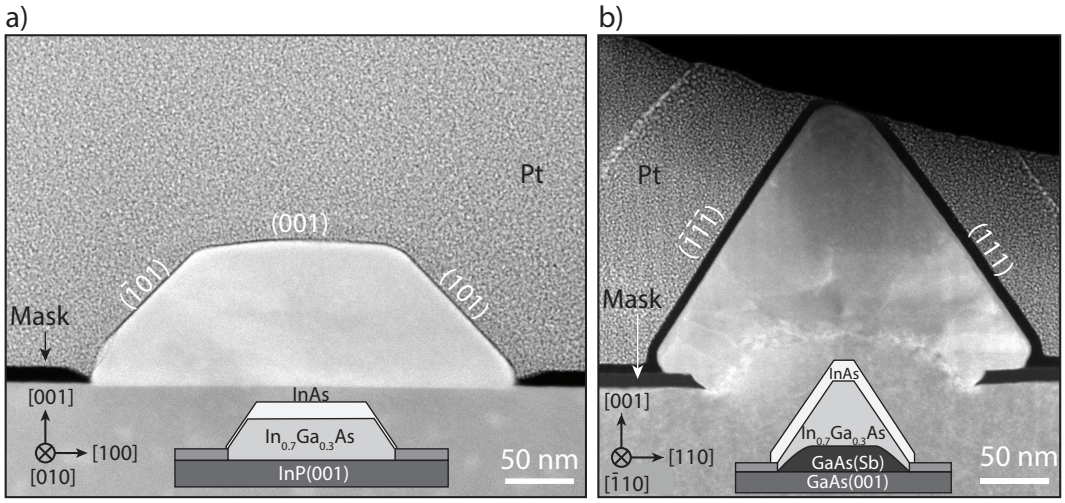

Figure 2.10.: Cross-sectional HAADF-STEM images of SAG NWs oriented along different in-plane crystallographic direction. a) $In_{0.7}Ga_{0.3}As$-InAs NW oriented along the $[010]$ crystallographic direction with dominant $\{101\}$ and (001) facets. b) GaAs(Sb)-$In_{0.7}Ga_{0.3}As$-InAs NW oriented along $[1\bar{1}0]$ with dominant side $\{111\}$ facets.

3 Pre-growth Fabrication and Post-growth Characterization

SAG mechanism heavily relies on the reproducible fabrication of the mask layer without damaging the underneath substrate, when opening windows to define the NW growth. Also, in order to study the outcome and quality of a growth, it is needed to perform different characterization techniques.

This chapter presents the experimental techniques used for pre-growth fabrication of the substrates and the post-growth characterization to study the resulting samples.

3.1 Pre-growth fabrication processes

A reliable and reproducible fabrication of the SiO_x mask is one of the most critical steps in SAG. Changes in roughness, impurity density, uniformity or grain size will have an impact on the adatom kinetics and hence, on the outcome of the NW growth. The overall mask fabrication process is well established as it employs standard techniques used widely in semiconductor fabrication cleanrooms. Figure 3.1 describes the steps needed to fabricate a SAG mask from a III-V semiconductor substrate.

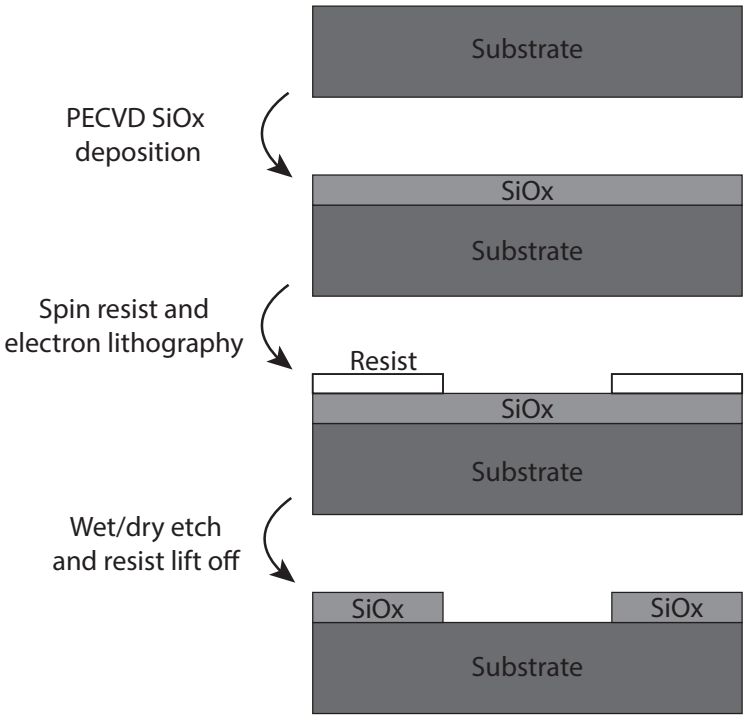

Figure 3.1.: Substrate pre-growth fabrication flow to generate a patterned mask for SAG.

In the first step of figure 3.1, 350 μm thick with 2" diameter epi-ready substrates of the desired chemical composition and out of plain orientation are acquired from commercial manufacturers. An important property to consider is the miscut angle error, which affect the adatom kinetics by introducing additional nucleation points along step edges. For the GaAs, InP and GaSb substrates used in this thesis, the miscut angle error is $\sim 0.1°$ which introduces up to 1 atomic step every $\sim$ 300 nm. The substrates of the presented data are from WaferTech. A 10 nm dielectric layer is deposited on top of the substrate via plasma enhanced chemical vapour deposition (PECVD), in the second step of figure 3.1. The most used chemical composition for SAG of NWs is SiO_2, although other compositions have been studied offering different performances, like SiN [81], Ti [82] or HfO_x [83].

In the third step, a thin layer of poly(methyl methacrylate) CSAR 13 polymer resist for electron beam lithography (EBL) is applied to the SiO_2 and baked at 185 °C. The resist is exposed by an electron beam on the areas of the design where the mask apertures will be placed, in a 125 kV Elionix EBL system. Later, the resist is developed, exposing the SiO_2 parts that will be etched and covering the rest of the mask from the etchant. Dry etch via inductively

coupled plasma reactive ion etching etching (ICP-RIE) or wet etch via amonium fluoride buffered oxide etching (HF) is used to remove the SiO_2 mask in the exposed areas, in step four of figure 3.1. As the last step, the lift off removal of the remaining resist leaves a clean SiO_2 mask selectively etched defining the parts of the substrate that will grow NWs in SAG by MBE.

3.1.1 Plasma Enhanced Chemical Vapour Deposition

PECVD is nowadays the most used film deposition technique for III-V SAG masks, giving the best results for the type of materials it can work with and the temperatures needed during the process [84]. Other deposition techniques such as atomic layer deposition of HfO_x[83] or sputtering of Ti [82] were studied in the past. However, the drawbacks for ALD are low typical grain size of ~ 10 nm and its extremely slow deposition rates of ~ 0.01 Å/s. Sputtering has a small step coverage and a poor film density. On the other hand, PECVD offers a low impurity level and high density of the deposited films, big grain sizes of ~ 100 nm and high deposition rates, at a process temperature of 300 °C. Low pressure chemical vapor deposition is a technique that in principle offers even better results than PECVD in grain size and the lowest impurity level, however its process temperature is ~ 600 °C making it incompatible to III-V substrates due to their low melting point.

Figure 3.2 shows an ellipsometry image of a 10 nm nominal thickness deposited thin film of SiO_x over a 2" substrate for SAG growth. Five point measurements are performed over the edges of the substrate and the results are used to estimate the height profile of the deposited layer. The thickest point is at the center of the substrate with 10.956 nm and the lowest at the top corner with 10.827 nm. Over the span of 4 cm across the substrate the deposition shows an extremely homogeneous film thickness. This allows to obtain comparable results after the etching process of the mask in different places of the substrate.

In order to improve further the reproducibility of SAG masks on fragile substrates like GaSb, double layer masks of different compositions are developed. A first layer of 2 nm AlO_x ALD deposition below the standard 10 nm PECVD

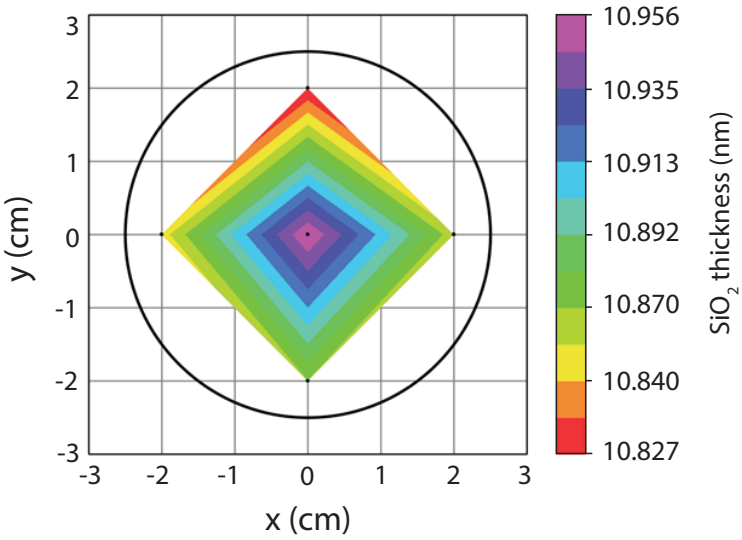

Figure 3.2.: SiO_2 thickness on a 2" wafer after a 10 nm PECVD deposition. Image acquired by ellipsometry.

SiO_2 helps to stop the etching process of SiO_2 before starting to damage the underneath substrate. The remianing AlO_x is then precisely etched by more controlled etching methods, like wet etch for this specific layer.

3.1.2 Wet and dry etching

The selective etch of the SiO_2 mask is the most important step during substrate pre-growth fabrication in order to guarantee the growth reproducibility. HF wet etch of SiO_2 is extensively used due to its simplicity and low cost, although it offers a series of drawbacks. A precise calibration of the etching rates must be done in order to avoid over etching of the underneath substrate. Buffered HF reactivity with SiO_2 is much higher than with III-V semiconductors, allowing for a controlled etch rate of the mask as the reaction naturally stops after reaching the substrate [85, 86]. However, if the HF solution is not precisely diluted and the substrate dip time is not perfectly timed the etchant will affect the surface of the substrate. Figure 3.3a shows the etch result of a wet etch experiment on a substrate with a SiO_2 PECVD deposited mask on top. The recipe used was: pure HF during 3s substrate dip for 10 nm of SiO_2, at room temperature. The mask is completely removed from the lithography exposed areas leaving the GaAs substrate exposed. The effect of a time imprecision, probably caused the human reaction time, leaded to an over etch of the first atomic layers of the substrate creating cavities underneath the edge of the SiO_2

mask. Another limitation of this etch approach is the lateral width increase of the defined areas during lithography. This implicitly sets a lower boundary to the minimum width attainable by this method of ~ 90 nm [83].

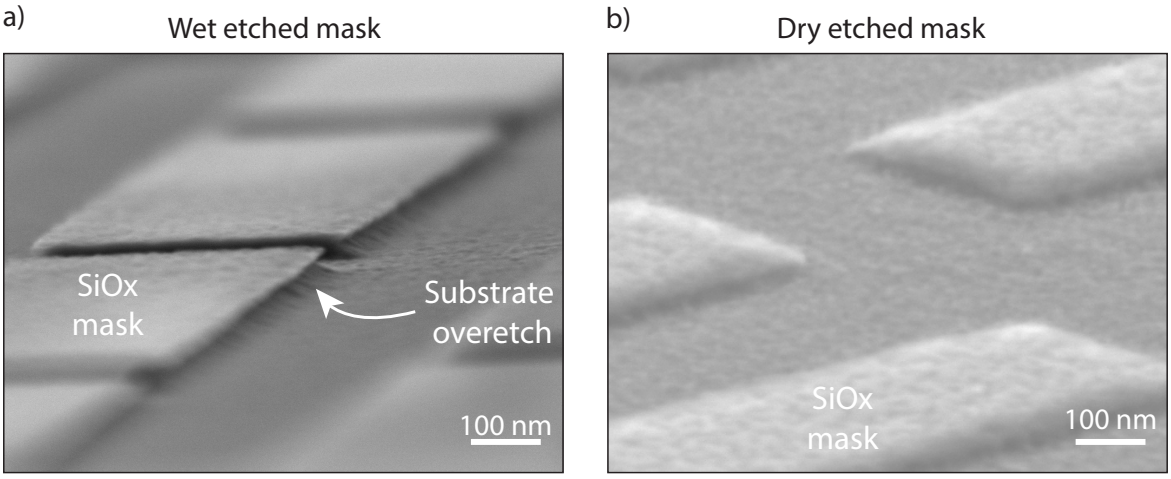

Figure 3.3.: High tilt SEM images of a pre-growth fabricated substrate by a) wet etch and b) dry etch.

Dry etch via ICP-RIE is a more sophisticated technique for selectively etching SiO_2 masks on SAG substrates. Its functioning principle is the creation of a CF4 reacting plasma by a radio frequency electromagnetic field generated by induction coils. The ions in the plasma are accelerated towards the substrate surface, which acts as a cathode, inducing a physical bombardment on the surface and at the same time than inducing chemical etching reactions with the SiO_2. Figure 3.3b shows the result of a SiO_2 mask on a GaAs substrate selectively etched by ICP-RIE, where no mask under etch is observed. The fact that ions from the plasma are created on top of the sample avoids over etch under the mask and allows the creation of thinner mask openings, due to the high directionality of the ions accelerated towards the surface. This technique is used for the etch steps on the majority of the samples presented in this thesis.

New etching methods still in development like atomic layer etching are promising techniques for achieving the highest quality of SiO_2 SAG masks [87].

3.1.3 Pre-growth substrate and mask roughness

Pre-growth characterization is performed in all fabricated substrates to inspect the quality of the SiO_2 mask and the overall cleanliness, to avoid the introduction of impurities into the ultra high vacuum MBE chamber. Figure 3.4 shows an AFM image with the typical roughness of a fabricated SiO_2 mask on a GaAs(001) substrate. The mask height is (0.06 ± 0.41) nm and the substrate is (-10.28 ± 0.37) nm. This implies that the substrate surface was not over etched during the ICP-RIE process, as the nominal height of the SiO_2 was 10 nm. Both mask and substrate have very low values of roughness which suggest that both surfaces are close to be atomically flat.

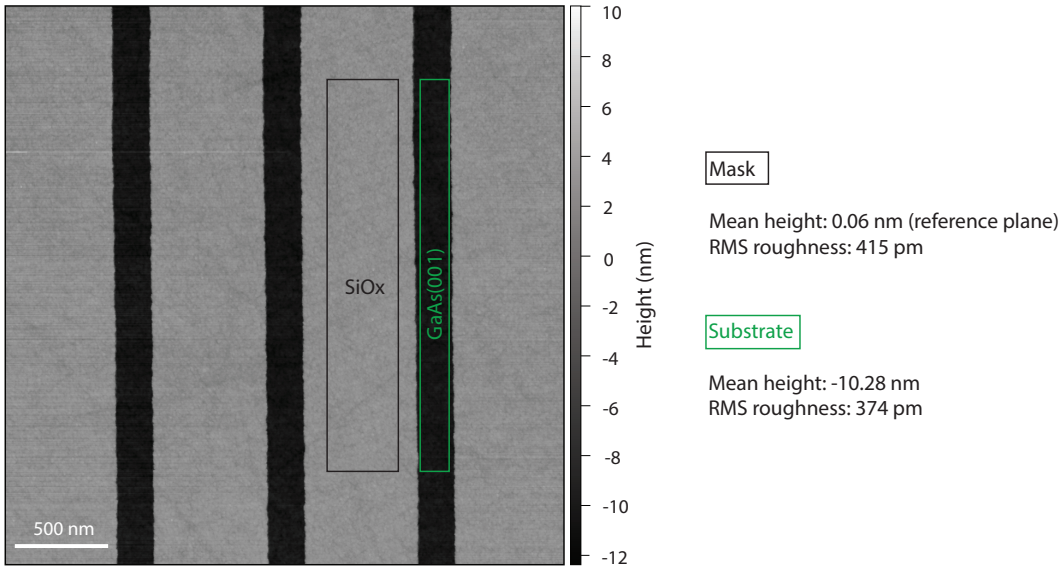

Figure 3.4.: AFM image of a SiO_x pre-growth mask fabricated by dry etch and substrate used for SAG. Their typical roughness values are comparable with the height of a GaAs monolayer.

Most of the samples presented in this thesis were fabricated following the same recipe, which offered a high reproducibility allowing to compare results between different SAG growths and disregard the influence of the mask on the observed phenomena presented in chapter 4. The full fabrication recipe is detailed in appendix A.

3.2 Post-growth characterization

Post-growth characterization of SAG NWs is crucial in order to study the growth outcome and one of the main parts of this thesis. Unlike the characterization of VLS NWs, which can be broken from the base with a micromanipulator and deposited directly on a TEM grid, SAG NWs are epitaxially attached in-plane to the substrate. This fact implies the necessity of performing a laborious sample preparation process to be able to observe in TEM the interface atomic arrangement quality and defect generation in multilayer samples.

3.2.1 Focused Ion Beam lamella preparation

Sample preparation via focused ion beam (FIB) for TEM observation is performed in the multilayer SAG samples presented in this thesis, to generate a transversal cut of the NWs called lamella. The lamella needs to be electron transparent to be characterized in TEM, with a width < 100 nm [88].

A Ga ion etching dual beam FIB is a microscope with two differentiated columns: an electron column and a ion column. The equipped electron column is a fully operative SEM with the same high end imaging capabilities as single electron column SEMs. The Ga column is located at 53° tilted from the electron column. The setup used for the samples prepared for this thesis was a FEI Helios NanoLabTM 650.

From a reservoir of liquid Ga, heavy Ga^+ ions are generated and accelerated towards the sample by electromagnetic lenses using the same principles than in electron optics. Due to their high mass and acceleration, Ga^+ ions reach energies of ~ 50 keV. Focusing the generated Ga^+ into a small probe of ~ 5 nm will sputter atoms from the surface of the sample. This allows to cut parts of the sample in a controlled way, creating the possibility of extracting thin cross-sections of the specimen.

Prior the start of the sample milling to extract a cross-section of a SAG NW, a Pt layer is deposited selectively on the region of interest via FIB-assisted chemical vapor deposition. The main purpose of using this heavy metal is to protect the underneath sample and its properties during the preparation

process. Two ~ 10 μm deep trenches are milled at both sides of the region of interest to define a lamella of Pt and substrate material containing the sample. By welding with Pt a micromanipulator needle to the lamella and performing an undercut, the lamella releases from the substrate and it is re-welded to a TEM grid. As a last step, a series of milling steps are performed to the lamella until it reaches an electron transparency width of < 100 nm. The details of the full preparation recipe is described in appendix C.

However, TEM lamella preparation by Ga^+ FIB ion milling can have an impact on the crystal quality of the sample. Due to the high energy acceleration of Ga^+ ions, they can get incorporated inside the crystal at depths up ~ 1 μm. This effect is called Ga implantation and can generate false results by increasing artifically the Ga content in a given III-V semiconductor, during chemical composition experiments performed in TEM. In addition, if the Pt protection layer is not thick enough or using an excessive energy in the last thinning steps it can cause an amorphization in the crystalline sample.

3.2.2 High Angle Annular Dark Field Scanning TEM

Scanning TEM (STEM) is a microscopy imaging technique performed in TEMs that allows to characterize the crystalline structure of the prepared lamellae, down to the atomic level. With an electron acceleration of 300 kV and an energy filtering monochromator, the spatial resolution is pushed to 0.25 nm at 300 kV.

In modern STEMs, aberrations in the electron probe wave front introduced by non-ideal lenses to electrons travelling away from the optical axis becomes the limiting factor for obtaining higher resolutions. The ideal electron wave front has spherical shape and any deviation from it caused by lens aberrations is defined as the aberration function $\chi(\theta, \phi)$. The aberration function depends

on latitude θ and azimuth ϕ spherical polar coordinates. Hence, the aberration equation can be described as:

$$\begin{aligned}\chi(\theta,\gamma) = C &+ \theta(C_{01a}\cos(\phi) + C_{01b}\sin(\phi)) \\ &+ \frac{\theta^2}{2}(C_{10} + C_{12a}\cos(2\phi) + C_{12b}\sin(2\phi)) \\ &+ \frac{\theta^3}{3}(C_{23a}\cos(3\phi) + C_{23b}\sin(3\phi) + C_{21a}\cos(\phi) + C_{21b}\sin(\phi)) \\ &+ \frac{\theta^4}{4}(C_{30} + C_{34a}\cos(4\phi) + C_{34b}\sin(4\phi) + C_{32a}\cos(2\phi) + C_{32b}\sin(2\phi)) \\ &+ \cdots\end{aligned} \tag{3.1}$$

where the different C_{xy} are the aberration coefficients for the different order of aberrations. For electrons travelling near the optical axis $\theta \approx 0$ the aberrations tend to disappear, specially the higher order ones. The aberrations that introduce the biggest distortions to the wave front are twofold astigmatism C_{12}, coma C_{21} and spherical aberration C_{30}.

Hexapole aberration correctors are multipole electromagnetic lenses that can introduce small distortions in the wave front in order to cancel out up to third order wave front aberrations, caused by the rest of the lenses. High-end TEMs have a set of hexapole lenses [89] that allows to correct aberration coefficients up to C_{30} (spherical aberration) and C_{32} (twofold astigmatism). This, together with the reduction of chromatic aberration corrected by the monochromator, allow these TEMs to achieve ~ 1.6 Å resolutions in STEM mode.

The high angle annular dark field (HAADF)-STEM is an imaging mode that uses an annular detector placed below the sample that acquires the Rutherford scattered electrons from the sample. The detector has an angular apertures of tens of milliradians. The density of electrons detected in HAADF-STEM is exponentially dependent on the atomic number of the sample, with a relation $\sim Z^{1.7}$. For a lamella sample of homogeneous width, HAADF-STEM becomes a useful imaging technique offering a chemical composition contrast dependence, with brighter regions corresponding to high Z composition. The images presented in this thesis were acquired at 300 kV acceleration voltage using the High Angle Annular detector. The contrast in this imaging mode depends on material thickness and elemental atomic mass of the sample.

The FEI Titan 80-300 TEM was used for the acquisition of the data presented in this thesis. Images are treated in the freeware Fiji (an extension if Image J [90]) and Gatan Digital Micrograph for Fast Fourier Transform (FFT) noise cleaning and plane selection for stacking fault formation analysis

3.2.3 Other characterization techniques

Characterization of the surface can be done with multiple characterization techniques giving different types of information, such as SEM, AFM, scanning tunneling microscopy, x-ray diffraction or raman spectroscopy among others. The samples presented in this thesis are extensively studied by AFM and SEM.

Atomic Force Microscopy

AFM post-growth characterization of the samples was perfomed in SAG NWs to calculate the volume of material incorporated. The data presented in this thesis was acquired in a Bruker Icon AFM using tapping PeakForce Quantitative Nanoscale Mechanical Characterization mode. The probes used were Bruker Scanasyst-Air.

Other AFM techiques such as scanning spread resistance microscopy AFM [91] or tip enhanced Raman spectroscopy [92] can be implemented in the Bruker Icon setup to characterize the surface chemistry properties of the sample.

Scanning Electron Microscopy

SEM is used after the pre-growth fabrication processes to study the quality of the etching process and detect any SiO_2 remnants on the mask openings. Since it is performed in high vacuum conditions ($\sim 10^{-5}$ Pa) this characterization is overall cleaner than AFM. The characterization is performed in a sacrificial part of the substrate to avoid long electron exposures on mask openings that can lead to undesired C deposition.

Post-growth characterization by SEM is extensively performed on the NWs to study the quality of the growth. New imaging modes, such as immersion electron channeling contrast imaging, will be studied in depth in the second half of chapter 5.

Optical Microscopy

An Olympus BX43 optical microscope in bright and dark field was used for quick observations before and after each fabrication process, to check for possible particle contamination.

4 Selective Area Growth Modes

The overlapping parts from this chapter with Publication 1 (reference [93]) are reprinted with permission of American Physical Society, Copyright 2021. License number: RNP/21/SEP/044571.

4.1 Introduction

One-dimensional semiconductor NWs have the potential to become the host platform of future quantum information technologies [44, 60, 94, 95]. Among the different crystal growth techniques of semiconductor NWs [48, 74, 96–98], Selective Area Growth (SAG) of in-plane III-V NWs using Molecular Beam Epitaxy (MBE) is a method for synthesizing scalable gate-controlled one-dimensional quantum electronics [99, 100]. In particular, the design flexibility allows for arbitrary device architectures including networks of NWs and quantum dots.

Recently, in-plane III-V NW arrays have gained attention and have been demonstrated with a variety of materials, shapes and dimensions [49, 56, 57, 78, 101–106]. Among the most promising designs, Karzig's SAG NW networks for fabricating a topologically protected quantum computer are the most feasible [60]. However, the proposed design has hard requirements regarding NW homogeneity and reproducibility, due to the fragile topological phases created in them. Optimising SAG crystal growth for the functionality and quality of such quantum structures implies optimizations of the morphology [104], composition [107], crystal disorder [108–110] and strain uniformity

[56, 111]. This makes it mandatory to control the incorporation rates with high precision in order to grow as reproducible NWs as possible and optimize the performance of quantum devices based on these NWs [112, 113].

This chapter presents a study of adatom kinetics and incorporation during crystal growth of in-plane GaAs, InGaAs and InAs SAG NWs, grown by MBE on GaAs(001), InP(001) and GaSb(001) substrates. It also discusses two groups of parameters that affect SAG NW growth rates: growth control parameters, namely substrate temperature (T_{sub}) and beam fluxes (f_i), and the NW design such as the width (w), interwire pitch (p), and in plane crystallographic orientation $[hkl]$. The results establish that these dependencies are of critical importance for the design of reproducible arrays of NWs.

4.2 Adatom kinetics during SAG

A crystal growth by MBE is facilitated by incoming beam fluxes of growth species that impinge and get adsorbed on the substrate surface [55, 114, 115]. The growth mechanism is described by the transition state kinetics of adatoms, where the transition rates $\Gamma_{\alpha\beta}$ (α and β denote the initial and final state, respectively) are limited by effective kinetic barriers [116]. To achieve SAG, the adatoms on the mask must either desorb or diffuse to the exposed crystal areas. The crystal growth rate is highly dependent on T_{sub} and f_i, as well as the surface state parameters, e.g. activation energies for adatom desorption, surface diffusion, nucleation and incorporation [57]. Following the continuum kinetics approach in reference [116] and ignoring the entropic terms for simplicity, the transition rates can be described by the Arrhenius equation

$$\Gamma_{\alpha\beta} \propto \rho_\alpha \exp\left(-\frac{\delta g_{\alpha\beta}}{k_B T_{sub}}\right), \tag{4.1}$$

where k_B is the Boltzmann constant, ρ_α is the adatom density in the initial state, and $\delta g_{\alpha\beta}$ is the effective activation energy for the transition.

Figure 4.1a sketches the different types of adatom transitions which take place during SAG: adatom diffusion on either the mask surface ($\Gamma_{a_m a_m}$), the growing crystal surface ($\Gamma_{a_c a_c}$) or across a mask-crystal boundary ($\Gamma_{a_m a_c}$); adatom incorporation into the crystal solid phase ($\Gamma_{a_c s}$), or via nucleation to

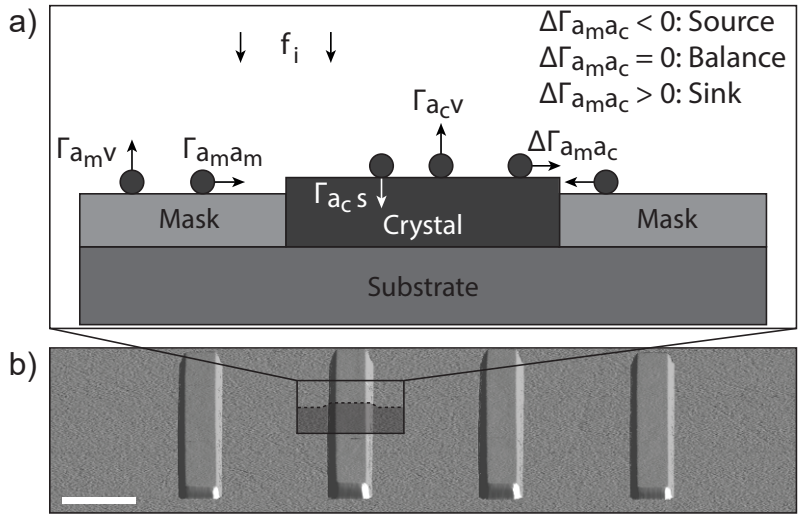

Figure 4.1.: (a) Schematic of adatom transitions during SAG. (b) AFM image of four parallel GaAs NWs oriented along the $[1\bar{1}0]$ crystal orientation on a GaAs (001) substrate. Scale bar is 500 nm.

solid phase on the mask ($\Gamma_{a_m s}$); or adatom desorption from the mask ($\Gamma_{a_m v}$) and crystal ($\Gamma_{a_c v}$) to vapour. All transition rates in this chapter are effective rates describing the mean properties of the transitions, e.g. $\Gamma_{a_c s}$ describes both the nucleation limited transitions as well as potential single atomic barriers for incorporation. Possible single atom barriers not considered are the bond dissociation of molecules, like $As_2 \rightarrow 2As$ prior incorporation forming a Ga-As bond. Due to the geometry, the mask-crystal boundary is 1D-like (linear) and the boundary of the $\Gamma_{a_c s}$, $\Gamma_{a_c v}$, $\Gamma_{a_m s}$ and $\Gamma_{a_m v}$ transitions is 2D-like (surface).

4.2.1 Mask - crystal adatom flux

The total current of adatoms of species i being incorporated in a NW segment of length l and width w ($l \gg w$) is given by adatom conservation:

$$I_{a_c s,i} = (f_i - \Gamma_{a_c v,i}) \cdot w \cdot l + (\Gamma_{a_m a_c,i} - \Gamma_{a_c a_m,i}) \cdot 2l, \tag{4.2}$$

assuming no substrate decomposition $\Gamma_{sa_c} = 0$. From mass conservation, the incorporation rate on the SAG NW can therefore be written as

$$\Gamma_{a_c s} = \sum_i f_i - \Gamma_{a_c v,i} + 2\frac{\Gamma_{a_m a_c,i} - \Gamma_{a_c a_m,i}}{w}. \tag{4.3}$$

where the units of f_i and $\Gamma_{a_c v,i}$ are $\frac{\text{atoms}}{s \cdot m^2}$ and the units of $\Gamma_{a_c a_m,i}$ and $\Gamma_{a_m a_c,i}$ are $\frac{\text{atoms}}{s \cdot m}$.

Then, the crystal volume growth rate is $\Gamma_{a_c s} \cdot \Omega$ where Ω is the volume of a III-V atomic pair. While f_i is a controlled parameter, the desorption term $\Gamma_{a_c v,i}$ is highly dependent on T_{sub}, following the exponential nature of the Arrhenius equation 4.1. Thus, if the desorption from the crystal can be ignored for a given T_{sub}, i.e. $\Gamma_{a_c v} = 0$, the relevant term for controlling the growth rate is the flux across the mask-crystal boundary,

$$\Delta\Gamma_{a_m a_c,i} = \Gamma_{a_m a_c,i} - \Gamma_{a_c a_m,i}, \tag{4.4}$$

where the forward flux $\Gamma_{a_m a_c,i}$ is the flux of adatoms to the crystal collected from the mask and the backward flux $\Gamma_{a_c a_m,i}$ is the flux of adatoms to the mask collected from the crystal.

$\Delta\Gamma_{a_m a_c,i}$ is the term that differentiates the incorporation rates of SAG NWs compared to planar growths with no mask, hence it is of great importance. Depending on the sign of $\Delta\Gamma_{a_m a_c,i}$, different growth modes are expected to arise. The SAG growth mode is defined as source if $\Delta\Gamma_{a_m a_c,i} < 0$, sink if $\Delta\Gamma_{a_m a_c,i} > 0$, and balance if $\Delta\Gamma_{a_m a_c,i} = 0$.

4.3 SAG growth modes on binary materials

The structures used in the experiments consist of individual NWs and arrays of NWs, with varying pitch and width. The NWs are 14 μm long and to avoid influence from the ends, the measure of incorporation is only considered in the central region of the NW. The employed SiO_2 mask fabrication flow and crystal growth concept by MBE are described in chapter 3. Figure 3.4 contains information about the typical roughness of mask and substrate prior MBE growth.

The MBE beam fluxes are calibrated to the corresponding planar growth rates using RHEED oscillations under conditions where desorption of group III can be ignored [57]. The V:III 1:1 flux ratio is calibrated with the surface

reconstruction change procedure, using RHEED on GaAs(100) substrates [117, 118]. Temperature is measured with pyrometer, which is calibrated with GaAs oxide desorption [119].

After growth, the SAG NW volume in single layer growths is measured by AFM and the cross-sectional area on the multi-layer sample is measured by cross-sectional TEM. The NW growth rate, Γ_{inc}, is defined as the measured crystal volume divided by the volume of a NW section with the same w and l from the equivalent planar growth used for the flux calibration. Γ_{inc} is a measure of the amount of material incorporated in a NW compared to the 2D growth and hence, the effect on material incorporation caused by the mask-crystal interface term $\Delta\Gamma_{a_m a_c}$ from eq. 4.3.

4.3.1 Source growth mode

Figure 4.2 shows incorporation rates measured by AFM, to extract the sign of $\Delta\Gamma_{a_m a_c}$ (and thus the growth mode) on pure GaAs and Sb surfactant-aided GaAs(Sb) SAG NWs grown on GaAs(100) substrate at T_{sub} of 603 °C. The Ga flux corresponds to a planar GaAs growth rate of 0.1 monolayers (ML)/s, under As rich conditions (detailed growth recipes are in appendix B). The reason for the selection of these two materials is their use as buffer layers before the growth on InAs transport channels, due to its beneficial effect of crystal defect reduction at the InAs interface [56]. The growth mode is determined by comparing incorporation rates between the two inner and two outer NWs.

In Figure 4.2a the mean incorporation rates of inner and outer NWs is plotted as a function of p for $[1\bar{1}0]$ orientated NWs of $w = 250$ nm. The data reveals a decrease in incorporation rates with increasing p until it saturates at around 4 µm for GaAs and GaAs(Sb) to 0.7 and 0.6 of the nominal growth rate, respectively. Note that the $[1\bar{1}0]$ NWs exhibit different faceting with and without Sb surfactant, with (001) vertical and $\{113\}$ side predominant facets, respectively [80] (more details about faceting in the later section 4.6). The different faceting can affect the total incorporation of the NW due to Ga adatom diffusion length $\lambda_{Ga,c}$ anisotropy on GaAs(001) [120]. However, in the p study this effect is considered to be negligible since $w \ll \lambda_{Ga,c_{[110]}}$ and $\lambda_{Ga,c_{[1\bar{1}0]}}$ [121, 122]. The facet time evolution of GaAs NWs from initial (001) to {113} is not considered because the initial stages of the growth are dominated by the

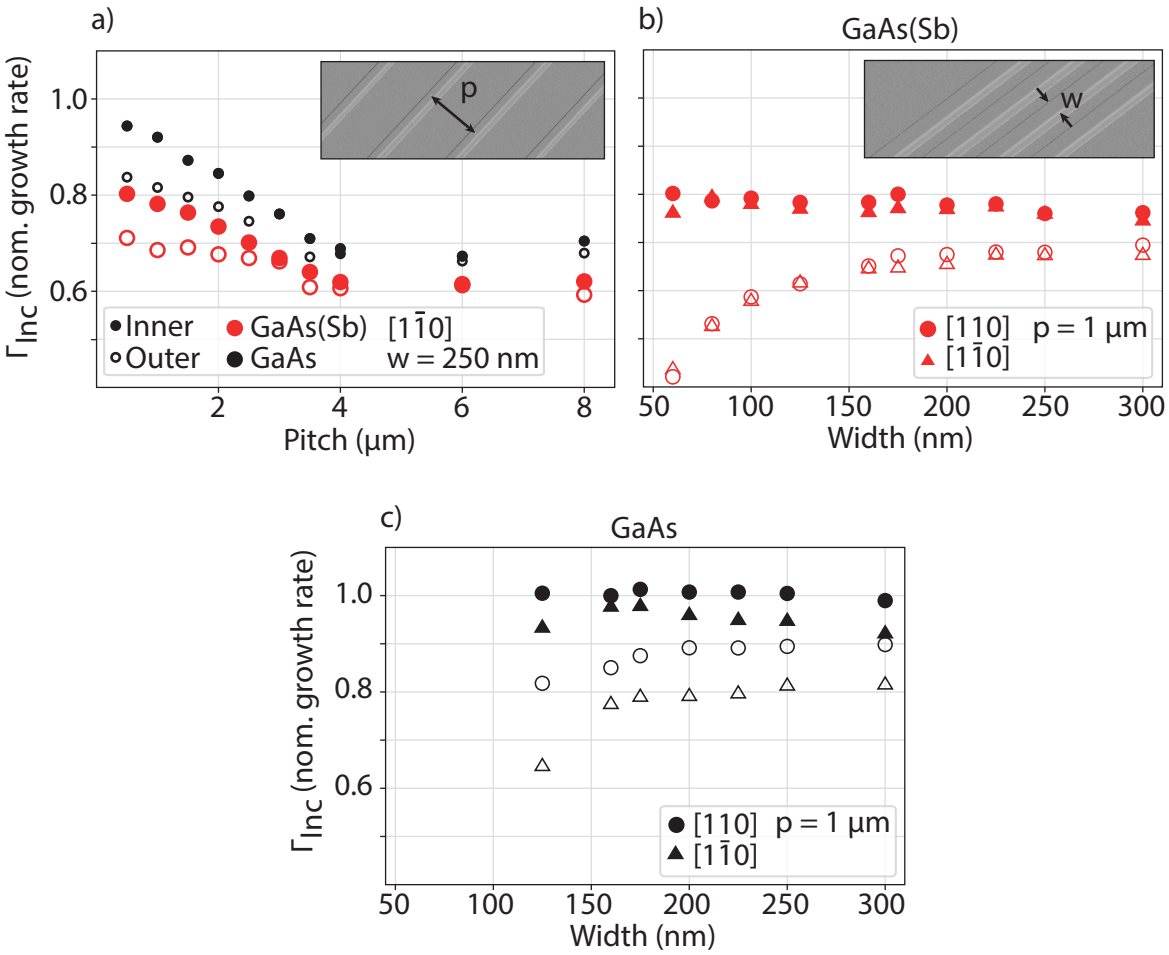

Figure 4.2.: NW Incorporation rate dependence on design parameters, p, w, and crystal orientation. Incorporation rates are measured in units of nominal growth rate of GaAs and GaAs(Sb). All three plots share the same y-scale. Filled (open) points indicate incorporation rates measured on the inner (outer) NWs. GaAs(Sb) is shown by red symbols, and GaAs by black symbols. a) Incorporation rates of inner and outer NWs in a 4 NWs array, as a function of NW p. The inset shows an AFM image of a typical array. b) and c) are the incorporation rates of GaAs(Sb) and GaAs, respectively, as a function of w and for $[110]$ and $[1\bar{1}0]$ oriented NWs. The inset in b) is an AFM image of a typical array.

diffusion on the original (001) substrate and the NWs reach the {113} fully grown facets at the end of the growth process.

The incorporation rate of pure GaAs arrays approaches the nominal value (i.e. $\Gamma_{inc} = 1$) at small p, as expected if the desorption from the crystal is negligible, i.e. $\Gamma_{a_cv,Ga} \approx 0$. By contrast, GaAs(Sb) NWs have lower incorporation rates but with the same overall trend. This general downwards shift of ~ 10 % in

the incorporation curve for the Sb surfactant compared with the pure case can be explained by two reasons: a result of non-reactive surfactants nature, which decreases the number of incorporation sites for adatoms [123, 124] and the higher facet roughness of $\{113\}$ compared to (001), which generates more incorporation sites for pure GaAs NWs. The decrease in incorporation with pitch implies that the growth is in the source mode ($\Delta\Gamma_{a_m a_c} < 0$). As a consequence, an increasing pitch implies a decreasing number of adatoms being shared between neighbouring NWs before they are desorbed from the mask.

In the regime of significantly large pitch ($p \gg \lambda_{Ga,m}$)[99, 125], the sourcing of adatoms between NWs can be ignored. All NWs in the array grow at the same rate and can be considered decoupled from each other. In this regime, the amount of material incorporated by a NW compared to the nominal growth rate is a direct measure of the source mode strength for the given growth conditions.

While the p dependence is used to study the desorption limited $\lambda_{Ga,m}$, the w dependence can be used to study the incorporation limited $\lambda_{Ga,c}$. Figure 4.2b and c show the incorporation rate as a function of w in the 60-300 nm range, with and without Sb surfactant respectively, for both $[110]$ and $[1\bar{1}0]$ oriented NW arrays with $p = 1$ µm.

As shown in Figure 4.2b, the GaAs(Sb) growth rate is independent of $[hkl]$ and even independent of w for the inner NWs. However, for the outer NWs there is a decrease in the growth rate with decreasing w. The outer NW growth rate dependence on w is consistent with equation 4.3; as w increases the sourcing effect from $\Delta\Gamma_{a_m a_c}$ becomes negligible for the given NW, and the incorporation rate converges towards $\Gamma_{a_c s} = f_i - \Gamma_{a_c v,i}$. If $\Gamma_{a_c v,Ga} \approx 0$ and the width approaches $w \gg \lambda_{Ga,c}$ the mean incorporation rate will converge towards the nominal growth rate for all NWs in the array, ignoring the effect of the surfactant. For increasing widths the growth rate converges towards 0.7 - 0.8 of the nominal growth rate, which can be explained with a longer $\tau_{Ga,c}$ due to the role of the surfactant and therefore a higher $\Gamma_{a_c a_m}$. On the other hand, the apparent w independence on incorporation for the inner GaAs(Sb) NWs is not obvious. This apparent independence of Γ_{inc} is speculated to be caused by a compensation on growth rates. The inner NWs get more sourced adatoms from its neighbours, as the outer NWs incorporate less at smaller w.

The Γ_{inc} difference between both inner and outer NWs on both directions with $w = 150 - 300$ nm slowly decreases and it is expected to merge at larger w. In Figure 4.2c, there is a clear dependence on $[hkl]$ and the incorporation rate of GaAs is more efficient on the crystal with Γ_{inc} closer to 1. As shown in the later section 4.5, the NW faceting evolves differently depending on the NW orientation as, which means that $\lambda_{Ga,c}$ also changes during growth. Thus, the crystal surface parameters can be dynamic in nature. The NWs oriented along $[1\bar{1}0]$ form dominating $\{113\}$ facets, while the $[110]$ oriented NWs preserve the (001) top facet. As such, the $[1\bar{1}0]$-oriented NWs exhibit a stronger source effect because the longer lifetime of adatoms on $\{113\}$ facets as compared to the (001) facet, resulting in a lower incorporation rate and therefore a more negative $\Delta\Gamma_{a_m a_c}$ compared to the NWs oriented along $[110]$. This is consistent with the findings in reference [126] which show the incorporation rate of Ga on $\{113\}$ GaAs facets is slower than on (001). Since only mean growth rates are being measured, for simplicity the surface state parameters are assumed constant for the modelling, and any change in the faceting during the growth is not considered.

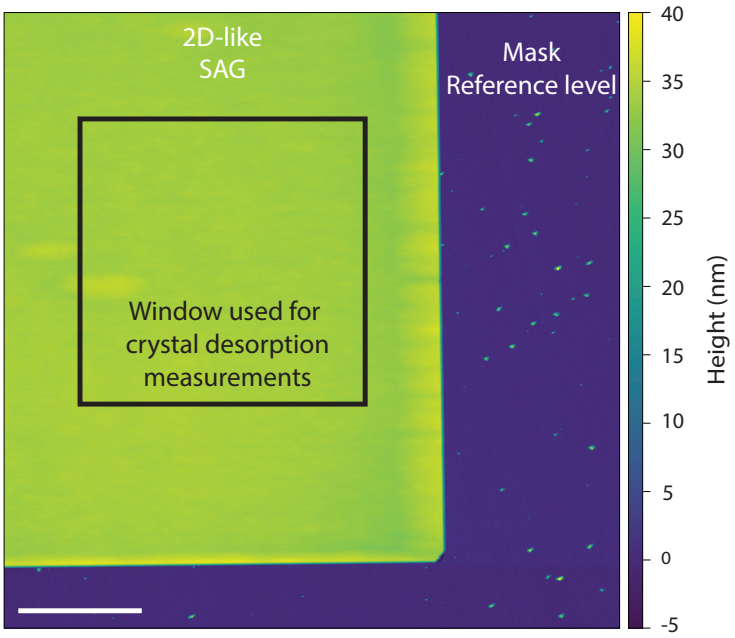

Figure 4.3.: The adatom desorption from the crystal during growth has been calculated measuring the volume from a big mask opening. Then, the volume of the measured square is compared with the nominal calibrated growth rate from the MBE. The image is leveled with the mask surface and the volume is measured in the center of the structure. The sample is GaAs(Sb) grown at 570 °C. Scale bar is 2 µm.

The mask selectivity measurements are performed in areas with no mask openings as detailed in figure 4.3, to avoid any influence from the $\Delta\Gamma_{a_m a_c}$ term. Crystal adatom desorption data is measured on big mask openings grown in the center of the substrate. Figure 4.3 is an AFM image of the corner of a 10x10 µm mask opening from a GaAs(Sb) sample grown at 570 °C. Using the mask as a reference height, the volume of a 5x5 µm square is measured and compared with the equivalent volume from a planar growth sample used for growth rate calibrations.

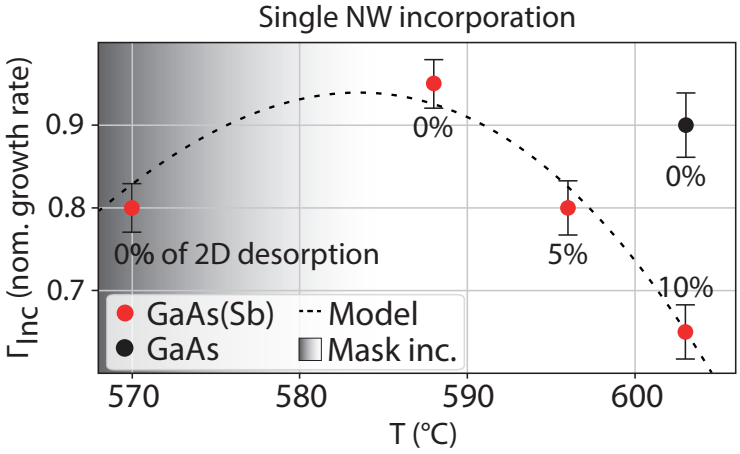

Figure 4.4.: Incorporation of isolated NWs as a function of T_{sub} indicated by black (red) symbols, for GaAs (GaAs(Sb)). The dashed line is extracted from the model based on the later section 4.4.1, highlighting a maximum incorporation near 583 °C. The number below each data point corresponds to the percentage of desorbed material from the crystal $\Gamma_{a_c v}$, measured on large mask openings. The blurred grey background represents the transition from $\Gamma_{a_m s} = 0$ (white) to > 0 (grey).

The growths discussed in the previous paragraphs exhibit a source growth mode. Unlike the usual understanding of VLS growth, where the gold catalyst has a collection area around it from which it collects adatoms for the NW growth [127], the SAG source growth mode is consistent with the NWs having a negative collection area of adatoms. In this area, NWs expel adatoms (instead of collecting them) that eventually desorb from the mask. To answer if it is possible to manipulate the strength of the source effect $\Delta\Gamma_{a_m a_c}$, and potentially achieve balanced and sink growth modes, four identical GaAs(Sb) samples are grown only varying T_{sub} between 570 °C and 603 °C at a nominal growth rate of 0.1 ML/s with a V/III ratio of 9. As shown in reference [54], the reduction of T_{sub} leads to an exponential reduction of $\Gamma_{a_m v}$, which will cause a decrease in $\Gamma_{a_c a_m}$ since the adatom density will be higher on the mask. Incorporation rates are measured on isolated NWs of $w = 250$ nm for each growth, and

plotted in figure 4.4 as a function of T_{sub}. GaAs(Sb) NWs initially increase the incorporation when temperature is reduced, compared to the growths at 603 °C discussed in figure 4.2. The number near each point in figure 4.4 is the 2D desorption ($\Gamma_{a_c v}$) in percents of nominal growth rate.

The dashed line in figure 4.4 is the model prediction of incorporation for the GaAs(Sb) samples, based on the adatom conservation model from equation 4.3 (detailed in the later section 4.4.2) and highlighting a maximum in incorporation around 583 °C for the given growth rate of 0.1 ML/s. None of the samples measured in this series reach nominal incorporation. There are two independent reasons. First, for the two highest temperature samples, the crystal desorption, $\Gamma_{a_c v}$, is non-negligible and equal to 10% and 5% at 603 °C and 595 °C, respectively. Second, as T_{sub} is decreased, adatom desorption from the mask decreases (lifetime increases) and incorporation in the NW increases (lifetime decreases). According to the selectivity window, reducing f while still growing selectively would allow to decrease the T_{sub} neutralizing the source effect by shifting the incorporation curve in figure 4.4 upwards until $\Gamma_{inc} = 1$. However, when nucleation on the mask starts the lifetime on the mask is reduced, making the source effect stronger. The parasitic growth on the mask is marked in figure 4.4 with the blurred grey background, with a transition happening between 570 °C and 588 °C.

Figures 4.5a and b show two AFM images of individual GaAs(Sb) NWs from the same growth, with different w, and separated 50 μm from each other on mask opening. For the 45 nm wide NW, due to the small w, the term $\Delta\Gamma_{a_m a_c}/w$ from eq. 4.3 is negative enough to override the growth on the substrate due to the dominating $\Gamma_{a_c a_m}$, whereas parasitic growth can nucleate on the mask. This would be an extreme case where the design parameter w induces a negative growth rate for the NW at growth conditions that otherwise induce growth in wider mask openings, as shown for the 150 nm wide NW.

Longitudinal end effect

The volume measurements to calculate NW incorporation were performed in the middle part of the NW. Figure 4.6 shows an AFM height line scan (black line) of a GaAs NW located inside of an array (inset) and the effect on the incorporation when approaching the end part. The reduction in incorporation is explained by the increase of available mask surrounding the NW at the end

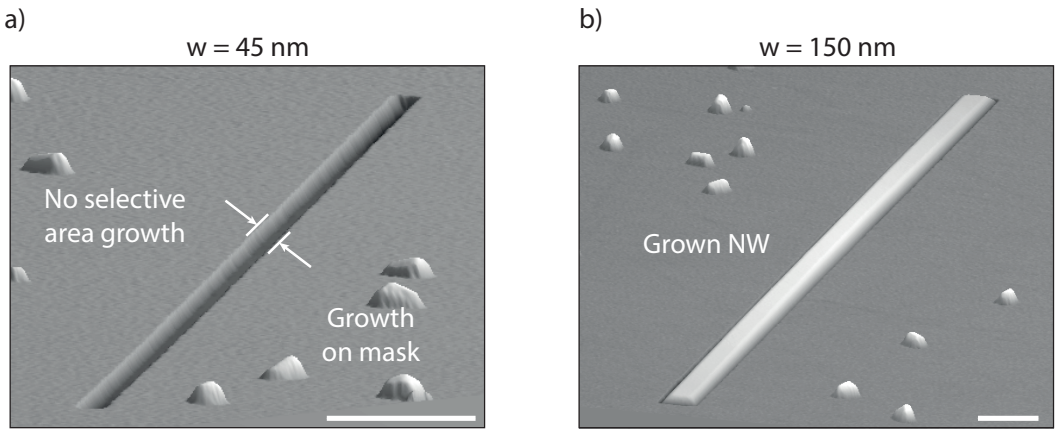

Figure 4.5.: Example of individual isolated 45 and 150 nm wide NWs, both from the same GaAs(Sb) growth. a) 45 nm wide mask opening where growth is overridden due to its width limitation and the source effect. b) 150 nm mask opening separated several μm from a), where the NW is grown as expected. Scale bars are 200 nm.

part, where adatoms can diffuse to and desorb from $\Gamma_{a_m v}$. The incorporation of a long enough NW along the crystal direction [hkl] saturates to a constant value when it is decoupled from the effect of the end part, at a distance from the end larger than the diffusion length of Ga on the crystal $\lambda_{Ga_c,[hkl]}$.

The red line in figure 4.6 is the simulated adatom density along the length of the NW, in arbitrary units. It is calculated by the adatom diffusion coupled equations model explained in the later section 4.4.1. The model predicts the adatom density decrease on the NW towards the end part, from the value 1 in the middle of the NW to 0.5 at the end, in arbitrary units. The abrupt change in height at the end is caused by the NW end faceting. The residual adatom density on the mask is not high enough to cause nucleation and it reduces away from the NW before reaching a base level.

4.3.2 Sink growth mode

The growth mode with positive $\Delta\Gamma_{a_m a_c}$ is defined as sink. In this growth mode, there is a net flux of adatoms from the mask being collected by the NW. The region of the mask where adatoms have a probability of diffusing to the NW is called positive collection area and it is proportional to the diffusion length

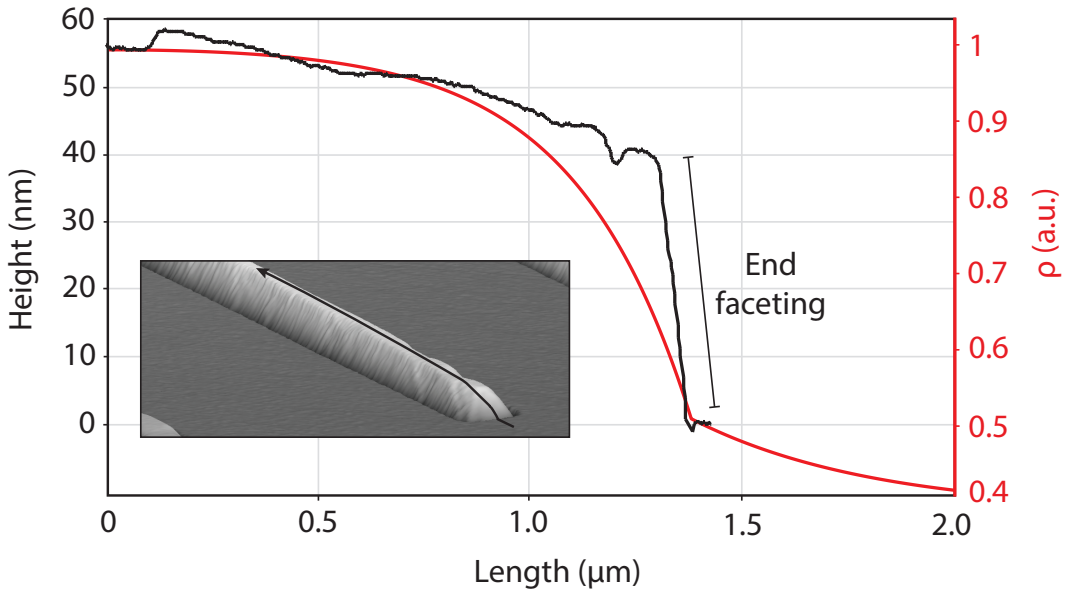

Figure 4.6.: AFM image (inset) and height profile of a 4 μm long GaAs NW along $[1\bar{1}0]$. The height line scan shows the effect in incorporation caused by source growth mode near the NW ends, due to an increase of available mask where adatoms can diffuse by $\Gamma_{a_c a_m}$. The GaAs incorporation steadily increases from the end until the half point of the NW. The red line is the adatom density calculated by the model presented in Section 4.4.1, also following the height trend due to the increase of available mask.

on the mask $\propto \lambda_{Ga,m}$. This collection area is similar in concept to the one that feeds the catalyst droplet in VLS method.

Figure 4.7 shows an array of InAs NWs grown on GaSb(001) in sink growth mode. Figure b is an AFM image of an array of four NWs oriented along $[1\bar{1}0]$, where a height line scan is performed longitudinally along an inner NW (figure c) and other line scan transversely across the four NWs (figure d). In the longitudinal line scan, the height of the central part of the NW does not exceed 100 nm above the mask level, however the height of the end parts of the NW reaches 150 nm. This indicates, that the end parts incorporate more material during growth as compared to the central part, as opposed to figure 4.6. This is caused by the adatoms sinking to the NW from the extra available mask around it, creating a higher adatom density at the end of the NWs. Figure 4.7d also shows an evidence of the sink growth mode. The outer NWs are taller than the inner ones, incorporating more material during growth as opposed to the case presented in figure 4.2. The extra mask available on one of the

sides of the outer NWs allows for extra adatoms to sink on the NW, making the growth of the outer NWs faster than the inner ones. On the other hand, the adatoms on the mask between inner NWs are shared between the two neighbouring NWs.

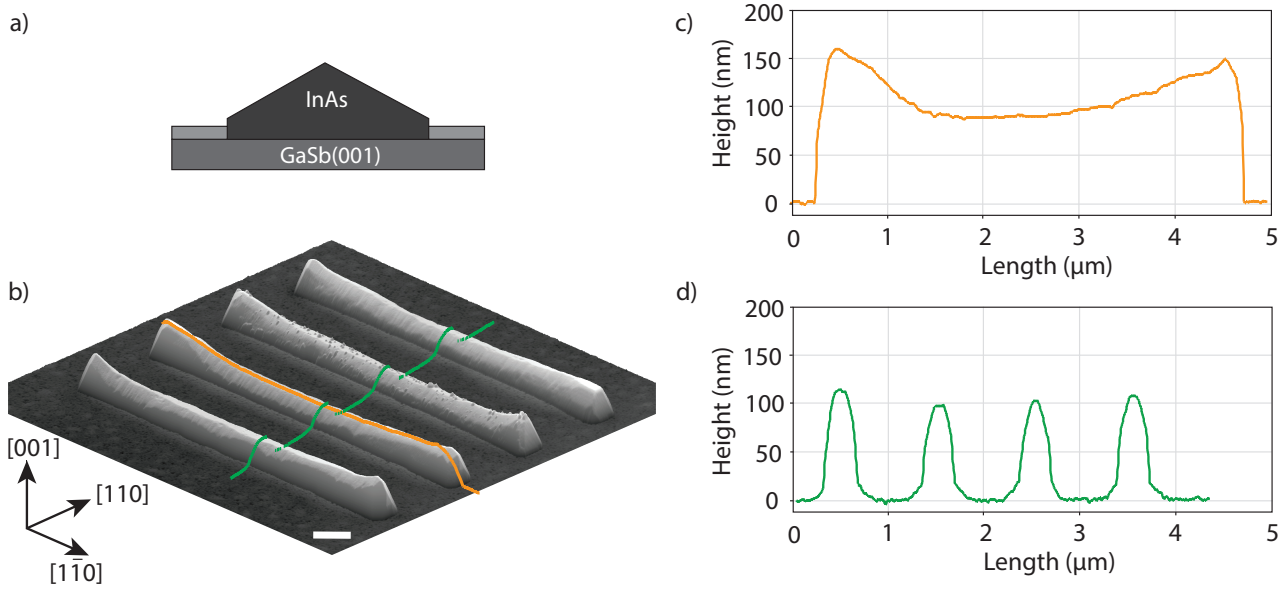

Figure 4.7.: Sink growth mode. a) Sketch of the sample layer composition, InAs NWs grown on GaSb(001) substrate. b) AFM image of an array of 4 NWs oriented along $[1\bar{1}0]$. Scale bar is 1 μm and z axis is scaled by a factor of 2 for better visualization. c) Height profile along the length of an inner NW in the AFM image b). The sample is grown in sink growth mode as the height increases towards the end of the NW, due to a positive collection area of adatoms from the mask. d) Height profile across the 4 NWs in the array. Again, the sink growth mode is observed due to a higher incorporation of the outer NWs caused by a larger adatom collection area compared to the inner ones.

The sample discussed in figure 4.7 is grown at 516 °C, which is 90 °C lower than the GaAs and GaAs(Sb) NWs presented in section 4.3.1. A hypothesis that explains the observation of the sink growth mode is that at low enough T_{sub}, the kinetics of the adatoms change from performing the preferential transition $\Gamma_{a_c a_m}$ to $\Gamma_{a_m a_c}$. This would imply

$$\left|\frac{d\Gamma_{a_c a_m}}{dT_{sub}}\right| > \left|\frac{d\Gamma_{a_m a_c}}{dT_{sub}}\right|, \tag{4.5}$$

meaning that the adatom kinetics on the NW slows down faster with T_{sub} than on the mask. Also, the differece in atomic mass and chemical potentials between Ga and In adatoms will have an influence on the transition T_{sub} from

source to sink modes. The heteroepitaxial growth from figure 4.7 is almost strain free (0.7% mismatch), excluding strain as a variable to take into account during growth.

The adatom collection area for the sink growth mode is expected to have a symmetric density around the NW, due to the isotropic diffusivity of adatoms on the SiO_2 mask (D_{SiO_2}) since it is an amorphous layer. However, in source growth mode the adatom density of the negative collection area of the NWs is expected to be anisotropic due to the different diffusivity of adatoms in the reconstructed NW crystal surface [128], emitting more adatoms from the boundaries with higher $D_{c,[hkl]}$.

4.3.3 Balanced and mixed growth modes

Balanced growth mode arises when the term $\Delta\Gamma_{a_m a_c} = 0$ in equation 4.3. Although this growth mode is not explicitly reported in this thesis, below are detailed two independent ways of growing reproducible SAG NWs with the same height, similar to the outcome from balanced mode.

The fabrication of SAG NWs for quantum electronic devices usually requires the growth of multi-stack buffer layers to minimize the generation of defects that degrade electronic properties [56]. Specifically, the growth of $In_xGa_{1-x}As$ buffer layers between the substrate and the InAs transport channel has been demonstrated to be beneficial for the strain relaxation of InAs [80]. Using this approach, Figure 4.8 shows two independent methods of engineering arrays of NWs with constant height based on the presented source and sink growth modes.

Figure 4.8a shows an array of lattice matched $In_{0.53}Ga_{0.47}As$ NWs on InP(001) grown at $T_{sub} = 508$ °C. The three outermost NWs are under the influence of the nearby mask, whereas the four middle NWs have a constant height. This approach of growing several NWs homogeneously can be extended by increasing the number of NWs in the array, generating a central region in each array where adatom density is constant. In figure 4.8a, the outermost NWs are the highest in the array. This is caused by the different behavior of Ga and In adatoms of the $In_{0.53}Ga_{0.47}As$ ternary alloy, as opposed to the pure source case observed for a binary semiconductor growth (figure 4.2a). It

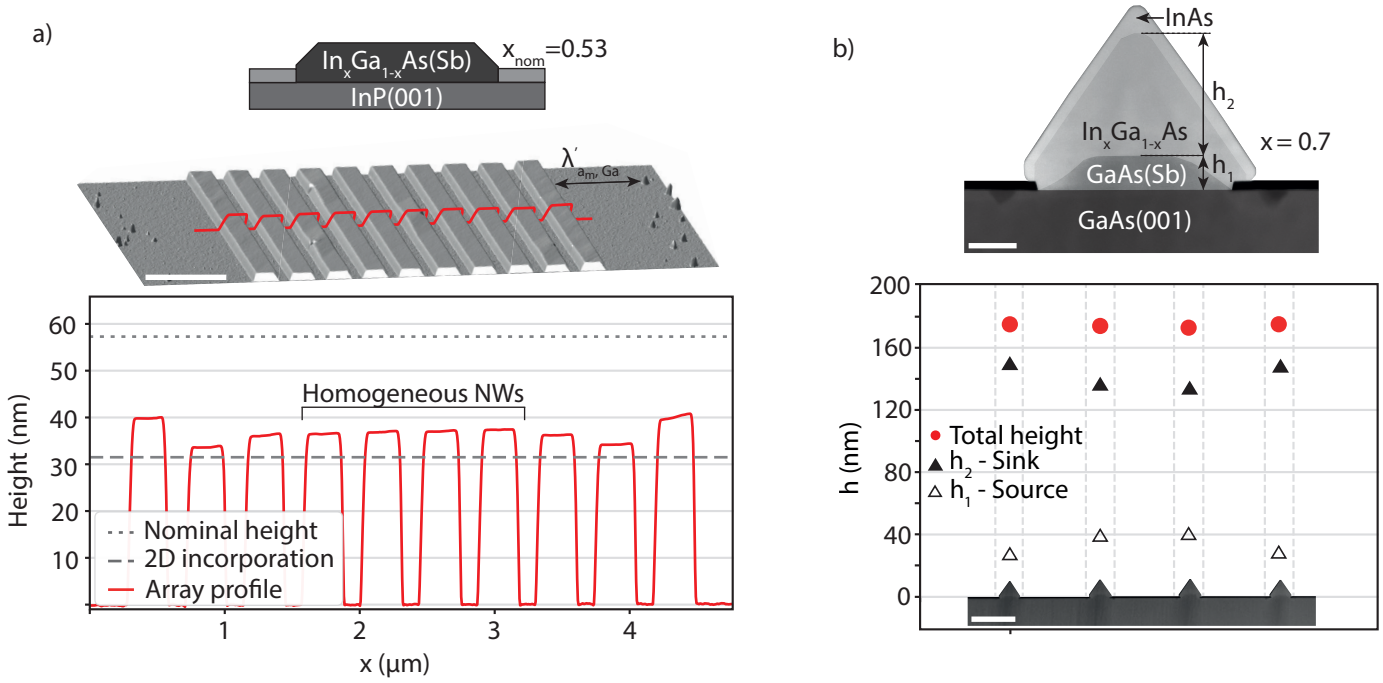

Figure 4.8.: Engineering arrays of NWs with homogeneous height. a) Sketch and AFM image of an array of $In_{0.53}Ga_{0.47}As$ NWs grown on InP(001). In the bottom, AFM line scan across the NWs showing simultaneously both source and sink growth modes, generated by the different group III adatoms. The central NWs of the array form a set of NWs with homogeneous height, due to the formation of an adatom density saturation region. b) HAAD-STEM cross-sectional image of multilayer NWs (top) and low magnification of the NW array (bottom). Material contrast is highlighted for visualization purposes. The plot shows the height of the GaAs(Sb) and $In_{0.7}Ga_{0.3}As$ buffers for each of the 4 NWs in the array, summing up to the same height due to the balanced effect of source and sink growth modes. Scale bars are 1 μm in a), 50 nm in b) (top) and 500 nm in b) (bottom).

is speculated that at the given fluxes and the substrate temperature, the Ga adatoms are incorporated via the source growth mode, whereas simultaneously the In adatoms are incorporated via the sink growth mode (see appendix B for growth conditions). This explains a local sink behavior for the outer NWs and a general source effect for the inner NWs compared to the second and third outermost ones. An implication of this compound growth mode is the possible group III adatom segregation in the different NWs of the array, being In more abundant in the sink regime outer NWs and Ga in the inner ones.

Another approach of growing reproducible structures is presented in Figure 4.8b. The NWs consist of two buffer layers of GaAs(Sb) and $In_{0.7}Ga_{0.3}As$ with an InAs transport channel, grown on a GaAs(001) substrate. The HAADF-STEM image on Figure 4.8b shows the cross-sectional geometry and material contrast between the different layers. The material contrast is highlighted for visualization purposes. The $In_{0.7}Ga_{0.3}As$ composition is extracted by Electron Energy Loss Spectroscopy and its growth temperature dependence has been studied in depth in reference [80]. A cross-section overview of four NWs obtained with TEM is shown as an inset. The white (black) triangles show the height of the first (second) buffers. Here, a combination of source growth mode from the first buffer and sink growth mode from the second buffer generates an array of NWs with constant height, where the subsequent InAs layer is grown on.

4.3.4 Crystallites as mode witness

Crystallites are parasitic crystals nucleating on the mask during growth if the growth conditions such as f and T_{sub} are not inside the selectivity window [57], as described in figure 2.8. During the growth of multilayer NWs each of the layers have their individual selectivity conditions, making it complex and non-trivial to grow selectively on each of the layers [80]. The characterization of these crystallites is important for the optimization of MBE recipes. If the selectivity requirement is not fulfilled during growth, the generated crystallites can be used as witnesses of the growth mode of a specific layer.

Figure 4.9a shows an example of non-selective NWs, which were used to analyze the growth modes. In figure 4.9b, two samples of InAs - $In_{0.7}Ga_{0.3}As$ - GaAs(Sb) NWs are grown at different growth temperatures but otherwise identical growth parameters. Figures 4.9c and d are SEM images of NW networks, where crystallites have nucleated on the mask, implying that the growth conditions were not optimal.

The crystallites in figure 4.9c are formed on the mask at a distance of ~ 3 µm from the structures, indicated by the black arrows. This behaviour suggests that the crystallites were formed during a sink growth mode layer, where the group III adatoms on the mask near the NWs were inside the collection area and incorporated into the NW. Around 3 µm away from the structures, the

a)

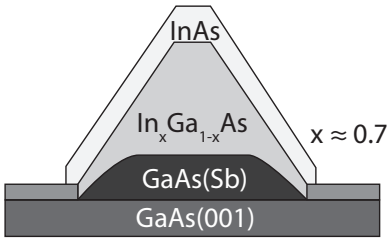

b)

Layer	Growth T (°C) c)	d)
GaAs(Sb)	608	602
$In_{0.7}Ga_{0.3}As$	532	533
InAs	523	526

c)

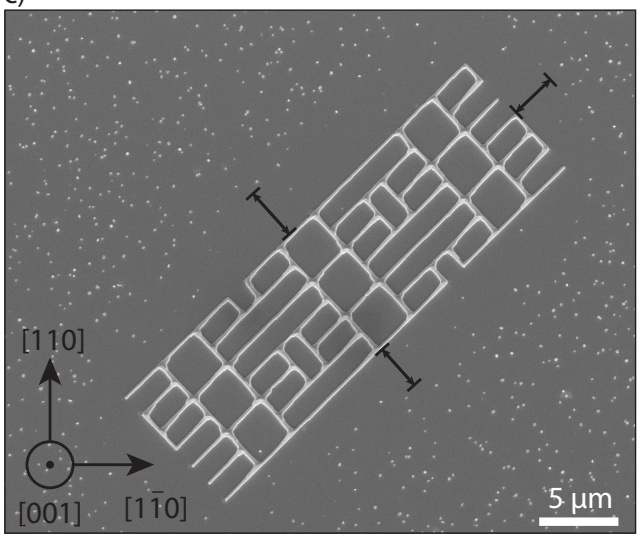

d)

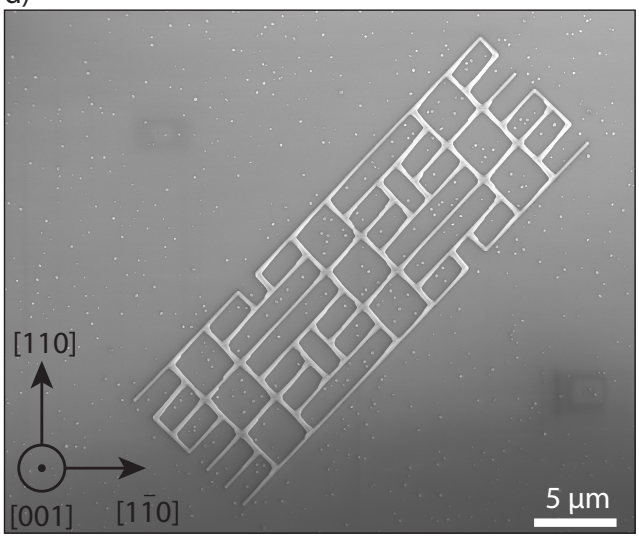

Figure 4.9.: Crystallites as growth mode witnesses. a) Sketch of the layers grown in the two different growths presented in c) and d). b) Table with pyrometer growth temperatures of the samples presented in c) and d), for comparison. c) NW network with parasitic growth on the mask except on a ∼3 µm region around the structure. This is consistent with the generation of crystallites during a layer in sink growth mode. d) NW network with homogeneous parasitic growth around the structure, as well as inside the NW network. In this growth, it is not possible to distinguish the growth mode of the layer or layers that generated the crystallites.

adatom density on the mask was high enough to start nucleating parasitic crystallites. The adatom collection area of the network is $\propto \lambda_{a,m}$, which can be wider than the area without crystallites if the adatom density was high enough to nucleate at the edges of the collection area. Figure 4.9d shows the same network design from a different sample. In this case, the crystallites are homogeneously distributed over the substrate and are found even between the nanowires forming the network. There is no clean area of the mask surface as opposed to the sample in figure 4.9c. Since there is no crystallite growth pattern it is impossible to determine from which growth mode layer they come

from. If they were grown in a source mode layer the adatom density was high enough to nucleate far from the structure and if they were grown in a sink mode layer the adatom density was high enough to nucleate in the collection area near the NWs.

The GaAs(Sb) layer of figure 4.9c is grown at a T_{sub} similar to the ones discussed in figure 4.4, meaning that this layer exhibit source growth mode. The $In_{0.7}Ga_{0.3}As$ layers in both samples were grown at a similar T_{sub}, so it does not explain the different crystallite behaviour. On the other hand, the InAs layer in figure c is grown at slightly lower T_{sub} than d meaning that the sinking growth layer in c was likely to be InAs, also in accordance with the InAs sink results from figure 4.7. Another possible explanation is a difference in the state of the mask between both samples, that affects the adatom kinetics differently between both samples creating this effect.

In these particular cases, the composition of crystallites can be deduced by the observation of growth modes saving time in chemical characterization experiments. In the cases were the crystallites show an inconclusive growth mode (like figure 4.9d), TEM or x-ray photoelectron spectroscopy is needed to determine the composition.

4.3.5 Extended SAG window

The selectivity window for SAG NWs describes suitable growth conditions in the temperature-flux space, as studied by Aseev et al. in reference [57] for GaAs (001) substrates and SiO_2 mask. Based on the results presented in the previous sections, figure 4.10 schematically introduces the effect on the lower boundary (desorption from the crystal, $\Gamma_{a_c v}$) and upper boundary (nucleation on the mask, $\Gamma_{a_m s}$) caused by the Sb surfactant, and the NW design limitation on w. The lower boundary and the upper boundary shift with respect to the standard selectivity window presented in section 2.4. The solid black curves in figure 4.10 represent the upper and lower boundaries and they confine the region in the f - T space where the growth is selective.

From the results presented in figures 4.2 and 4.4, the effect on these boundaries due to the addition of Sb surfactant is the shift to lower temperatures (or higher fluxes), sketched with solid red lines. It is unclear if the shift is identical for

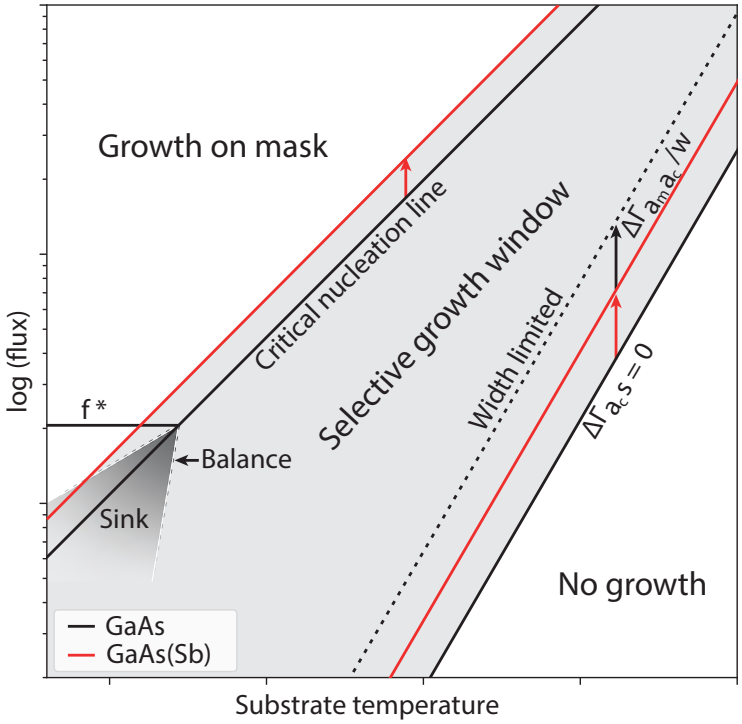

Figure 4.10.: Sketch of the extended SAG growth window and the implications of the source effect. The transition from solid black to solid red lines indicated by the red arrows is caused by the use of Sb surfactant during growth, shifting the $\Delta\Gamma_{a_c s} = 0$ and $\Gamma_{a_m s} = 0$ lines towards lower T. The transition from solid red to dotted black on the $\Delta\Gamma_{a_c s} = 0$ line is caused by the width limitation of the design, additionally shifting it towards lower T. A region of sink growth mode may exist at low f and T, delimited by a line that would be balanced growth mode. Above the sink region maximum flux f*, all growths are expected to be in source mode.

both boundaries since the transition rates defining them might be affected differently by Sb. The growth limitation on the design parameter w shown in figure 4.5 has an implication on the lower boundary by additionally shifting the curve towards lower temperatures by a factor proportional to the strength of the source effect, $\Delta\Gamma_{a_m a_c}/w$. This shift can cause the lower boundary to cross the upper boundary, effectively closing the SAG window as shown in figure 4.5. An important note is that previously reported SAG growths do not account for these effects, implying that by using the standard selectivity window reported in reference [57] it is possible to observe no growth for nanowires of certain width if they are grown in the source growth mode.

Figure 4.10 also speculates about the appearance of a sink region at low f and T where $\Delta\Gamma_{a_m a_c} > 0$ and whose boundary gives balance growth mode

independent of the NW design. The sink window is expected to extend symmetrically beyond the upper boundary towards lower temperatures until the adatom density is sufficiently reduced by nucleation on the mask, entering the source growth mode once more. This localized region in the f - T selectivity map would imply the existence of a critical flux f^* above which it would not be possible to achieve a balanced growth. Further exploration is needed at lower group III fluxes and temperatures of the SAG window in order to demonstrate a balanced growth mode and the existence of the sink effect region for binary materials.

4.4 SAG adatom kinetics models

In this section, two independent models are presented that simulate the experimental observations and predict the existence of different growth modes in SAG. The first is based on coupled adatom diffusion equations in the mask - NW boundary and the second is based in mass conservation calculated from the analytical expression of $\Delta\Gamma_{a_m a_c}$.

4.4.1 Coupled adatom diffusion equations

To simulate the adatom fluxes in this system the adatom diffusion problem is simplified to one dimension by considering only the transversal direction *x* of an array of parallel NWs of infinite length. The steady state adatom diffusion equation for each surface *j* can be written as

$$D_j \frac{\partial^2 \rho_j(x)}{\partial x^2} + f - \Gamma_{a_j v}(x) - \Gamma_{a_j s}(x) = 0, \tag{4.6}$$

where D is the diffusivity of adatoms on the surface j, ρ_j the adatom density on the surface j, and the mask, and crystal surfaces are coupled via boundary conditions for the particular design in question.

Figure 4.11a shows a SEM image of the geometry of four NWs array. The midpoint between the two inner NW ($x = 0$) and at $x = \infty$ are considered as symmetry planes, i.e. $\partial\rho_{a_j}/\partial x = 0$. These symmetry points are marked as red lines in the SEM image. The adatom coupled diffusion equations model

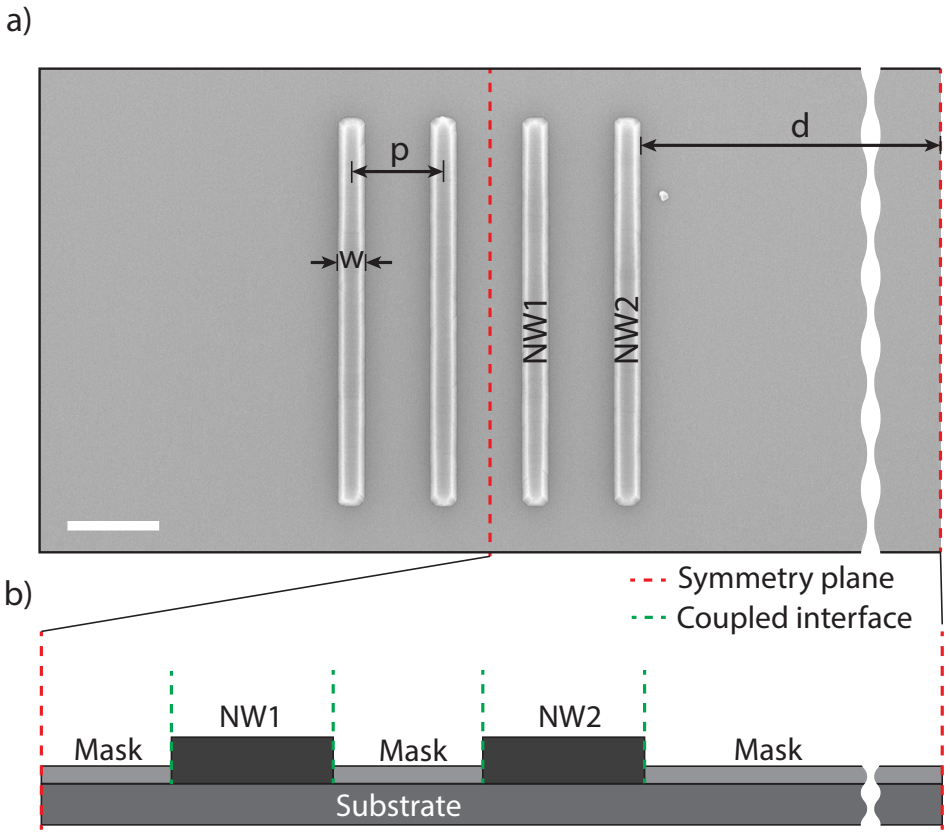

Figure 4.11.: Description of the coupled adatom diffusion equations geometry. a) SEM image of a typical four NW array geometry used in the model. b) Sketch of the NWs and mask regions used in the simulation. The red and green dashed lines describe the position where symmetry planes and coupled adatom density NW - mask interfaces were applied, respectively. For computational simplicity, the simulation was performed only in 2 NWs and applying a symmetry plane in the middle of the array to effectively describe an array of 4 NWs.

presented in equation 4.6 was computed in Matlab using the boundary value problem solver $bvp5c$ (details in appendix D).

Figure 4.11b shows a sketch of the different regions simulated in the model and the location of the symmetry planes and coupled interfaces. At the green boundaries it is imposed adatom density continuity on the crystal and mask, $\rho_{a_c} = \rho_{a_m}$, and mass conservation, $D_c\ (\partial\rho_{a_c}/\partial x) = D_m\ (\partial\rho_{a_m}/\partial x)$. Since the effective incorporation rate is proportional to the adatom density, $\Gamma_{a_c s} \propto \rho_{a_c} \exp\left(-\delta g_{a_c s}/(k_B T)\right)$, ρ_{a_c} can is solved under the approximation of being a measure of the SAG growth rate.

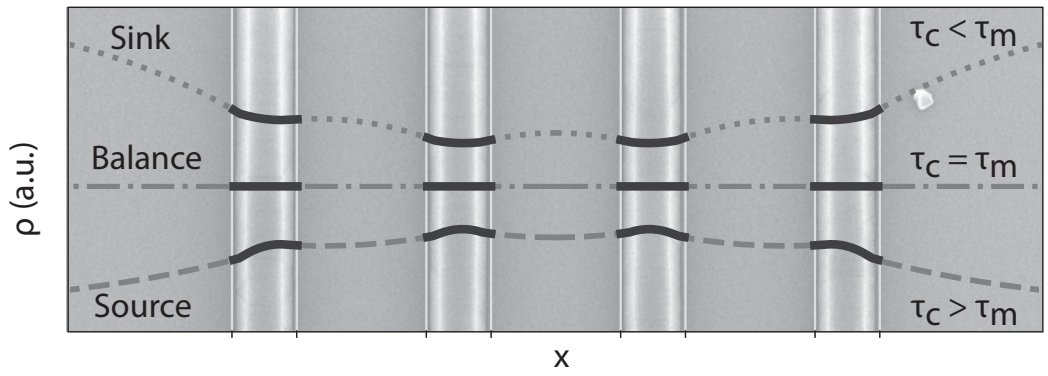

Figure 4.12.: Three types of solutions (sink, balance and source) from the simulation of coupled adatom diffusion equations describing the adatom density ρ on four parallel NWs. The y-axis is adatom density obtained by the model, in arbitrary units. The x axis is the transverse direction through the array of NWs. The dashed and solid lines obtained by the simulation are the adatom density on mask and crystal regions, respectively. Background is a SEM image of an array of 4 NWs for visualization of the different mask-crystal regions.

The model predicts the three general types of growth modes experimentally observed, shown in figure 4.12: sink, balance and source. The model parameters changed in the simulation to obtain different growth modes where $\Gamma_{a_c s}$ and $\Gamma_{a_m v}$, assuming $\Gamma_{a_m s} = \Gamma_{a_c v} = 0$ and keeping the rest of the variables (f, T_{sub} and diffusivities) constant. The relative value of parameters in source mode is $\Gamma_{a_c s}/\Gamma_{a_m v} = 1/3$ and for sink $\Gamma_{a_c s}/\Gamma_{a_m v} = 3$. The balance case is observed when $\Gamma_{a_c s}/\Gamma_{a_m v} = 3$. The model predicts a higher (lower) adatom density, and hence material incorporation, for the sink (source) growth modes, compared to the calibrated corresponding planar growth rate (2D-like growth with no mask). The adatom density gradient appearing near the NWs in the source and sink growth modes is the driving force of the inhomogeneous flux of group III adatoms $\Gamma_{a_m a_c}$ at the boundary, supporting the hypothesis of the cause of these growth modes. These growth modes have been experimentally observed in the figures presented in the previous section 4.3.

4.4.2 Mass conservation model

To understand the influence of T_{sub} on the growth modes, an analytical simulation is performed in Python based on equation 4.3. It models the NW incorporation as a function of T_{sub} by approximating the mask - crystal adatom

flux term $\Delta\Gamma_{a_m a_c}$ as the difference of the diffusion lengths λ on each of the surfaces.

Using the adatom kinetics approach detailed in reference [116], the diffusion length is expressed in terms of mean adatom diffusivity D_a and mean adatom lifetime τ_a. Both D_a and τ_a are expanded on their Arrhenius equations, for mask and crystal. τ_a is a quantity affected by both adatom desorption and incorporation events in the form of $\tau_a = (\tau_{as}^{-1} + \tau_{av}^{-1})^{-1}$. For simplicity, the constant terms f and w in the growth equation 4.3 are normalized to 1 in the model since it only adds a homogeneous offset to the result. Then, equation 4.3 can be written as 4.7, which is the equation used in the simulation:

$$\Gamma_{a_c s} = f - \Gamma_{a_c v} + \frac{2}{w} \cdot \Delta\Gamma_{a_m a_c} \quad \propto \quad f - \Gamma_{a_c v} + (\lambda_m - \lambda_c) =$$

$$= f - \Gamma_{a_c v} + \sqrt{D_{a_m} \tau_{a_m}} - \sqrt{D_{a_c} \tau_{a_c}} = f - c_{a_c v} \exp\left(\frac{-\delta g_{a_c v}}{k_B\, T}\right) +$$

$$+ \sqrt{\frac{c_{D_m} \exp\left(\frac{-\delta g_{a_m a_m}}{k_B\, T}\right)}{c_{a_m s} \exp\left(\frac{-\delta g_{a_m s}}{k_B\, T}\right) + \; c_{a_m v} \exp\left(\frac{-\delta g_{a_m v}}{k_B\, T}\right)}} - \sqrt{\frac{c_{D_c} \exp\left(\frac{-\delta g_{a_c a_c}}{k_B\, T}\right)}{c_{a_c s} \exp\left(\frac{-\delta g_{a_c s}}{k_B\, T}\right) + \; c_{a_c v} \exp\left(\frac{-\delta g_{a_c v}}{k_B\, T}\right)}} \tag{4.7}$$

where the δg_a are the activation energies for the respective adatom state transition and c the constants for each Arrhenius term. These c constants depend on the adatom normalized density on the surface, steric factors and transition attempt frequencies, which for simplicity they are grouped as single pre-exponential parameters. It is assumed that the transition rates obey Arrhenius equations only depending on the activation energy, disregarding entropic terms. The resulting equation depends on T_{sub}, the activation energies δg_a of each transition the pre-exponential constants c.

Figure 4.13 shows a qualitative solution of the model for a given set of parameters δg_a and c. The values of the parameters are detailed in appendix D. The found values of the parameters δg_a and c that generate the modelled curve is probably not a unique set of parameters that models the experimental data.

The vertical axis in figure 4.13 is nominal NW material incorporation Γ_{inc} and the horizontal axis is the growth temperature T_{sub}. At $T_{sub} > 620$ °C the

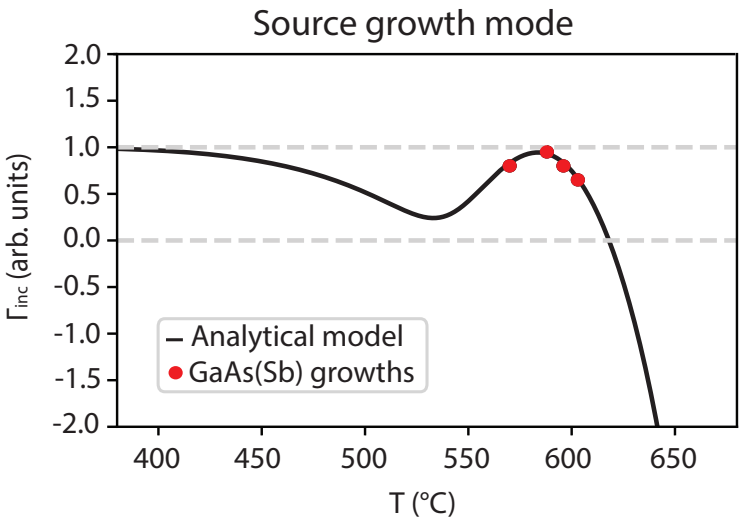

Figure 4.13.: Incorporation in units of nominal incorporation as a function of growth T for a source growth mode. The black line is obtained with the qualitative analytical model described in equation 4.7, where $\Delta\Gamma_{a_m a_c}$ is negative. Red dots are the incorporation measured on isolated NWs presented in figure 4.4.

desorption term $\Gamma_{a_c v}$ dominates, avoiding any incorporation in the NW and even decomposing the substrate at the highest T_{sub} (described by negative growth rates). In the temperature range $540 < T_{sub} < 600$ °C, where $\Gamma_{a_c v}$ is negligible, the growth is dominated by the source effect created by $\Delta\Gamma_{a_m a_c} < 0$, stopping the incorporation curve to reach the nominal incorporation value $\Gamma_{inc} = 1$. The red dots represent the incorporation of individual GaAs(Sb) NWs presented in figure 4.4. The analytical model predicts, in a qualitative way, the reduction of the source effect strength and its increase again at the temperature range $540 < T_{sub} < 580$ °C. At lowest temperature range $T_{sub} < 540$ °C the source effect starts to get weaker due to the slow down of desorption events on the mask, reaching $\Gamma_{inc} = 1$ at the lowest T_{sub}. At this point, parasitic growth will be homogeneously present on the mask.

Figure 4.14 shows the solution of the analytical model for the case of sink growth mode, $\Delta\Gamma_{a_m a_c} > 1$. Similar to figure 4.13, at high T_{sub} the growth is dominated by $\Gamma_{a_c v}$ and substrate decomposition. In the temperature range $500 < T_{sub} < 560$ °C the incorporation is affected by the sink effect, which is able to increase the nominal incorporation above 1. This means that NWs incorporate extra material that is supplied by the flux of group III adatoms coming from the nearby mask, as shown in figure 4.7. At the lower T_{sub} the

incorporation approaches the nominal $\Gamma_{inc} = 1$ as the adatom transitions in the mask - NW boundary are less probable.

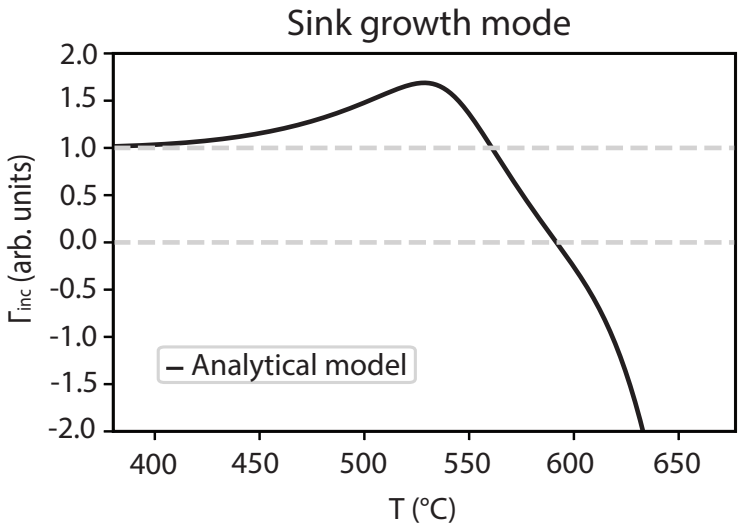

Figure 4.14.: Incorporation in units of nominal incorporation as a function of growth T for a sink growth mode, obtained by the qualitative analytical model presented in equation 4.7. In this regime, the term $\Delta\Gamma_{a_m a_c}$ is positive.

Figure 4.15 shows the solution of the model for the balance growth mode. In this mode, there is no net flux of adatoms in the mask - NW boundary $\Delta\Gamma_{a_m a_c} = 0$ and it only considers $\Gamma_{inc} = 1$ until T_{sub} is high enough to start activating $\Gamma_{a_c v}$ transitions. This case would correspond to the understanding of the SAG growths before reporting the different growth modes.

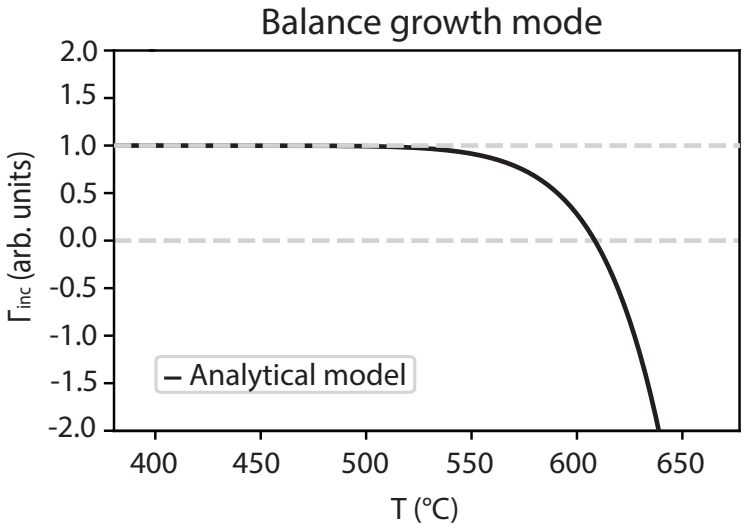

Figure 4.15.: Incorporation in units of nominal incorporation as a function of growth T for a source balance mode, obtained by the qualitative analytical model presented in equation 4.7. In this regime, the term $\Delta\Gamma_{a_m a_c} = 0$.

Since the three solutions to the analytical model describe the incorporation of NWs at a constant f, they can be understood as horizontal lines in the SAG window, figure 2.8. At high T_{sub}, the growths enter the NW desorption regime and at low T_{sub} the mask incorporation. An important outcome of the previous sections is that there is faint structure inside the selectivity window which describes different growth modes while still being selective, supported by the experimental data and models.

4.5 NW faceting

NW faceting is the crystal mechanism to minimize their surface free energy, until achieving what is known as equilibrium shape [129]. Its understanding and control are crucial for SAG based topological qubits due to the necessity of depositing superconductor layers on semiconductor facets to generate the topological phase [44]. The use of different substrate out of plane orientation determines which set of facets a growing NW can develop, topic extensively reported in the past [130–132]. In this thesis, (001) substrates are used due to the high symmetry set of facets that SAG NWs develop during MBE growth. However, other orientations have been reported in the past to study the quality of the grown SAG structures, such as on: (111) [57], (011) [106] or (113) [133].

In order to understand the facet evolution during the growth of $[1\bar{1}0]$ SAG NWs on (001) substrates, three cross-sectional FIB lamella cuts are performed on NWs with different w. The NWs are grown under similar conditions of T_{sub}, group III flux and growth time. Figure 4.16 shows three sketches showing the layer composition of the three HAAD-STEM images below, from three different $In_{0.7}Ga_{0.3}As$ - InAs NWs. Each of the NWs have a different w, being 235 nm, 120 nm and 75 nm for figure 4.16a, b and c, respectively. Although the NWs come from different samples, 4.16c being grown in a substrate with different chemical composition, it is expected that it will not have an impact on the later stages of the facet evolution of the NWs during their growth. It is assumed that growing the same NW volume on a different w mask opening is equivalent to grow different amounts of material on the same w mask opening.

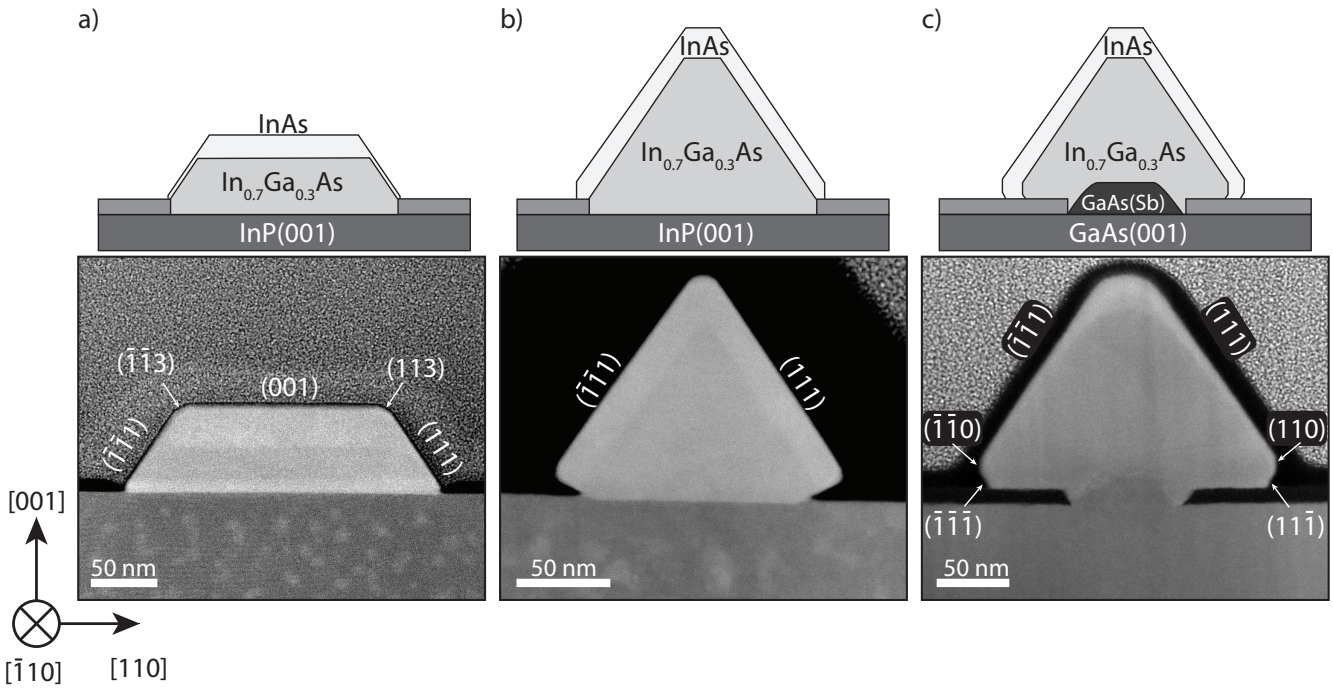

Figure 4.16.: NW faceting change during growth. a) 235 nm wide NW with dominant $\{111\}$ and (001) facets. A pair of $\{113\}$ micro facets appear connecting the $\{111\}$ and (001). b) 120 nm wide NW with fully formed $\{111\}$ facets. This NW has reached the crystal equilibrium shape. c) 75 nm wide NW overgrowing over the mask.

Figure 4.16a shows a NW with $\{111\}$ side facets and (001) top facet, consistent with the faceting of an early growth stage where the NW has not reached the equilibrium shape. 4.16b shows a thinner NW with $\{111\}$ side dominant facets. 4.16c shows the thinnest NW also with $\{111\}$ side dominant facets while overgrowing over the SiO_2 mask. The fact that the faceting is the same in 4.16b and 4.16c, but only overgrowing over the nearby mask, implies that $\{111\}$ with minor $\{113\}$ facets connecting both on top is the equilibrium shape of $In_{0.7}Ga_{0.3}As$ - InAs NWs grown on (001) substrates. In terms of adatom lifetimes, τ_{a_cs} would have a local maximum value for (001) planes, a higher local maximum value for $\{113\}$ and the highest maximum value for $\{111\}$.

The importance of facet evolution during NW growth is shown in figure 4.17. Figure 4.17a is an AFM image of an InAs NW grown in GaAs(Sb), from the same sample discussed in figure 4.7, and 4.17b is the same AFM image with NW facets color coded. Since the NW is grown in sink growth mode, the longitudinal end parts incorporate more adatoms, due to their bigger collection

areas, than the central parts of the NW. This extra incorporation has an effect on the faceting, allowing the end parts to reach a state of faceting closer to equilibrium shape than the middle part. This can be seen by an increase of $\{111\}$ facets (red) at the NW ends and a majority of $\{113\}$ (blue) and (001) (yellow) facets in the middle.

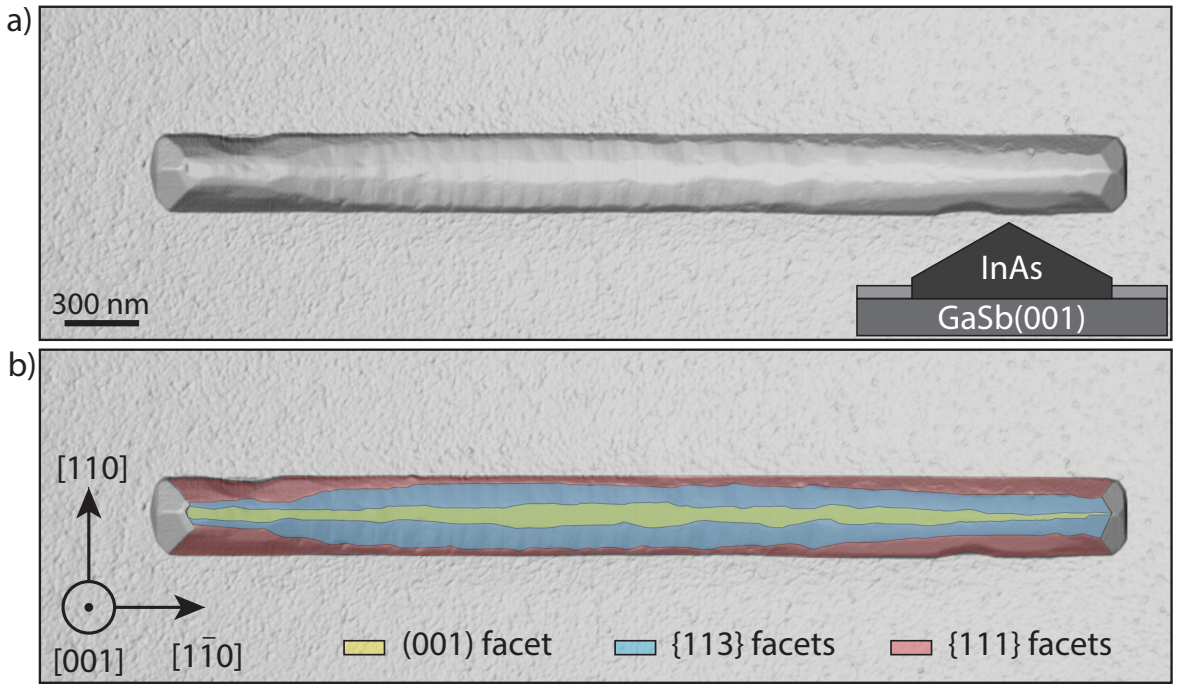

Figure 4.17.: InAs NW grown on GaAs(001), from the same sink growth mode sample presented in Figure 4.7. a) AFM image of an InAs NW oriented along $[1\bar{1}0]$. b) Same AFM image with color coded facets, showing the facet evolution caused by the sink growth mode.

Figure 4.18a is an AFM image of the corner of a 10x10 μm mask opening from a GaAs(Sb) sample grown at 570 °C. The data about crystal adatom desorption during growth presented in figure 4.4 is measured in this type of big mask openings. Using the mask as a reference height, the volume of a 5x5 μm square is measured and compared with the equivalent volume from a planar growth sample used for growth rate calibrations.

AFM height line scans are performed on both $[1\bar{1}0]$ and $[110]$ edges of the structure, shown in figure 4.18b. Both profiles show an increase of incorporation near the edge of the structure, compared to inside the structure. Along the $[1\bar{1}0]$ this increase in incorporation spans over 715 nm inside the structure, whereas for $[110]$ spans for 220 nm. These results are consistent with a pref-

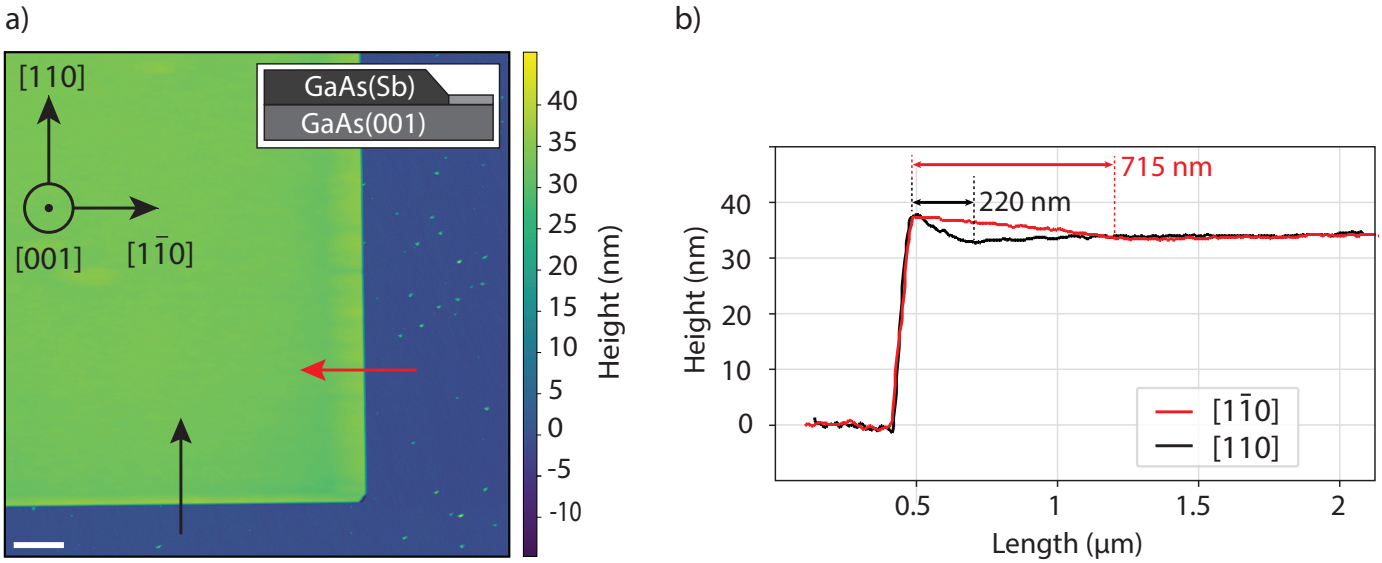

Figure 4.18.: Adatom diffusion from $\{111\}$ to (001) facets of GaAs(Sb) grown on GaAs(001). a) AFM image of a large mask opening comparable to a 2D growth, used for alignment purposes during lithography. Scale bar is 2 μm. b) Height profiles along the $[1\bar{1}0]$ (red) and $[110]$ (black) directions on the 2D-like structure.

erential adatom diffusion from $\{111\}$ side facets towards the (001) top facets, due to $\tau_{a\{111\}} > \tau_{a(001)}$ [134]. This extra source of adatoms towards the inside of the structure penetrates until they are finally incorporated in the NW. The different penetration length is directly related with the longer diffusion length of adatoms on GaAs (001) along the $[1\bar{1}0]$ than $[1\bar{1}0]$, as discussed in figure 4.2.

Figure 4.19a shows an AFM image of an array of four GaAs(Sb) on GaAs(001) NWs oriented along the $[1\bar{1}0]$. The growth T_{sub} was 537 °C, reason for the appearance of parasitic growth around the NWs. Figure 4.19b is a transversal line scan taken on the four NWs along the red line described in a. The height profile of the NWs show a convolution between two different effects. The fact that the outer NWs grown less than the inner ones implies that the growth is source $\Delta\Gamma_{a_m a_c} < 0$, in agreement with the analytical model 4.13. At the same time, each NW has a preferential overgrowth at the sides of each NW. This is a different manifestation of the preferential diffusion of adatoms from the side of the NW towards the top facets shown in figure 4.18. This is probably caused by the very low T_{sub} making an adatom diffusion length comparable to the width of the NW. It is remarkable that NWs in this sample expel adatoms

to the mask due to the source growth mode and at the same time there is a flux of adatoms from the side facets towards the inner top one.

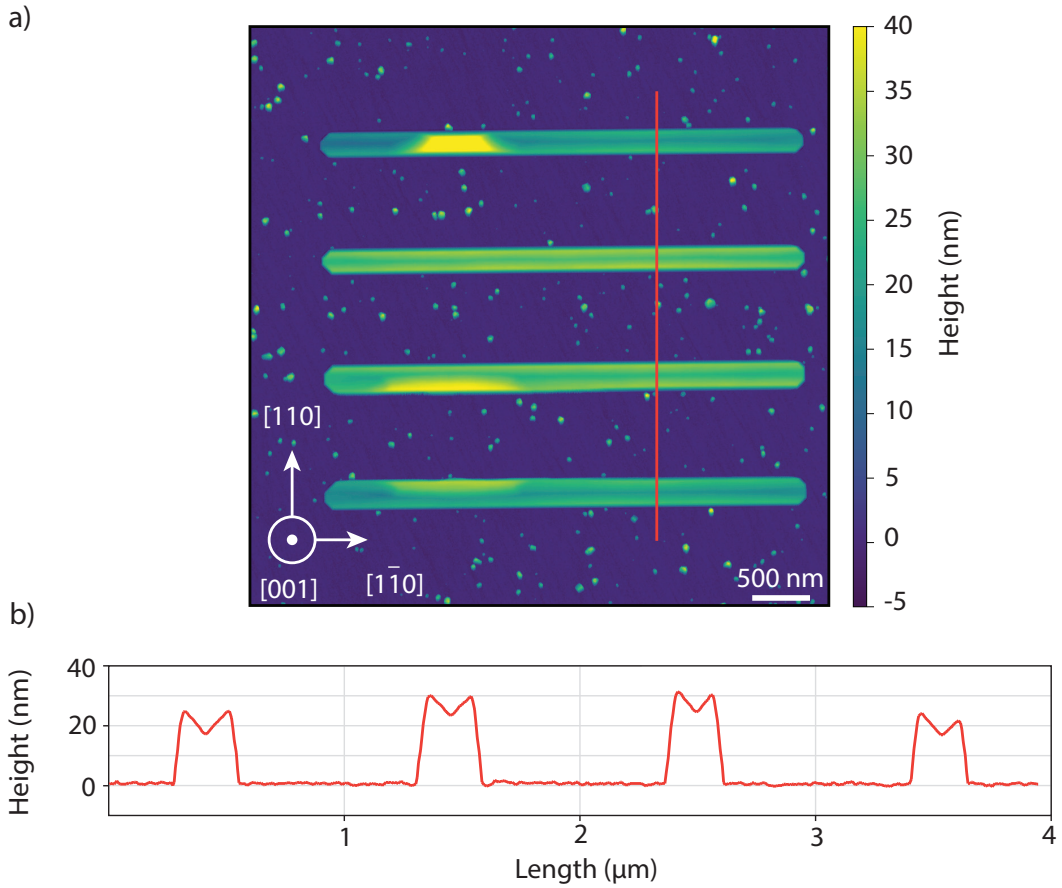

Figure 4.19.: Adatom diffusion from $\{111\}$ to (001) facets on NWs from the same sample as the one discussed in Figure 4.18. a) AFM image of four GaAs(Sb) NWs array along $[1\bar{1}0]$. b) Height profile across the four NWs, showing an increase in incorporation on each side of the NWs.

4.6 Effect of Sb surfactant on adatom kinetics

Homoepitaxial growths show a Frank-Van der Merve or step-flow growth mode due to the lack of crystal strain. These growth modes rely on a sufficiently long surface diffusion length for the adatoms reach an island edge and incorporate in an edge site, i.e. a sufficiently high T_{sub} is required. If the adatoms have a diffusion length shorted than the mean terrace width, adatoms will nucleate in terraces creating new monolayers before completing the older ones. This

change to Stranski-Krastanov growth mode is undesired because it generates a rough growth front, whereas the homogeneity requirements on the NW morphology for qubit applications are very demanding.

The use of surfactant during MBE growth of GaAs has been studied in the past [135–137]. Surfactants are adatoms of a different species than the homoepitaxial growing layer that reduce the surface energy, change the surface reconstruction and modify the surface kinetic processes [138]. They also diffuse to the growth front via exchange mechanism [139], offering little or no incorporation into the homoepitaxial film.

Figure 4.20 shows two SEM images of arrays of pure GaAs and GaAs(Sb) surfactant grown along $[1\bar{1}0]$ on GaAs(001). Sb is used as a surfactant due to its low vapor pressure and its low degree of incorporation in the NWs [56]. The GaAs NWs exhibit rough $\{113\}$ side facts, whereas by adding Sb surfactant the faceting changes to a smooth top (001) facet. The reduction in the surface energy and the increase of the Ga adatoms diffusion length caused by the Sb promotes a step-flow growth mode of the original (001) planes, for high enough T_{sub}. Sb, as non-reactive surfactant, is expected to occupy adatom sites in the growing GaAs layer forcing Ga adatoms to find other incorporation sites, hence increasing the lifetime and diffusion length.

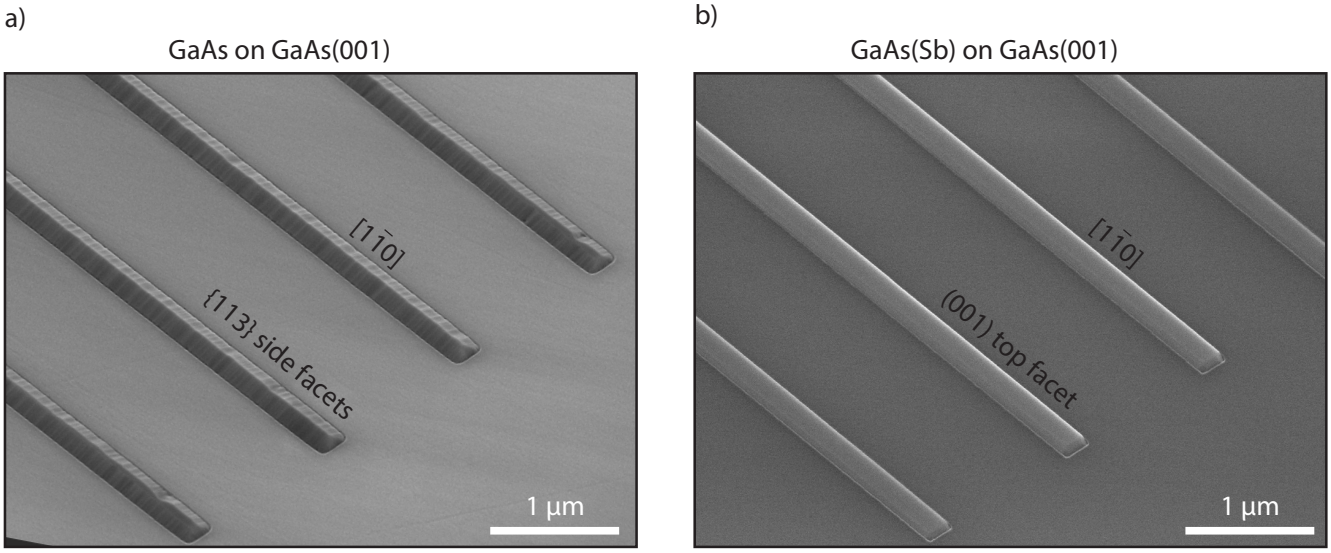

Figure 4.20.: Effect of Sb surfactant on NW facets. a) SEM image of GaAs NWs along $[1\bar{1}0]$ with dominant and rough $\{113\}$ facets. b) SEM image of GaAs(Sb) NWs along $[1\bar{1}0]$ with dominant $[001]$ top facet.

The change on the adatom kinetics caused by Sb surfactant also has an impact on the growth mode, as discussed in figure 4.2. This makes surfactants another variable to have into account for optimizing the morphology of NW networks.

Figure 4.21 shows AFM height line scans of a GaAs (black) and GaAs(Sb) (red) NWs inside arrays, along $[1\bar{1}0]$. These NWs come from the samples discussed in the source growth mode figure 4.2, which explains the reduction of incorporation when approaching the end part, specially in the pure case. The Sb surfactant NW is able to incorporate a more homogeneous amount of material along its length, caused by the induced change in faceting and the increased adatom diffusion length $\lambda_{a,c}$. For this reason, the volume measurements of NW incorporation presented in the previous sections were performed in the middle part of NWs with $l \gg \lambda_{a,c}$. If the NW length is comparable to $\lambda_{a,c}$, the use of surfactants can override the effect of the growth mode due to a homogenization of the adatom density in the whole NW.

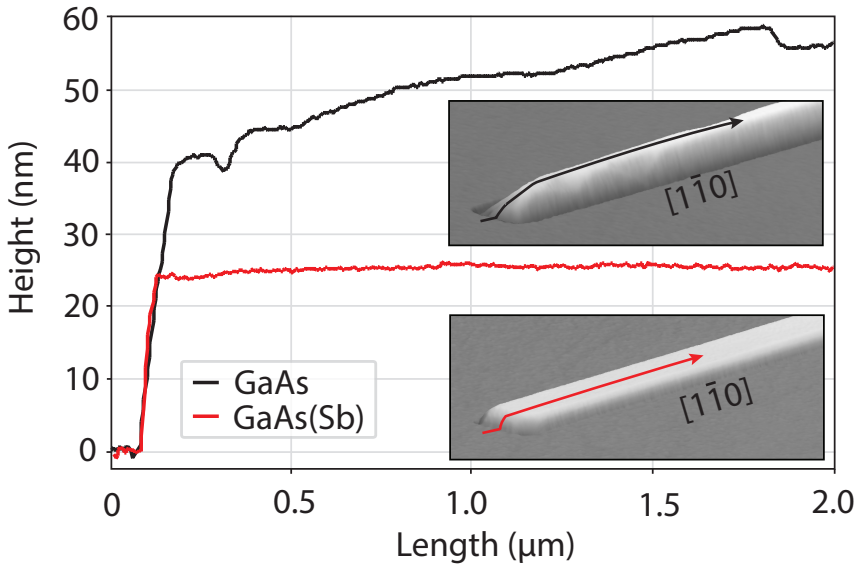

Figure 4.21.: AFM longitudinal height profiles of a 4 μm long GaAs NW (black) and GaAs(Sb) (red) (discussed in Figure 4.2) along $[1\bar{1}0]$.

4.7 Source effect on quantum dots

Quantum dot (QD) structures are required in the Karzig's platform approach for topological computing for reading the states of MZMs [60]. Using the same approach than with NWs, SAG based QDs can be grown [99]. Figure 4.22

shows SEM images of an array of 11 $\times$ 11 GaAs(Sb) - InAs QDs of diameter $d = 100$ nm grown on GaAs(001) under similar MBE conditions to other samples reported previously showing source growth mode (details in appendix B). In figure 4.22b, the outer NWs of the array are ungrown due the strength of the source effect. As opposed to NWs, where the longitudinal dimension is $> \lambda_{a,c}$, adatoms in QDs have a higher probability of doing the transition $\Gamma_{a_c a_m}$ since $d \ll \lambda_{a,c}$. On the other hand, the QDs in the middle of the array can grow both layers due to the collective creation of an adatom saturation region high enough to allow nucleation on the crystal, as shown in figure 4.22c.

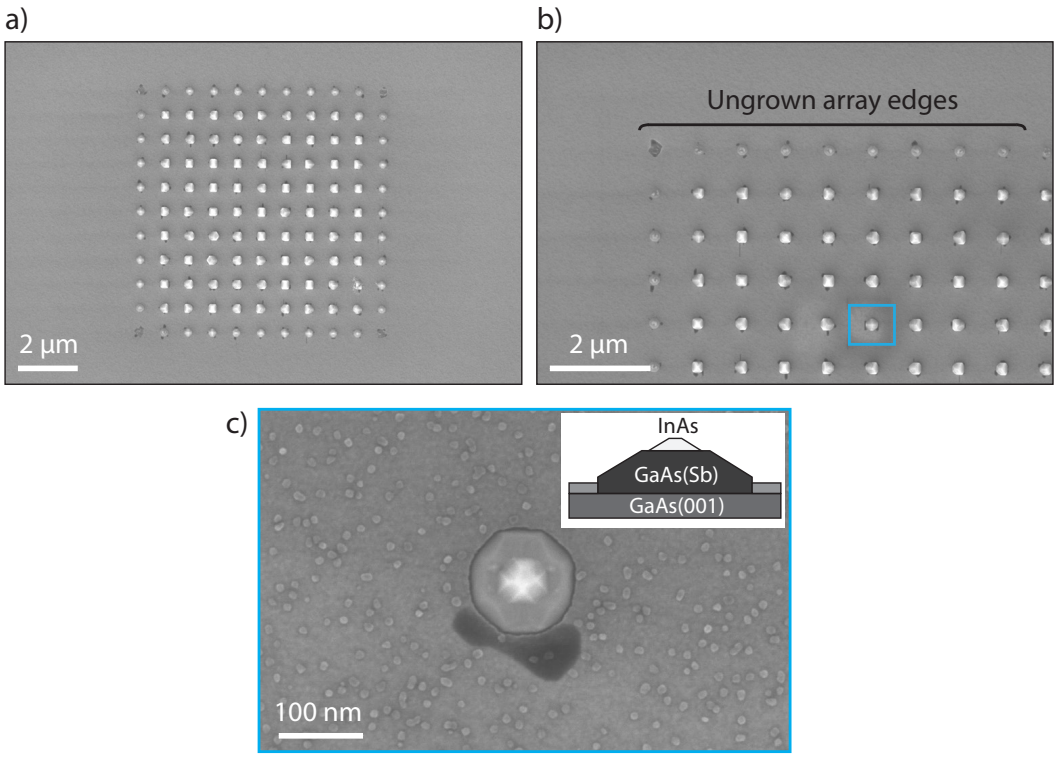

Figure 4.22.: Source effect in positioned InAs Quantum Dots grown on GaAs(001). a) SEM image of an array of 11 $\times$ 11 QDs. b) SEM image of the edge of the array, where the outer most QDs do not grow due to the source effect. c) SEM zoom in image of a QD on the middle of the array, where the faceting of both the buffer and InAs can be observed.

In the case of NWs, the growth mode term in equation 4.3 $\Delta\Gamma_{a_m a_c}$ was weighted by the width of the NW $\Delta\Gamma_{a_m a_c}/w$. However, in the case of QDs due to their geometry, it is expected to be $\propto \Delta\Gamma_{a_m a_c}/d^2$ making the source effect more intense. It is also expected some residual InAs growth on the QDs placed at the edge of the array due to the higher positive collection area in sink mode, similar to figure 4.7.

4.8 Conclusions and outlook

SAG growth rates are measured and analyzed for GaAs, GaAs(Sb), $In_xGa_{1-x}As$ and InAs NWs on GaAs, InP and GaSb SiO_2 patterned substrates. The results show how the growth rates are dominated by the effective flux of adatoms across the mask to crystal areas, $\Delta\Gamma_{a_m a_c}$, where its sign determines whether the growth is in source (negative), balanced (neutral) or sink (positive) growth mode. The type of growth mode is determined experimentally and by measuring the NWs growth rate it can be concluded its dependency on the variables: NW array pitch, position in the array, width, crystallographic orientation and chemical composition.

With the growth conditions used in this study, GaAs and GaAs(Sb) grow consistently in source mode while $In_xGa_{1-x}As$ and InAs grow effectively in sink mode. The results demonstrate the possibility of growing reproducible NWs by two different approaches: tuning the growth mode of each group III species on buffer layer stacks and by increasing the number of NWs in the array, creating an incorporation saturation region for the inner ones.

The implications of the growth modes on the growth of reproducible NW arrays and networks are remarkable. Facets can get affected by the differential incorporation caused by the growth mode at the NW end parts as shown for InAs NWs growing in sink mode. For GaAs(Sb)-$In_{0.7}Ga_{0.3}As$ multi-stack samples it is demonstrated, at the given growth conditions, the compensation between both sink and source growth regimes, leading to possible chemical composition inhomogeneities between NWs in the same array. This implies that to reproducibly grow SAG NWs of varying design, the growth mode must be taken into account. The use of surfactants also affect the intensity of the growth mode, having a beneficial effect for GaAs(Sb) compared to pure GaAs NWs due to the substantial increase of $\lambda_{a,c}$. NW junctions are expected to show an reduction of the growth mode strength compared to single NWs. The decrease of available mask and the availability of two diffusion directions for adatoms around junctions should allow for a local increase in incorporation in source mode and a decrease in sink mode.

Further studies are required at the SAG window region of lower group III fluxes and T_{sub} to confirm the existence of an accessible sink mode window for

GaAs SAG growths. It is also expected that, at the same f and T_{sub} conditions used for the growths explained in this chapter, using a different substrate out of plane orientation will cause a different strength of the reported growth modes due to different $\lambda_{a,c}$.

5 Nanowire Defect Characterization

The overlapping data from this chapter with Publications 2 and 3 (publications in preparation) are adapted with the permission of the collaborating authors.

5.1 Introduction

MZM created in the induced topological gap of hybrid semiconductor superconductor NWs are protected against the disorder created by the local environment, as discussed in chapter 1.1. However, crystal defects in the semiconductor can generate perturbations in the internal chemical potential. These defects can have different nature: defects in the crystal lattice such as misfit dislocations and stacking faults [140], charge impurities added during growth [141] or chemical inhomogeneities of the materials [80].

The effect of defect caused disorder on the MZM field has attracted considerable attention lately. Recent publications based on simulations claim that the estimated potential perturbation of a single charge impurity contained in the crystal lattice of the semiconductor is on the order of $\sim$ 1 meV, the same as the topological gap created in reported hybrid NWs [142]. However, MZMs can still exist, due to screening of charge impurities by the proximitised superconductor in the hybrid NW, by screening the potential of the charge impurity [143]. The latest estimations of the upper limit of charge impurity density in NWs to show MZMs is 15 per µm (10^{15} cm^{-3}) [141]. Taking into account the typical impurity levels of MBE grown III-V semiconductors [144], this would imply that the MZM signatures reported results in the last years [59,

145] are likely to be Andreev bound states (ABS) generated by disorder inside the topological gap. Unlike MZM, ABS have conventional fermionic properties and do not obey non-Abelian statistics. These investigations produced the recent revision of the experimental data and later retraction of one of the most promising articles regarding the observation of MZM [146, 147].

It is expected that other crystal defects would be (in the same way as charge impurities) detrimental to the generation of MZMs. For this reason, the characterization of crystal defects is a critical factor in order to develop Karzig's platform for topological computing [60]. This chapter will describe the influence on the semiconductor properties of the two most common defects appearing in SAG NWs: stacking faults and dislocations.

5.2 Effects of stacking faults on electronic transport properties

Stacking faults and twin planes are planar defects in the crystal structure of ZB and WZ III-V semiconductors. Figure 5.1a shows a HAADF-STEM cross-section image of an GaAs(Sb) - InAs - $In_{0.7}Ga_{0.3}As$ SAG NW, grown on GaAs(001) substrate. Due to the strain generated in the $In_{0.7}Ga_{0.3}As$ - GaAs(Sb) lattice mismatched interface, misfit dislocations are formed. These dislocations usually trigger the formation of a stacking fault plane, as explained later in figure 5.6.

Figure 5.1b is a high magnification image of the green square in 5.1a, showing the atomic structure at the InAs - $In_{0.7}Ga_{0.3}As$ interface. The main reason for growing the InAs transport channel on top of two buffer layers is to elastically relax the 7.2% lattice mismatch between InAs and GaAs. Most of the misfit dislocations will be generated in the highly mismatched interface $In_{0.7}Ga_{0.3}As$ - GaAs(Sb), enabling a plastic relaxation of the strain. The remaining mismatch between InAs and $In_{0.7}Ga_{0.3}As$ can be accommodated by the InAs elastically [56]. However, a stacking fault generated by a misfit dislocation at the $In_{0.7}Ga_{0.3}As$ - GaAs(Sb) interface propagates through the crystal until it penetrates into the InAs transport channel.

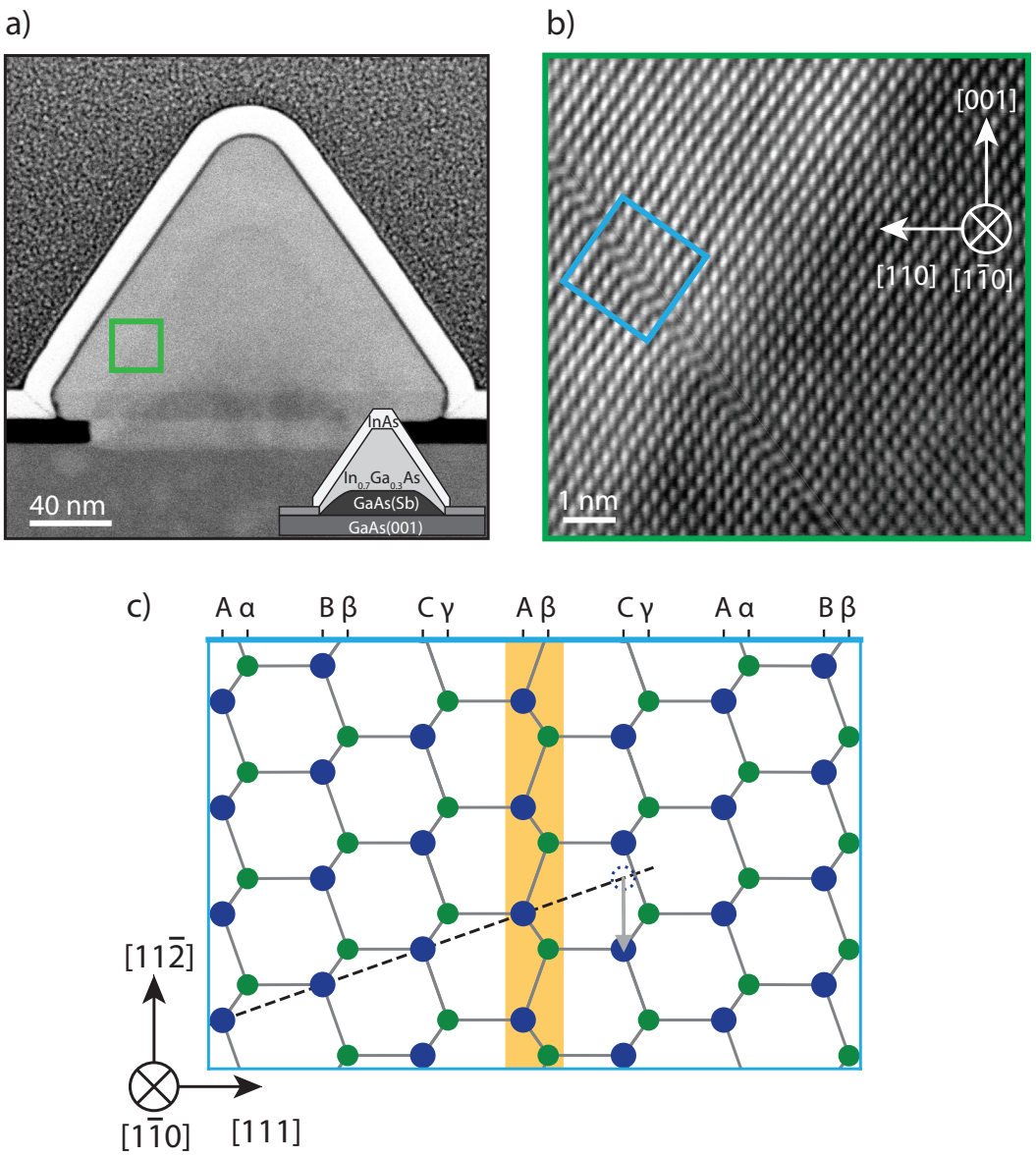

Figure 5.1.: a) Cross-section HAADF-STEM image of an InAs - $In_{0.7}Ga_{0.3}As$ - GaAs(Sb) NW. The zone axis is $[1\bar{1}0]$. b) High magnification of the green square in a), showing how the stacking fault generated in the lattice mismatched $In_{0.7}Ga_{0.3}As$ - GaAs(Sb) interface penetrates into the InAs layer. c) InAs atomic model from the blue square in b), where blue dots are In atoms and green dots are As atoms. The latin letters label the In monolayers stacking sequence and the greek letters the As monolayers stacking sequence. A stacking fault is marked by the yellow region, where an $A\alpha$ bilayer is substituted by an $A\beta$. The blue dashed circle shows the position where the In atom in that column would be without the stacking fault defect.

The zincblende (ZB) crystal structure can be described as a stacking sequence of (111) planes of group III and group V atoms, as discussed in chapter 2.1. Figure 5.1c is a model of the atomic arrangement in the blue square from 5.1b, with In being the blue atoms, As the green atoms and a stacking fault marked in yellow. Each of the bilayers are described with latin characters referring to As atoms and greek characters for In atoms. On a perfect ZB crystal the stacking sequence of (111) planes is Aα-Bβ-Cγ-Aα-Bβ-Cγ... However, in this case the stacking fault introduces an erratic bilayer Aβ in the position of an Aα. After the stacking fault the crystal continues the correct stacking sequence, with a shift of $-2/3 \cdot a_{[11\bar{2}]}$(InAs) along $[11\bar{2}]$ compared to the original crystal.

In order to simulate the impact of the stacking fault to the InAs semiconductor properties, numerical simulations based on density functional theory (DFT) are performed in the freeware Quantum ESPRESSO [148, 149]. It is an optimized tool for materials modelling and electronic structure calculations based on DFT and many-body perturbation theory, widely used by the materials research community. Appendix D contains the details about the simulations performed in Quantum ESPRESSO.

Figure 5.2a shows the definition of the InAs crystal unit used for the DFT calculation of density of states (DOS), containing the stacking fault (yellow) and correctly stacked with three bilayers (purple). The experiments were done varying the number of clean units at both sides of the stacking fault. Bulk contact leads are attached at both extremes of the structure (green dotted rectangles in figure 5.2b).

To evaluate the effect that the stacking fault has on the semiconductor properties of the InAs, the DOS are calculated at the stacking fault location in figure 5.3a and 11 units of clean crystal away from the stacking fault in figure 5.3b. The horizontal axis describes the crystallographic directions along which the DOS has been calculated, from $\bar{X}$ to Γ ending at $\bar{K}$. The vertical axis is the energy of the band, normalized to the valance band maximum. The color scale describes the DOS in arbitrary logarithmic units.

At the stacking fault location there are no electron states penetrating into the band gap, conserving this important property of the semiconductor. This situation is maintained at a distance of 11 units of crystal, in figure 5.3b. By comparing both DOS, the only appreciable difference is the generation of a

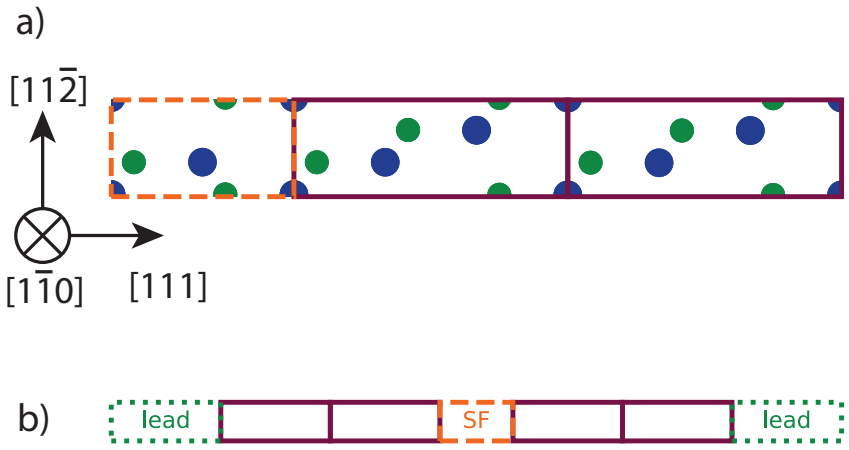

Figure 5.2.: Crystal unit definitions used for the DFT simulation of DOS. a) The dashed orange box contains the stacking fault layer and the purple boxes contain a crystal unit of 3 correctly stacked layers. b) Sketch of the crystal arrangement used for the experiments, with a varying number of purple boxes at both sizes, the stacking fault in the middle part and the contact leads at both ends.

localized state in the conduction band at ∼1 eV above the conduction band minimum at the stacking fault plane. This difference is not expected to have an appreciable negative impact on the InAs properties required for device measurements.

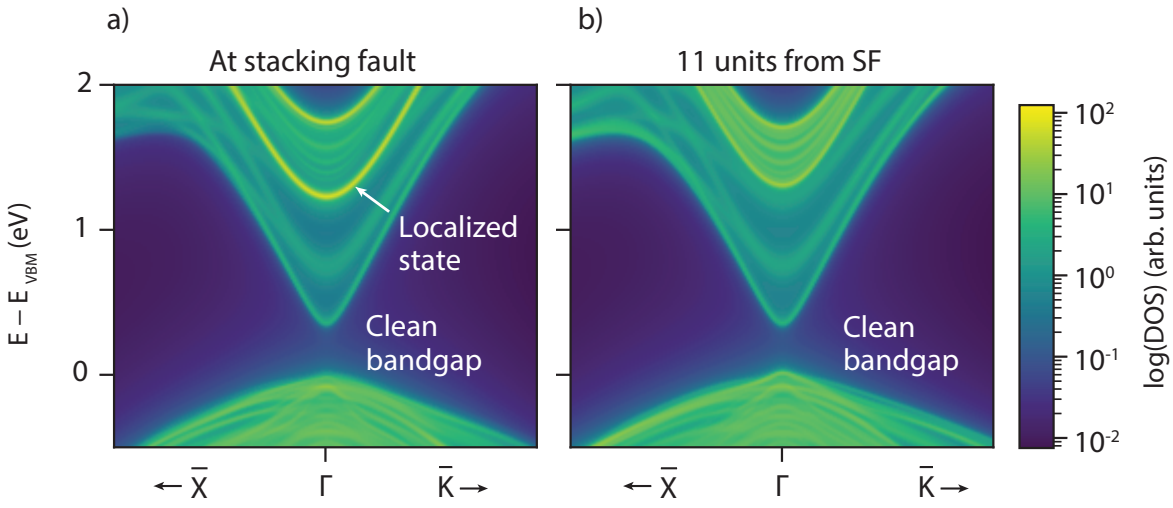

Figure 5.3.: DOS calculation. Y axis energy units are offset to have at 0 eV the valence band maximum energy. a) DOS at the stacking fault location, with no states penetrating the band gap. b)DOS 11 crystal units (defined in Figure 5.1) away from the stacking fault, also with no states penetrating the band gap and a similar state distribution than in a).

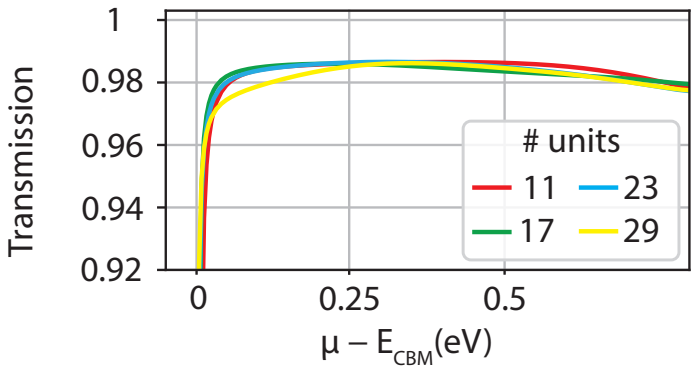

Figure 5.4.: Electron transmission across a stacking fault. The chemical potential axis is offset for the conduction band minimum energy to be at 0 eV. The plot shows that the transmission decreases by 2% caused by a stacking fault, for NWs simulated with different amount of crystal units.

The electron transmission perpendicular to the stacking fault is a crucial parameter that can affect the electronic device properties of these NWs. Figure 5.4 shows the electron transmission perpendicular to the stacking fault as a function of the electron energy, normalized to the energy of the conduction band minimum (CBM). Similar experiments are usually performed for superconductor junctions in hybrid NWs, where a transmission (or transparency) value as close to 1 as possible is desired for a good performance of the NW devices [48]. The calculation is performed with a different number of clean crystal units, shown as purple boxes in figure 5.2b. For simplicity, it is considered a strain free structure. This approach is not expected to have a big impact in the results, since the stacking fault changes the local lattice parameter by $< 0.3\%$ from previous DFT studies in ZB crystals [150].

The electron transmission is almost undisturbed by the stacking fault, with a $\sim$ 2% decrease and a similar behaviour between the simulations with different number of clean crystal units. It is unknown if the piling of more stacking fault along the NW would cause a cumulative detrimental effect in transmission, although such scenario is expected. The fact that no electron is transmitted for energies $\mu < E_{CBM}$ is because they have lower energy than the InAs band gap. Although the crystal used for the calculation does not define very accurately the NW geometry presented in figure 5.1, it gives a valuable notion about the effect of stacking faults on electronic transport measurements of real SAG NWs. Since stacking faults are a coherent planar defect, all the electronic bonds from the stacking fault plane are bonded towards both sides, making a non destructive impact on the semiconductor properties.

5.3 Effects of dislocations on the semiconductor band structure

The other most common crystal defect appearing in SAG NWs are misfit dislocations. Due to the lattice mismatch between the stress-free GaAs(001) substrate and the InAs that will be used as transport channel, NWs will create a periodic array of misfit dislocations at mismatched interfaces [140, 151, 152]. To minimize their impact on transport measurements, buffer layers with lattice parameter closer to InAs are grown in between. Ideally, with the buffer strategy the strain can be accommodated by plastic relaxation in the GaAs(Sb) - $In_{0.7}Ga_{0.3}As$ interface and burying the dislocations underneath the buffer moving them away from the InAs [56]. In principle, the remaining misfit between $In_{0.7}Ga_{0.3}As$ - InAs can be accommodated as elastic strain by rotation of the epitaxial planes of InAs [80].

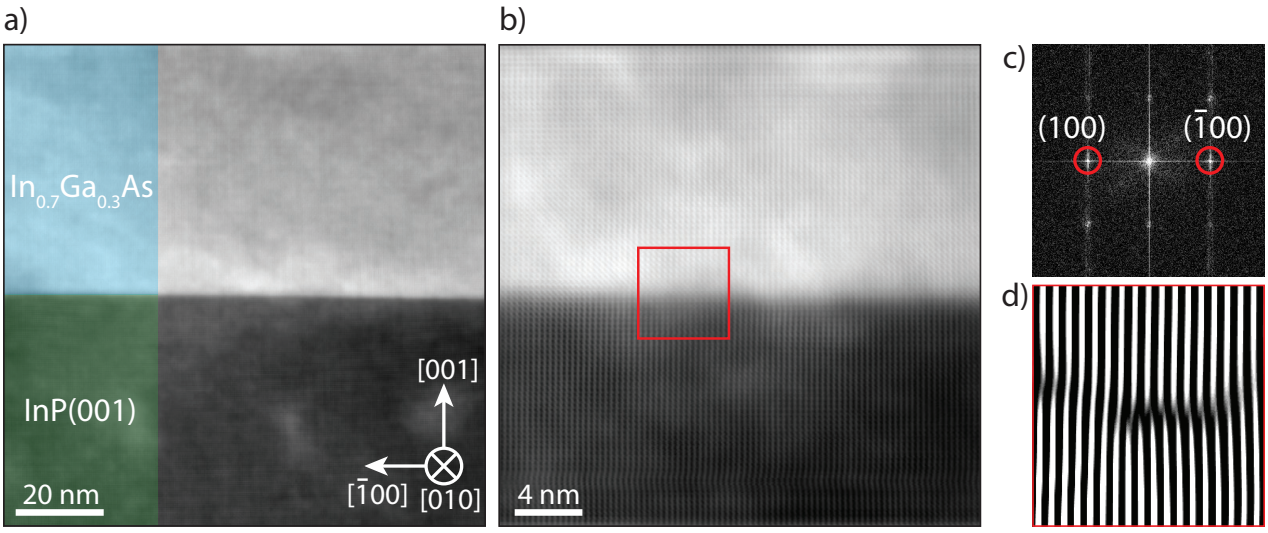

Figure 5.5.: Misfit dislocation generation at mismatched crystal interfaces. a) HAADF-STEM image of an $In_{0.7}Ga_{0.3}As$ - InAs epitaxial interface, belonging to a NW. b) Magnified atomic resolution image of the interface. c) FFT of b) and the selected Bragg peaks used to highlight the (100) planes. d) IFFT of the red square in b), selecting the Bragg peaks in b) and highlighting the misfit dislocation at the interface.

Figure 5.5a shows a cross-sectional HAAD-STEM image of an $In_{0.7}Ga_{0.3}As$ single buffer layer grown on InP(001), along the [010] zones axis. The lattice mismatch at the interface is 1.1%, calculating the lattice parameter for $In_{0.7}Ga_{0.3}As$ using Vegaard's law [153]. Figure 5.5b is a high magnification

atomic resolution image of the mismatched interface. The FFT is calculated on the red square and the $\{100\}$ peaks are masked to performed inverse FFT (IFFT) in order to observe those isolated planes, as shown in Figure 5.5c. Figure 5.5d highlights the presence of a misfit dislocation on the interface. This dislocation appears in the interface along the zone axis direction, however due to the invisibility criterion [154] dislocations along other directions are not visible, but expected to exist [140].

Misfit dislocations also appear in two buffer layer samples. Figure 5.6a is a cross-sectional atomic resolution HAADF-STEM image of the already mentioned GaAs(001) substrate - GaAs(Sb) - $In_{0.7}Ga_{0.3}As$ - InAs structure along the $[1\bar{1}0]$ zone axis. The frame corresponds to the area marked with the blue square in the inset sketch. The FFT is performed to the image followed by selection of the $(\bar{1}\bar{1}1)$ and $(\bar{1}\bar{1}\bar{1})$ peaks for IFFT, as marked in the inset of figure 5.6b. The result highlights the stacking fault originated at the GaAs(Sb) - $In_{0.7}Ga_{0.3}As$ 5% lattice mismatch interface.

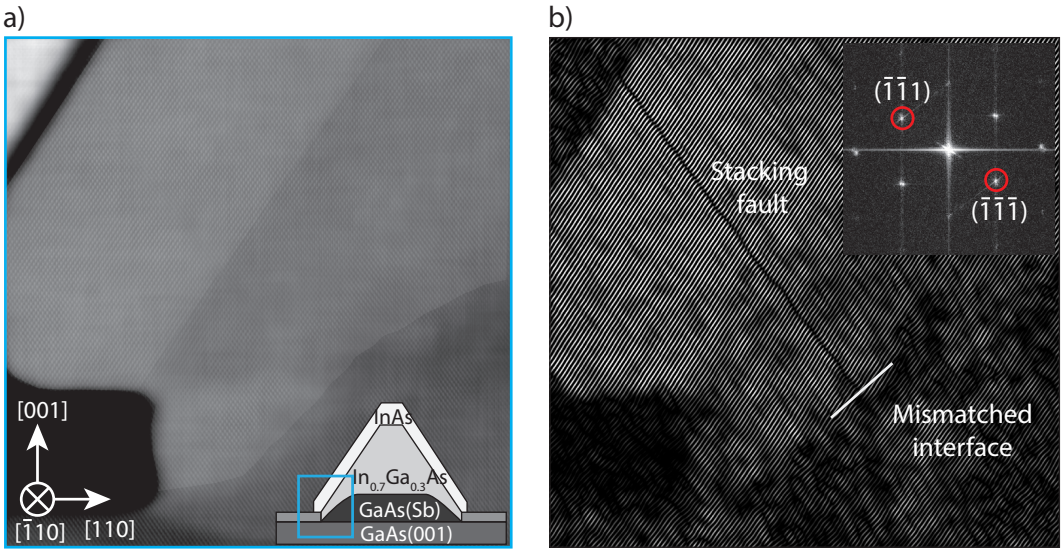

Figure 5.6.: Misfit dislocation triggering the creation of a stacking fault. a) HAADF-STEM image of a NW with a layer composition described in the inset sketch. The frame corresponds to the place described with the blue square in the sketch and the layers contrast has been enhanced. b) IFFT image of $(\bar{1}\bar{1}1)$ planes of image a), to highlight the stacking fault originating from a misfit dislocation at the mismatched interfaced between GaAs(Sb) and $In_{0.7}Ga_{0.3}As$. Frame widths are 40 nm.

Opposed to the case described in figure 5.5, the misfit dislocations generated at the curved mismatched interface of 5.6b have a probability of triggering

the creation of a stacking fault. This stacking fault penetrates inside the $In_{0.7}Ga_{0.3}As$ buffer layer and InAs transport channel to be annihilated at the NW surface. The fact that the line of the stacking fault atomic plane is not straight in figure 5.6b is explained by ambient vibration noise during the image acquisition.

It is known that the core of dislocations in III-V semiconductors have unpaired columns of atoms [155]. They have been characterized for SAG NWs in the past, where the formation of As rich and Ga rich core channels in stair-rod dislocations are measured by atomic resolution energy disperse X-ray TEM [156]. Since the crystal structure of the NWs presented in this thesis is the same as the previously referenced studies, it is assumed that the misfit dislocations characterized in figures 5.5 and 5.6 also create the same type of In and As rich cores. To understand the effects of these dislocations and their core channels on InAs, DFT calculations are performed. The crystal unit cell used in the calculation is an InAs crystal with a set of stair-rod dislocations (labeled with the numbers 1 and 2) connected by stacking faults (highlighted in yellow), as shown in figure 5.7. Although this crystal unit cell is not identical to the misfit dislocation generating a stacking fault (experimentally observed in figure 5.6), both structures contain comparable defects. The reason for choosing the crystal unit from figure 5.7 for the DFT calculation is the use of a single composition crystal. This approximation greatly reduces the complexity of the simulation, by eliminating the strain generated by mismatched materials and the different chemical potentials between layers involved. The details of this DFT calculation are in the appendix D.

Figures 5.8a and b show the band structure calculated by DFT for the InAs crystal described in figure 5.7 and for a clean InAs crystal, respectively. The horizontal axis describes the path along which the band structure is calculated and the vertical axis is the energy of the state in eV, normalized to the valence band maximum energy. The biggest difference between both cases is the penetration of two pairs of states into the band gap of the semiconductor with dislocation cores. This would have a destructive impact on the local semiconductor properties around the these defects. Also, compared to the clean case the folded valence and conduction bands are more finely split due to the influence of the dislocation cores. These consequences are to be expected due to the strain induced in the crystal, both from the dislocation cores and

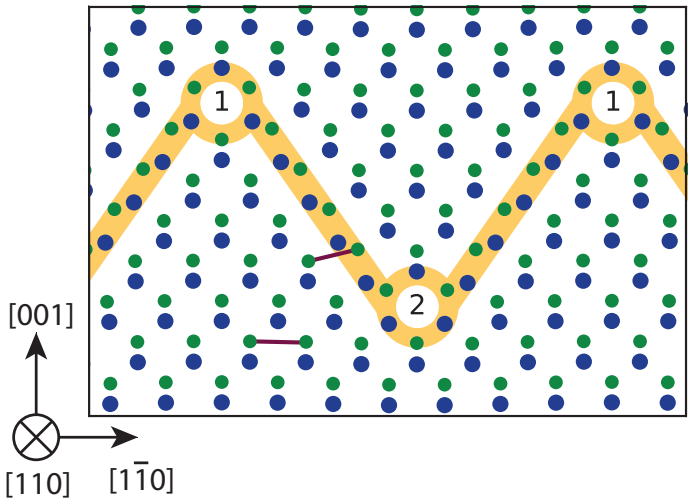

Figure 5.7.: Crystal structure of dislocation cores (1 and 2), joined by stacking faults (yellow). The green atoms correspond to As and blue to In. Dislocation types 1 and 2 are As rich (green atoms) and In rich (blue atoms), respectively. The purple line shows the typical As-As distance in a clean part of the crystal and through the stacking fault.

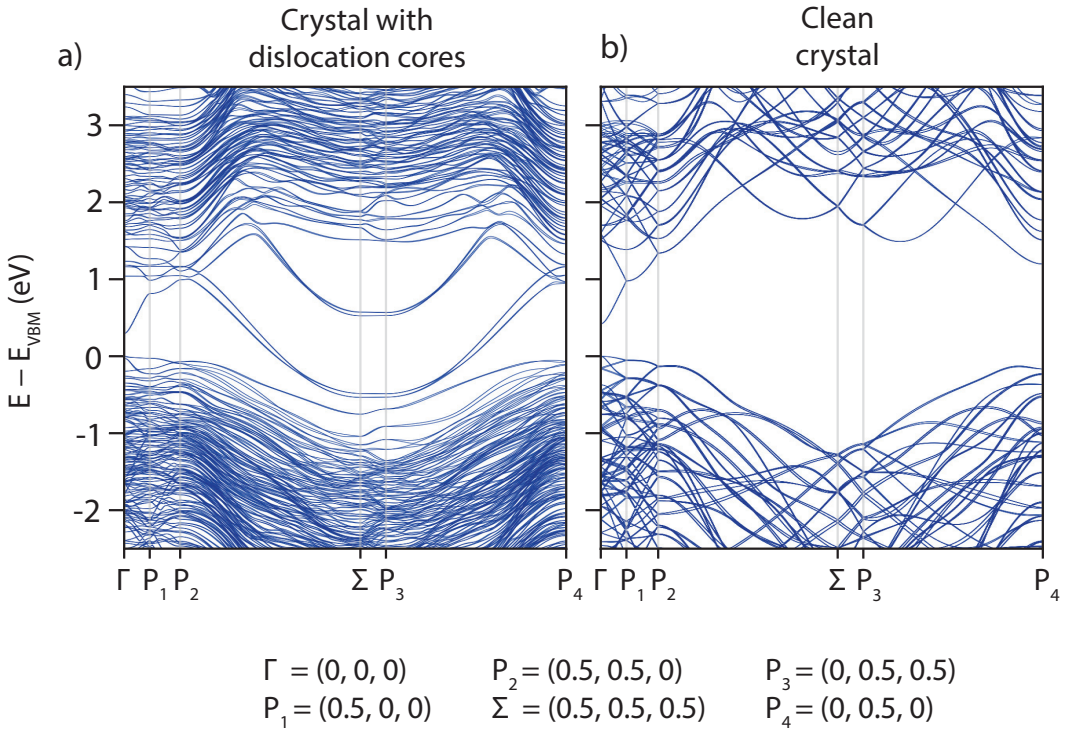

Figure 5.8.: a) Band structure of a crystal unit containing the dislocation cores described in Figure 5.7, along the path detailed in the x axis. Two pairs of states cross the band gap. b) Band structure of the same crystal without dislocations cores, where no states cross the band gap as expected.

the stacking faults across crystal unit, and the different charge accumulation accumulation around the As and In rich cores [156].

It is assumed that the results obtained in figure 5.8 can be extrapolated to the misfit dislocation generating a stacking fault observed in figure 5.6, due to the similarity of both structures. These defects would have a detrimental impact on the semiconductor performance, stressing the importance of developing cleaner material interfaces with reduced defects.

5.4 Electron Channeling Contrast Imaging

As discussed in the previous sections, stacking faults and dislocation cores generated during crystal growth are undesired and can have a catastrophic impact on the semiconductor device performance. For this reason, it is essential to perform structural characterization studies that can detect these defects. TEM is a powerful technique that can characterize the structure of a crystal down to the single atom level, as shown for example in figures 5.1, 5.5 and 5.6. However, it has some limitations: it requires a considerable amount of time for sample preparation by FIB cross-section, it is time consuming to conduct the experiment itself and it is unable of detecting defects perpendicular to the zone axis of the lamella [154]. This implies that in order to fully characterize the crystal structure of a NW and determine the presence of stacking faults and dislocations it is necessary to perform a transversal and longitudinal FIB lamellae.

SEM offers a set of advantages that go beyond the usual surface topography characterization and are complementary to the TEM observations. Electron channeling contrast technique (ECCI) is an SEM observation technique developed decades ago [157, 158] for characterization and visualization of crystal defects placed up to few μm inside ceramics and metals. Recently, it is attracting more interest due to its application in the field of semiconductors [159–161]. It allows to observe and quantify semiconductor crystal defects and strain in SEM, being is a fast and scalable way to study the quality of semiconductors.

5.4.1 Standard ECCI

The beam of electrons used to construct images in SEM can generate two types of electrons after hitting the sample: secondary electrons (SE) and backscatter electrons (BSE) [162]. SEs are created by inelastic scattering events between the primary beam and the atoms forming the crystal. These collisions eject tenths of electrons from the valence band of the sample for each primary electron, with energies between $\sim 1-20$ eV depending on the initial energy of the primary beam. The small energy of the generated SE make SEM imaging very surface sensitive, since the escape depth of is very small < 10 nm [163]. SEs generated below the first 10 nm sample depth can not escape and be detected, being reabsorbed by the sample. BSEs are electrons from the primary beam that after entering the specimen perform several elastic collisions with the sample until they can exit again through the surface. Their energy is comparable to the initial beam energy acceleration ~ 20 keV, so they can penetrate a distance of ~ 5 μm into the sample. Along their trajectory to leave the sample, BSEs generate additional SEs (defined as SE2s) that can leave the sample if they are not deeper than the escape depth. Primary electrons that scatter elastically in the sample without escaping from the surface loose all their energy and are absorbed.

ECCI observation mode is achieved in SEM when a crystalline sample is positioned at a tilt (T) and rotation (R) coordinates that favours the penetration of the high energy primary electrons. This is called channeling condition and it is caused by a reduction of scattering events of the primary electrons with the crystal lattice [164]. A BSE image acquired at channeling condition has a lower signal compared to an image not in channeling condition. At given T and R where the bulk crystal satisfy channeling condition, a disturbance on the crystal lattice such as defect or a strained region would not satisfy locally the channeling, causing an increase of the BSEs generated. Using a BSE detector to measure such effect would measure a standard ECCI image highlighting such defects.

Figure 5.9 shows a sketch of the geometry used in standard ECCI SEM. The objective magnetic lens (1) is created inside the objective lens pole piece (2), in a so-called closed objective lens geometry [165]. By "standard" it is referred to the ECCI performed with an objective lens of the closed type, thus not leaking

magnetic field to the sample. All the ECCI experiments reported previously use this geometry [166–168]. At certain R and T coordinates the crystalline sample (3) fulfills channeling condition, allowing a high transmission of primary electrons (4) and generating BSEs (5) mostly from strained regions of the crystal and defect that do not fulfill channeling. These BSEs are detected by a retractable solid state BSE detector placed on top of the sample (6).

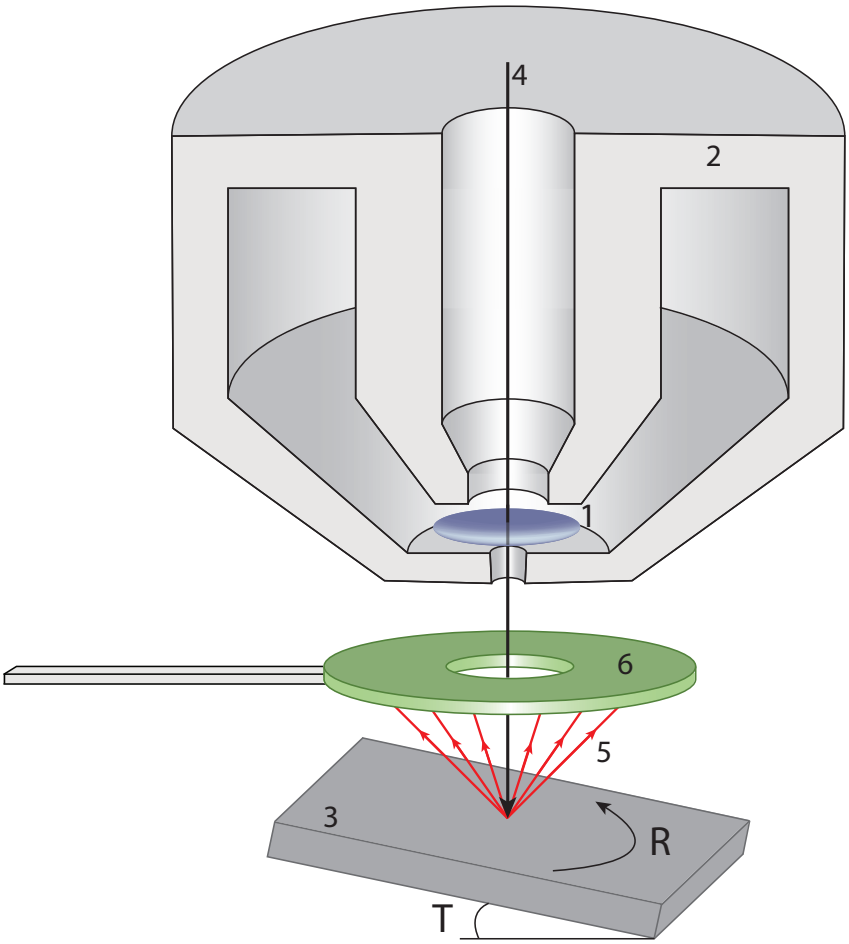

Figure 5.9.: Sketch of the geometry used in standard ECCI. (1) Magnetic objective lens confined inside the lens bore. (4) Primary electron beam. (2) Pole piece of the objective lens. (3) Sample placed at a given rotation R and tilt T. (4) High acceleration ($\sim$ 20 kV) primary electron beam. (5) Cone of generated high energy BSE. (6) Retractable solid state BSE detector placed on top of the sample.

A typical result of standard ECCI for InAs NWs of different widths grown on InP(111)B is shown in figure 5.10. Figures a and c are SE SEM images of the structures under study and b and d are their standard ECCI equivalents, respectively. In b, the elongated high contrast features are stacking faults of {111} planes and the dot like are dislocation cores generated at the mismatched

interface and emerging to the surface. The NW has gray constant contrast and the substrate totally black due to the channeling of the primary electrons at the used R and T. Figure 5.10 d is a standard ECCI image of a NW, where a stacking fault is highlighted. To be able to detect the faint contrast of the defects, detector contrast has to be increased up to the point where the substrate appears completely dark compared to the NW.

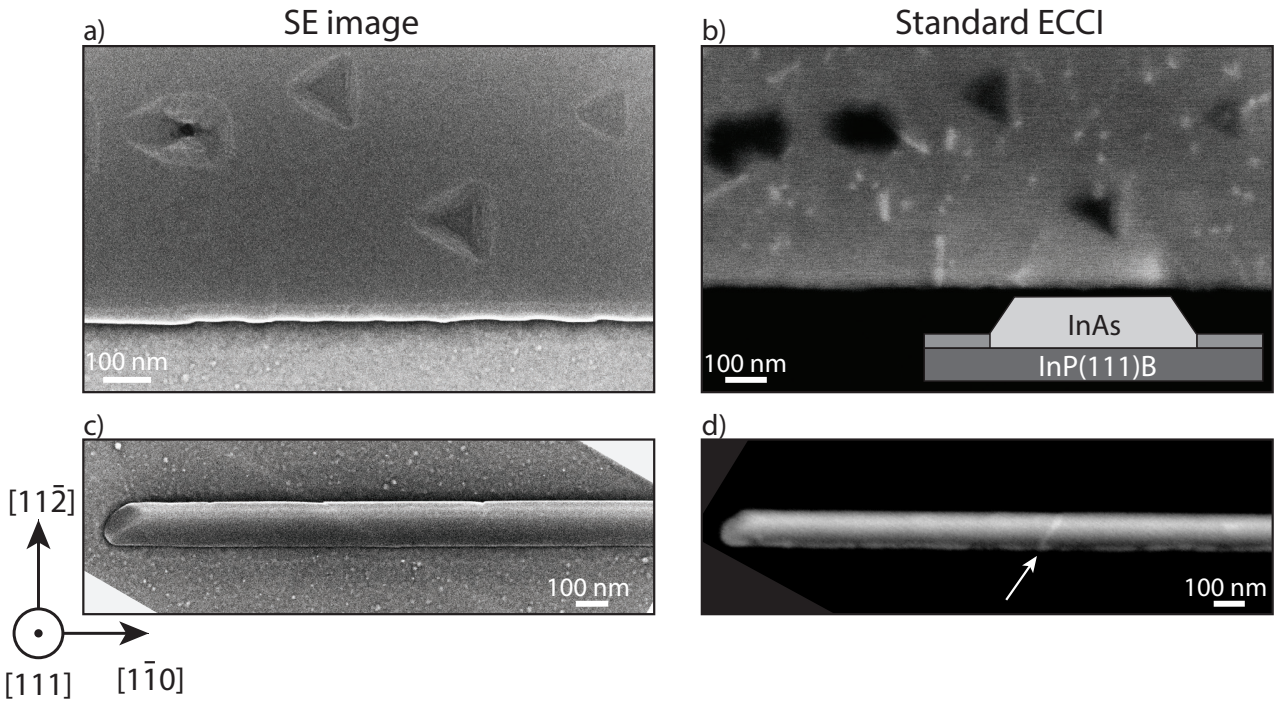

Figure 5.10.: Standard ECCI images of InAs NWs grown on InP(111)B. a) SE SEM image of a big mask opening. Crystal growth inhomogeneities are observed with the characteristic $\{111\}$ triangular shapes. b) Standard ECCI image of the same region than a), highlighting the crystal defects. The elongated bright features correspond to stacking faults being generated at the mismatched interface and propagating to the surface and the bright dots are misfit dislocation as well propagating to the surface. c) SE SEM image of a NW along $[1\bar{1}0]$. d) Standard ECCI image of the same NW than c), highlighting a bright stacking fault.

To be able to probe defects at certain depth inside the structures, an acceleration voltage of 20 kV is used in the experiments to achieve a high electron penetration. The escape depth of BSE on InAs at this voltage is ~ 1 µm [162], so the ECCI images probe the whole volume of the InAs NWs. Due to the small yield of BSE creation, the acquisition time of the images is 40 s, several times higher than for SE image. The tilt coordinate is an inherent limitation of the standard ECCI setup shown in figure 5.9. Due to the placement of

the retractable BSE detector on top of the sample the stage cannot tilt more than 5° without risking a dangerous collision between sample and detector. Although the working distance can be increased to gain a higher T range, this will reduce the BSE detected signal making the process even less efficient. Further requirements to achieve standard ECCI are advanced SEM characteristics such as low probe divergence and high electron brilliance, which are met in the Thermofisher Verios G4 SEM used for these experiments [169, 170].

Particular crystal defects arise at specific channeling conditions, making it important to know which conditions gives certain defects. Electron Channeling Patterns (ECP) are electron back scatter diffraction (EBSD)-like micrographs that show the crystal structure of a given sample. A change in the Bragg condition caused by a variation in the angle between the primary beam and crystal lattice generate increase or decrease in the BSE intensity [164]. By doing a lowest magnification 2D electron probe raster over the sample, a pattern of high contrast bands can be imaged with the BSE detector. This is caused by the change in the incident angle of the electron probe with respect to the crystalline substrate while scanning, fulfilling Bragg's diffraction condition for some of the angles. This ECP describes the sets of the crystallographic planes perpendicular to the surface. The experimental configuration to generate ECPs is the same as the one from figure 5.9 and the details of the imaging conditions are specified in appendix C.

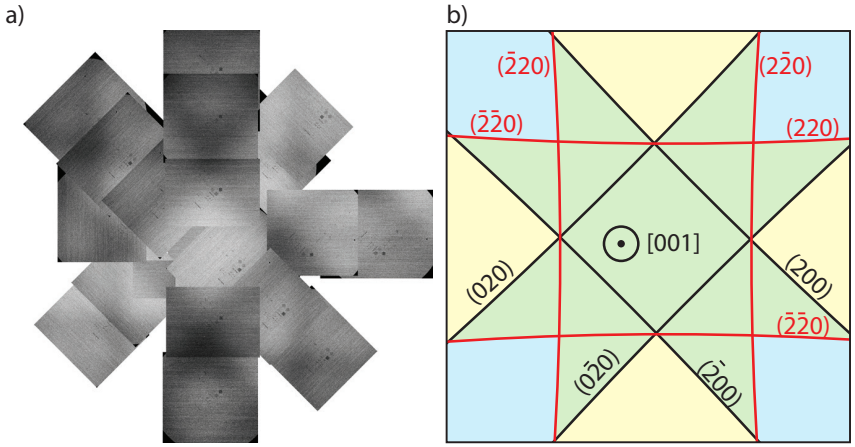

Figure 5.11.: a) Electron Channeling Pattern acquired with the BSE detector in the Thermofisher's Elstar electron column. The angular resolution of each ECP image obtained is very small, making it necessary to stitch the images at different T and R into a collage. The bright areas correspond to Kikuchi bands, similar to an EBSD-like micrograph. b) Sketch of the ECP measured in a), with the observed bands labeled.

Figure 5.11a shows a collage of the lowest possible magnification BSE images taken on a GaAs(001) substrate. The reason to stitch the images into a recognisable image is because of the small angular tilt of the probe while scanning large areas. For this reason, each of the images correspond to a different T and R values of the sample. Although this small probe tilt is a feature usually considered as a good property of a SEM electron column, in this case it reduces the field of view of ECP images. A simulation of the band diagram for GaAs(001) substrates is in figure 5.11b with labels, for comparison with the experimental one. The diagram was computed using the freeware Kossel/Kikuchi from the JCrystalSoft suite [171, 172].

At the positions in the ECP where two bands cross, the Bragg condition is fulfilled for two sets of plane at the same time, making them zones of high electron channeling and darker in contrast. The standard ECCI images taken in figure 5.10 b and d where acquired at the corner where the $(2\bar{2}2)$ and $(\bar{2}22)$ meet. This makes it a place where defects have a high chance to be observed with high contrast since the non diffracted electrons channel inside the sample until complete absorption.

5.4.2 Immersion ECCI

The standard ECCI procedure presented before is a very useful defect characterization tool that allows to detect stacking faults and dislocations in NWs without the necessity of performing TEM cross-section lamellae, as shown in figure 5.10. However, it also has some drawbacks to take into consideration. The very slow frame acquisition time (~ 1 min), the small inherent spatial resolution arising from BSE imaging, the need of a solid state detector and the sample tilt limitation hampers the utility of this technique. For these reasons, in this section it is developed a new ECCI imaging mode that allows to get the benefits of ECCI itself together with the high spatial resolution of SE imaging.

High-end modern SEMs incorporate a technology called immersion mode developed in the decade of the 90's by the company Hitachi [173]. After the expiration of the patent in 2012, other microscopy companies like Thermofisher implemented this technology in their flagship SEMs. This technology uses a type of objective lens called open, snorkel or magnetic immersion lens [174].

The pole piece of the immersion lens is modified compared to the standard lens presented in figure 5.9, in a way that the magnetic lens is generated outside the pole piece and bore the lens. The structure of the objective lens pole piece and the generated immersion lens is described in figure 5.12, (2) and (3) respectively.

The magnetic lens immerses the sample inside its own magnetic field, giving its name to the immersion observation mode. Among all the advantages of this lens geometry, an important one is the reduction of the effective working distance between the lens and the sample virtually to 0, reducing the primary beam aberration coefficients and achieving the ultimate spatial resolution of an SEM [175, 176]. However, due to the high magnetic field generated of ~ 0.1 T ferromagnetic samples are not suitable to be observed in this mode.

In immersion mode, low energy SEs generated in the sample by the primary beam are affected by the lens strong magnetic field. They are bent to a spiral trajectory and redirected back into the electron column through the lens bore [177]. The suction tube is a conical device placed at the end of the electron column that can apply a bias voltage, device (6) in the sketch of figure 5.12. Its main function is to accept or reject the entrance to the column of the SEs, similar to an electron energy filter [178]. By setting the suction tube to a positive voltage, it attracts the SE towards the inside of the objective lens pole piece, for then being attracted and detected by the scintillator of the through the lens detector (TLD) placed transversely inside the objective lens (10). This high efficient SE collection mechanism, together with the aberration reduction, makes the immersion mode an ultra high definition and low noise surface characterization technique.

In principle, the generated BSE would not be able to be detected by the TLD due to its location on the side of the lens. However, since the main function of the strong immersion magnetic field is to focus the high energy electrons of the primary beam to create a probe, it is also strong enough to bend the trajectory of the emerging BSE because both types of electrons have a comparable energy (~ 20 keV). This fact opens a possibility of detecting BSEs with the TLD in immersion mode and hence to observe crystal defects through an ECCI observation mode different than the standard.

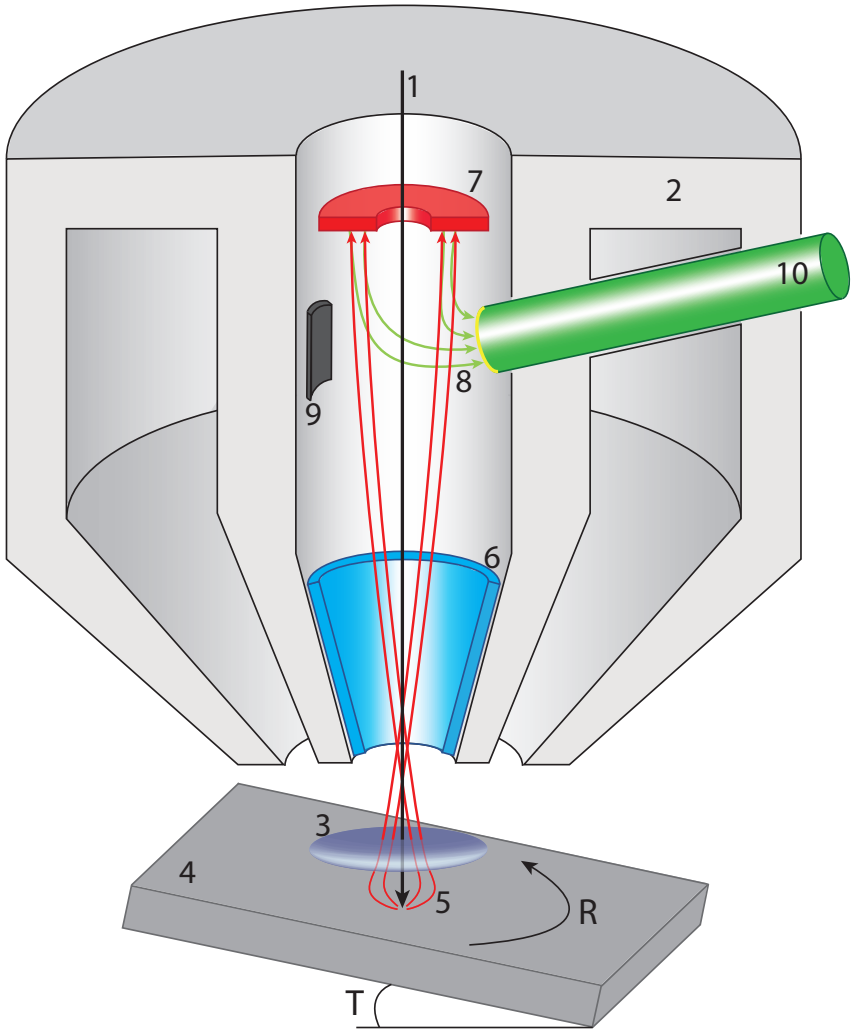

Figure 5.12.: Sketch of the geometry used in Immersion ECCI performed in Thermofisher's Elstar electron column. (1) High acceleration ($\sim$ 20 kV) primary electron beam. (2) Pole piece of the magnetic lens with an opened geometry at its lower part. (3) Magnetic objective lens, generated outside the lens pole piece. (4) Sample at specific T and R. (5) Generated BSE. (6) Suction tube. (7) Mirror detector acting as a BSE-SE convertion plate. (8) Generated SE. (9) Push electrode for SEs. (10) TLD detector, with a scintillator at 10 kV voltage.

Figure 5.12 shows a sketch of the geometry used during immersion ECCI. The primary beam (1) is conditioned by the upper lenses in the electron column and focused by the objective lens (2). The design of the immersion lens is different to the standard objective lens shown in figure 5.9, with a pole piece structure open at the bottom. This allows to leak the magnetic field generated by the wire coiling inside pole piece and to generate a magnetic lens (3) outside the lens pole piece. The design geometry of the SEM immersion lenses is identical in concept to the upper half of the objective lenses used in

TEMs, where the sample is introduced inside the pole piece of a magnetic lens [179]. At specific T and R sample coordinates that promote channeling, the primary beam generates a high yield of diffracted BSEs (5) created by stacking faults, dislocations and strained parts. These BSEs together with the surface SEs, are deflected by the immersion lens back into the electron column. This deflection of BSEs is the key factor that allows the immersion ECCI imaging mode. Once the BCEs are in the column they hit the mirror detector (7), which for this purpose it solely acts as a BSE to SE converter plate [178]. The newly generated SEs (8) are called SE3s and are repelled by the push electrode (9) towards the TLD detector (10).

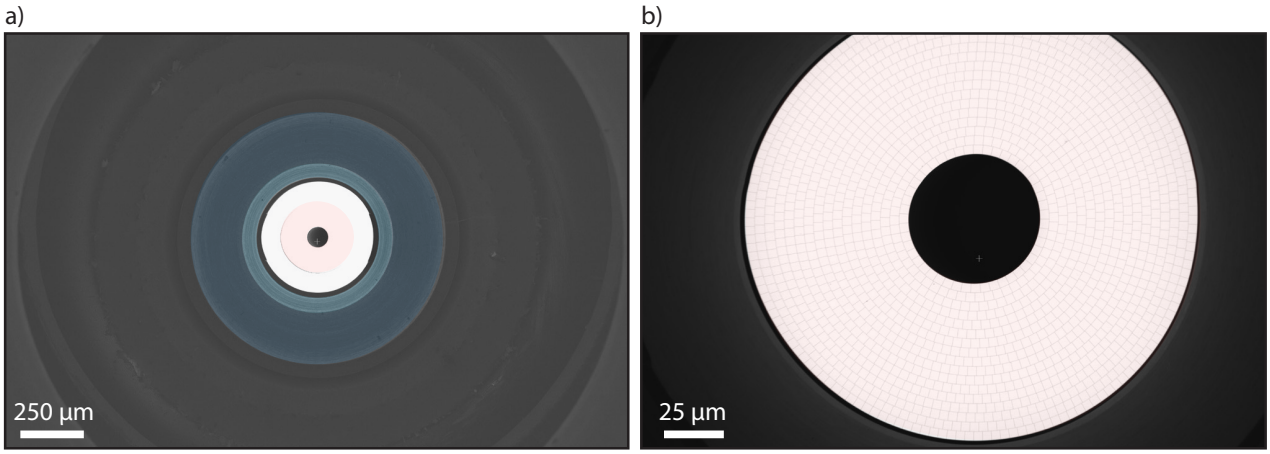

Figure 5.13.: SEM self image of the Thermofisher's Elstar column. a) View of the electron column from the sample's perspective. The blue colored region corresponds to the suction tube and the red region the mirror detector, as described in figure 5.12. b) High magnification self image of the mirror detector.

Figure 5.13 shows a self image of the electron column, acquired by mirror detector. A detector self image is achieved by setting the sample to a deceleration bias voltage higher than the incoming beam acceleration voltage. In figure 5.13a can be seen the suction tube highlighted in blue colors and the mirror detector that converts the BSE in SE3s in immersion ECCI. Although they seem to be concentric, they are at different heights in the electron column as detailed in the sketch figure 5.12. The higher magnification of the mirror detector in figure 5.13 shows the pixel tessellation covering the whole surface of the detector.

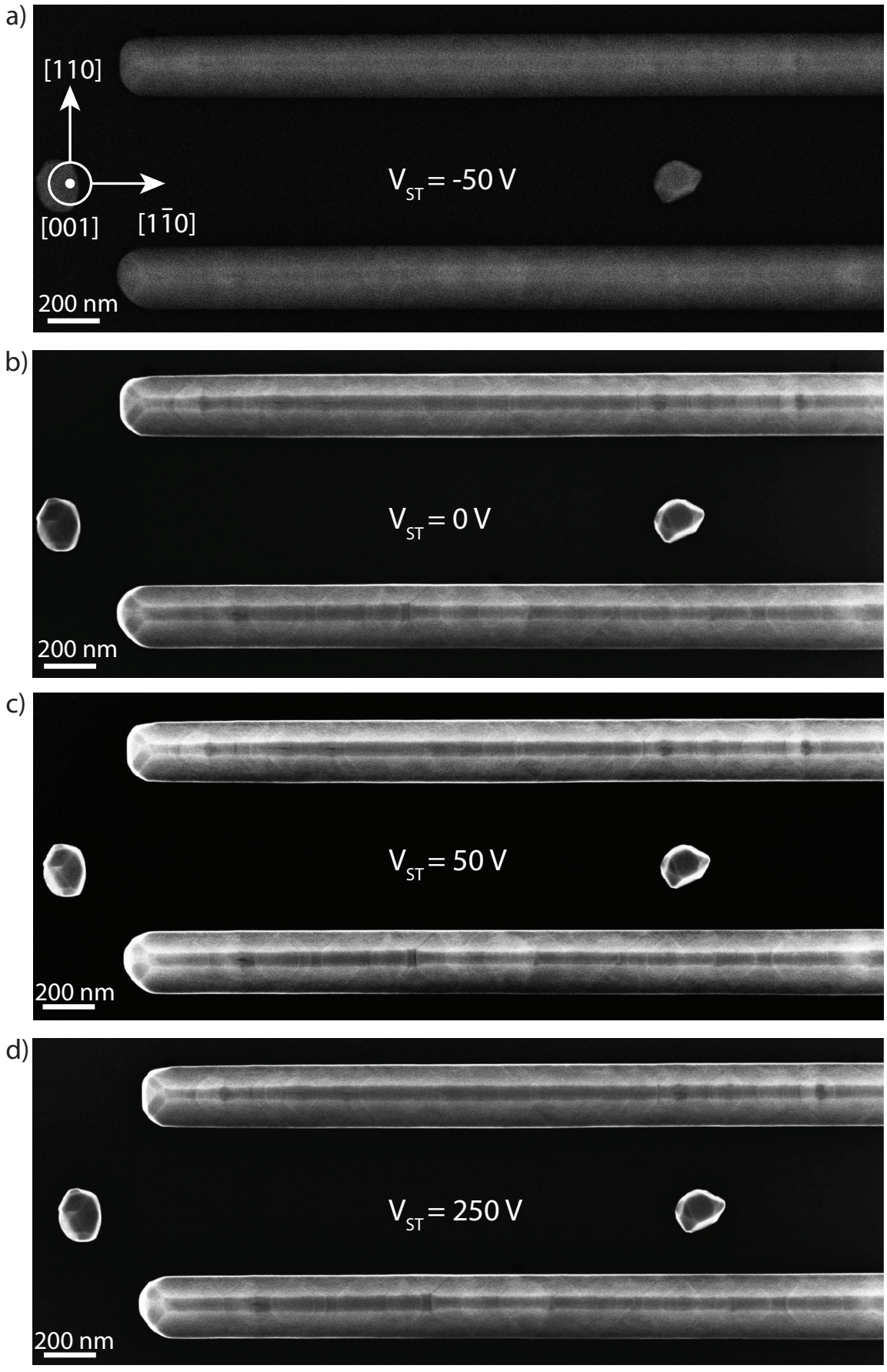
a)
[110]
[001]
[1$\bar{1}$0]
V_{ST} = -50 V
200 nm
b)
V_{ST} = 0 V
200 nm
c)
V_{ST} = 50 V
200 nm
d)
V_{ST} = 250 V
200 nm

Figure 5.14.: Comparision of different suction tube voltages on Immersion ECCI of stacking faults on GaAs(001) - GaAs(Sb) - $In_{0.7}Ga_{0.3}As$ - InAs NWs. a) $V_{ST} = -50$ eV. b) $V_{ST} = 0$ eV. c) $V_{ST} = 50$ eV. d) $V_{ST} = 250$ eV.

The signal acquired by the TLD in immersion ECCI is purely generated by SEs. Thanks to the BSE to SE3 conversion that occurs in the mirror detector, the TLD can observe a signal of SEs which is directly correlated with the BSEs deflected by crystal defects. Those by-product SE3s carry the original diffraction information from the BSEs that generated them, meaning that if the sample is at channeling condition it is possible to get diffraction contrast from defects that alter their local crystal lattice.

Figure 5.14 shows a set of four TLD immersion ECCI images of the same pair of GaAs(001) - GaAs(Sb) - $In_{0.7}Ga_{0.3}As$ - InAs NWs along $[1\bar{1}0]$. All the images were acquired at the same position of the ECP, located at the T and R coordinates where the three kikuchi lines $(0\bar{2}0)$, $(\bar{2}00)$ and $(\bar{2}\bar{2}0)$ meet. This point, as shown in figure 5.11a, has a strong channeling condition of the primary beam electrons due to its darker color compared to the rest of the regions. The images in figure 5.14 have a dark background contrast due to the high channeling and the need of increasing the relative contrast between NWs and substrate for observing the faint defect contrast.

The only parameter changed in the four images of figure 5.14 is the voltage of the suction tube from -50 to 250 V. Since the BSE are 3 orders of magnitude more energetic than the V_{ST}, they are not affected by it and can by-pass the effect of the suction tube being able to enter the column after being re-directed by the immersion lens magnetic field. Hence, the difference between the four images is the amount of SEs originated in the sample that are being detected. Figure a is the image for $V_{ST} = -50$ V, filtering out the low energy SEs from entering the column and being detected by the TLD. The contrast is very poor and the image is noisy, being consistent with a typical BSE image. Some faint contrast of $\{111\}$ stacking faults can be observed in the bottom NW, however the quality at these conditions is rather poor. Figures b, c and d allow the SEs generated in the sample to enter the column, with the 2 last images being directly attracted inside the column by the suction tube having a positive voltage. In these images, $\{111\}$ stacking faults are clearly visible in both NWs. The BSEs arising from the deep parts of the NWs with defect diffraction information are redirected by the immersion lens, converted

at the mirror detector and detected by the TLD. The fact that the images with an SE component (figures 5.14 b, c and d) have better defect contrast might imply that the SEs generated by the diffracted BSE during their way out of the sample (SE2s) have a big contribution on the defect detection. The high resolution surface information is supplied by the SEs generated at the superficial levels of the sample, making the immersion ECCI observation mode defect and topography sensible at the same time.

Although SEM does not have resolution enough to resolve the atomic layer that forms these stacking faults and dislocations, it is capable of detecting the effect that they have in the surrounding lattice.

5.5 Conclusion

The effect of stacking faults on the electrical properties of InAs is studied performing DFT calculations. Electron transmission through a single stacking fault is reduced by 2% using crystal structures with different number of unit cells. Although it is not a remarkable detrimental effect for the device performance, it is expected that a consecutive piling of stacking faults will have an increasing impact on the transmission. DOS calculations show that stacking faults do not introduce electron states on the band gap, only creating a localized state on the conduction band which is not expected to considerably affect the semiconductor.

On the other hand, dislocations have a bigger impact on the semiconductor properties. DFT calculations are performed using a crystal model of stair-rod dislocation connected by stacking faults. The generation of incoherently bounded As and In-rich channels on the dislocation cores generate two pairs of electron states inside the band gap. This impact on the semiconductor properties is more harmful than the generated by stacking faults.

In order to quantify the density of defects appearing in SAG NWs, immersion ECCI observation mode is developed. Although the results are not as precise as the ones obtained via cross-sectional TEM, it allows for a non-destructive higher throughput of results on defect characterization. The effect on the

local lattice caused by stacking faults on $\{111\}$ planes is observed with high resolution in InAs - $In_{0.7}Ga_{0.3}As$ - GaAs(Sb) NWs on GaAs(001).

The following list describes the advantages that immersion ECCI offers compared to standard ECCI:

1. In the immersion ECCI geometry there is no BSE detector placed on top of the sample. This allows to tilt the sample over a much bigger range of angles without risking a collision between sample and detector and hence accessing to further regions in the ECPs. Compared to the $\sim 5°$ limit for standard ECCI, immersion ECCI allows for tilt values limited by the range of stage $\sim 70°$.
2. Highest spatial resolution in the images, since the TLD in immersion mode is used.
3. Fast acquisition times of ~ 10 s, as opposed to standard ECCI ~ 1 min.
4. No limitation for small working distances.
5. More automation possibilities with SEM softwares like Autoscript [180], since it is a safe observation mode for unsupervised work due to the absence of the retractable BSE detector on top of the sample.

6 Conclusion and Outlook

The results presented in this thesis show, from a structural characterization point of view, the feasibility of III-V SAG NWs as the host platform to develop the Karzig et al. [60] approach for building a topological superconducting scalable quantum computer.

The results obtained partially fulfill some of the strict requirements of this platform approach, such as the growth of identical NW arrays in terms of volume and facets. The experiments described in chapter 4 reveal the different SAG growth modes arising from the inhomogeneous flux of adatoms in the mask - NW boundary. The sign of this flux, $\Delta\Gamma_{a_m a_c}$, determines the growth mode of the sample. Source growth mode $\Delta\Gamma_{a_m a_c} < 0$ is measured on GaAs and GaAs(Sb) arrays of NWs grown on GaAs(001). Varying the pitch, width and crystallographic orientation has an impact on the NW incorporation depending on their placement inside the array. Sink growth mode is observed on InAs NW arrays grown on GaSb(001). The sink growth mode affects the faceting of NWs near the end compared to the middle part, due to a higher collection of adatoms from the mask. This complicates a homogeneous deposition of the superconductor on a NW side facet, essential requirement to generate the topological phase [44].

Two solutions are proposed and developed to tackle the different growth modes generating a differential incorporation of NWs in arrays. One is the fine tuning of the growth modes of buffer layers by combining the source mode exhibited by GaAs(Sb) and the sink mode of $In_{0.7}Ga_{0.3}As$. The result is a buffer layer stack with homogeneous height to grow the InAs on. However,

this approach is heavily affected by any change in the array geometry, making it a non-general solution. A more scalable solution that is proposed implies to increase the number of NWs on the array. This generates an adatom density saturation region for the inner NWs, effectively overriding the effect of any growth mode. This solution can be scaled to any NW geometry by placing NWs surrounding the structures of interest. A disadvantage of this approach is the growth of this nearby NW barrier that can not be used in electronic transport measurements due to their different incorporation.

Another implication of the SAG growth modes is the influence on the SAG selectivity window. An internal structure inside the selectivity window separating f and T_{sub} regions depending on the sign of $\Delta\Gamma_{a_m a_c}$ is hypothesized. Although this thesis shows experimental evidence of both sink and source growth modes, it will need to be proofed experimentally the existence of both modes for NWs of the same composition. This can be tested for example by growing GaAs(Sb) NWs, that have been extensively characterized as source mode in chapter 4, at lower T_{sub} and f than the ones presented in this thesis.

In the first part of chapter 5, DFT calculations were performed to understand the effect of stacking faults and dislocation cores to the semiconductor properties. Stacking faults had a small impact on the semiconductor properties by reducing a 2% the electron transmission through them. On the other hand, dislocation cores generate a pair of electron states in the band gap that would destroy the topological phase on the surroundings of the core. Luckily, the misfit dislocations shown in this thesis are buried under the buffer layers, maintaining its influence far from the transport channel. Overall, defects are a critical aspect on the growth of SAG NWs, possibly becoming a roadblock for SAG to host Karzig et al. approach of the quantum computer if they are not minimized [141, 143, 181].

The need of higher throughput characterization techniques led to the development of the SEM observation mode immersion ECCI. This technique, explained in the second half of chapter 5, demonstrates to be faster and providing higher resolution imaging than standard ECCI. Stacking faults are observed on InAs - $In_{0.7}Ga_{0.3}As$ - GaAs(Sb) on GaAs(001) due to their diffractive effect on their nearby crystal lattice, giving a higher yield of generated BSE. A faster acquisition time, without sample preparation and higher resolution technique allows to quantify defects in NWs and speed up their optimization.

Overall, the use of III-V SAG NWs as a scalable platform to host the topologically protected quantum computer is promising. However, more development needs to be done on the incorporation reproducibility of NW networks and general defect reduction.

A

Pre-growth mask fabrication

This appendix defines the recipe used for the preparation of the SAG SiO_2 mask before MBE growth.

SiO_2 mask deposition

- The wafers from the growths used in this thesis were Fe-doped InP(001) 2" 350 μm thick, undoped GaAs(001) 2" 350 μm thick and undoped GaSb(001) 2" 350 μm thick, all from WaferTech.
- Deposition of nominal 10 nm of SiO_2, recipe "Std HF SiO2 10s" at 300 °C. The PECVD setup used for the deposition is located in the Nanolab cleanroom from the Danish Technical University, model SPTS Multiplex.
- Final layer thickness is measured by ellipsometry.

EBL of the mask

- CSAR13 resist is spun over the wafer at 4000 RPM during 45 s.
- Bake resist 120 s at 185 °C
- Electron exposure is performed in an Elionix F125 125 kV acceleration voltage. Fine NW structures have an electron dose of 385 $\mu C/cm^2$ under 500 pA current.
- Rough alignment mark structures have an electron dose of 600 $\mu C/cm^2$ under a 2 nA current.
- Develop the exposed resist dipping the wafer in a solution of MIBK:IPA 1:3 during 30 s.
- Plasma ash during 2 min to make the resist walls vertical.

ICP-RIE Dry etch

First run this recipe on a dummy wafer with a thick SiO_2 deposition to calculate precisely the etch rate, before the processing of every wafer. The setup used was the III-V ICP-RIE placed in the Nanolab cleanroom at the Danish Technical University.

- Run a 10 min O_2 plasma clean of the chamber with the dummy wafer inside.
- Run a 1 min slow etch with CF4 and H2 in order to clean the chamber. Recipe "nbi/SiO2 slow".
- Introduce the wafers to be processed in the center of the chamber and run the recipe "nbi/SiO2 etch slow" for 16 s, if the mask SiO_2 thickness is 10 nm.
- Run a 20 min chamber cleaning recipe on a dummy wafer when leaving. Recipe "clean/chamber clean O_2".

Cleaning before MBE growth

- Dip wafer in acetone for 20 min.
- Sonicate 1 min at 30% power and 80 kHz frequency.
- Dip in IPA and sonicate with the same recipe as before.
- Dip in new IPA and sonicate with the same recipe as before.
- Dip in MQ and sonicate with the same recipe as before.
- Rinse in MQ and dry with the N_2 gun.

B

MBE SAG recipes

This appendix describes the MBE recipes used for the growth of the SAG samples explained in this thesis. The first list explains to which sample number does correspond each sample presented and the second list specifies the growth details of each of them. All temperatures shown are measured by pyrometer and the growth rates are calculated via RHEED oscillations of monolayer growth.

- Figure 4.2a-c corresponds to growths recipe #1 for GaAs(Sb) and recipe #2 for GaAs.
- Figure 4.3 corresponds to growth recipe #3
- Figure 4.4d is a series of samples with common growth recipe #1, grown at the different specified temperatures.
- Figure 4.5 corresponds to growth recipe #1. Unlike the other NWs presented in 4.2a, these NWs were grown at the edge of the substrate. This had an influence on the local T_{sub}, being slightly smaller than in the center and causing some incorporation on the mask.
- Figure 4.6 corresponds to growth recipe #2.
- Figure 4.7 corresponds to growth recipe #4.
- Figure 4.8a corresponds to growth recipe #5
- Figure 4.8b corresponds to growth recipe #6
- Figure 4.9a corresponds to growth recipe #7
- Figure 4.9b corresponds to growth recipe #8
- Figure 4.16a corresponds to growth recipe #9
- Figure 4.16b corresponds to growth recipe #10
- Figure 4.16c corresponds to growth recipe #11
- Figure 4.17c corresponds to growth recipe #4
- Figure 4.18 corresponds to growth recipe #12
- Figure 4.19 corresponds to growth recipe #13
- Figure 4.22 corresponds to growth recipe #14

1. GaAs(Sb): Growth T is 603 °C, As/Ga ratio 9, Sb/Ga ratio 3, Ga growth rate 0.1 ML/s, growth time 1800 s. SiO_2 mask (10 nm), grown on GaAs(001).
2. GaAs: Growth T is 597 °C, As/Ga ratio 9, Ga growth rate 0.1 ML/s, growth time 1800 s. SiO_2 mask (10 nm), grown on GaAs(001).
3. GaAs(Sb): Growth T is 573 °C, As/Ga ratio 9, Sb/Ga ratio 3, Ga growth rate 0.1 ML/s, growth time 1800 s. SiO_2 mask (10 nm), grown on GaAs(001).
4. InAs: Growth T is 516 °C, As/In ratio 6, In growth rate 0.056 ML/s, growth time 6000 s. SiO_2 mask (10 nm), grown on GaSb(001).
5. $In_{0.53}Ga_{0.47}As$: Growth T is 508 °C, In growth rate 0.023 ML/s, Ga growth rate 0.01 ML/s, growth time 7200 s.
6. GaAs(Sb)-InGaAs-InAs:
    a) Growth T of GaAs(Sb) is 602 °C, As/Ga ratio 10.1, Sb/Ga ratio 3, Ga growth rate 0.1 ML/s, growth time 1800 s.
    b) Growth T of InGaAs is 533 °C, As/Ga ratio 12, Ga growth rate 0.01, In growth rate 0.09 ML/s, growth time 3600 s.
    c) Growth T of InAs is 523 °C, As/In ratio 9, In growth rate 0.09 ML/s. AlOx (2nm) - SiOx (10nm) mask, grown on GaAs(001).
7. GaAs(Sb)-InGaAs-InAs:
    a) Growth T of GaAs(Sb) is 602 °C, As/Ga ratio 9, Sb/Ga ratio 3, Ga growth rate 0.1 ML/s, growth time 1800 s.
    b) Growth T of InGaAs is 532 °C, Ga growth rate 0.01, In growth rate 0.09 ML/s, growth time 3600 s.
    c) Growth T of InAs is 523 °C, In growth rate 0.09 ML/s, growth time 1200 s. SiOx (10nm) mask, grown on GaAs(001).
8. GaAs(Sb)-InGaAs-InAs:
    a) Growth T of GaAs(Sb) is 602 °C, As/Ga ratio 9, Sb/Ga ratio 3, Ga growth rate 0.1 ML/s, growth time 1800 s.
    b) Growth T of InGaAs is 533 °C, Ga growth rate 0.01, In growth rate 0.09 ML/s, growth time 3600 s.
    c) Growth T of InAs is 526 °C, In growth rate 0.1 ML/s, growth time 1200 s. SiOx (10nm) mask, grown on GaAs(001).
9. InGaAs-InAs:

a) Growth T of InGaAs is 520 °C, Ga growth rate 0.01, In growth rate 0.09, As/In ratio 9, ML/s, growth time 1800 s.

b) Growth T of InAs is 504 °C, In growth rate 0.09 ML/s, growth time 900 s. SiOx (10nm) mask, grown on InP(001).

10. InGaAs-InAs:

    a) Growth T of InGaAs is 520 °C, Ga growth rate 0.01, In growth rate 0.09, As/In ratio 12, ML/s, growth time 1800 s.

    b) Growth T of InAs is 504 °C, In growth rate 0.09 ML/s, growth time 900 s. SiOx (10nm) mask, grown on InP(001).

11. GaAs(Sb)-InGaAs-InAs:

    a) Growth T of GaAs(Sb) is 601 °C, As/Ga ratio 9, Sb/Ga ratio 3, Ga growth rate 0.1 ML/s, growth time 1800 s.

    b) Growth T of InGaAs is 528 °C, Ga growth rate 0.01, In growth rate 0.09 ML/s, growth time 1800 s.

    c) Growth T of InAs is 526 °C, In growth rate 0.1 ML/s, growth time 900 s. SiOx (10nm) mask, grown on GaAs(001).

12. GaAs(Sb): Growth T is 573 °C, As/Ga ratio 9, Sb/Ga ratio 3, growth time 1800 s, growth rate 0.1 ML/s. SiO_2 mask (10 nm), grown on GaAs(001).
13. GaAs(Sb): Growth T is 537 °C, As/Ga ratio 9, Sb/Ga ratio 3, growth time 8700 s, growth rate 0.02 ML/s. SiO_2 mask (10 nm), grown on GaAs(001).
14. GaAs(Sb)-InAs. GaAs(Sb): Growth T is 585 °C, growth time 7200 s, growth rate 0.05 ML/s InAs: Growth T is 426 °C, growth time 630 s, growth rate 0.02 ML/s. SiO_2 mask (10 nm), grown on GaAs(001).

C

FIB and ECCI microscope conditions

This appendix details the imaging conditions used during the cross sectional lamella preparation by FIB and the immersion ECCI defect characterization.

FIB conditions

- Electron deposition of Pt for protection: stage at 0° tilt, 2kV, 5.5 nA current over an area of 3x3 μm and 2 μm in height
- Ion beam Pt deposition for additional protection: stage at 53° tilt, 30 kV and 90 pA current over an area of 10x3 μm and 2 μm in height.
- Etching of main trenches: 30kV at 9 nA current for a depth of 3 μm. In parallel mode.
- Polish away the redeposited material over the sample side of the trench, same conditions
- Etching of one side of the lamella for inserting the micromanipulator needle: 30 kV and 2.7 nA current for a depth of 3 μm.
- Perform a thin lamella undercut: stage tilt at 0° and 0.9 nA current.
- Insert the micromanipulator needle, approach until it gently touches the lamella and weld it with electron deposited Pt using the same recipe than before.
- Perform the final cut to the lamella and lower the stage for detachment.
- Bring the lamella to the TEM Cu grid and weld it with electron and ion deposited Pt, using the same recipes.
- Perform the final lamella polishing until it reaches a thickness < 100 nm, by under and overtilting the sample to reach the bottom part. The final steps are performed at low ion current: 2 kV and 24 pA.
- Ion imaging conditions: 30 kV at 2.7 pA current.
- SEM imaging conditions: 20 kV at 0.1 nA current.

ECCI conditions

Drive the stage to the desired R and T coordinates from the ECP that give a high defect contrast (key point). Immersion mode ON, TLD detector ON, downhole visibility mode, no beam deacceleration, 20 kV, 0.4 nA, working distance 4 mm. Increase the contrast the highest possible level, where the image starts to saturate. Imagining conditions are 3072x2048 pixels, suction tube to 70 V, Mirror detector -15 V and dwell time 3 μs.

D Simulation parameters

Coupled diffusion equations

These are the main lines of the coupled diffusion equations code used to model the incorporation of NWs in figures 4.12 and 4.6. The code was written by Tobias Særkjær and the following lines are the essential parts of it:

```
d = 20000;
w = 150;
p = 500;
x0 = 0;
x1 = (p-w)/2;
x2 = (p+w)/2;
x3 = (3*p-w)/2;
x4 = (3*p+w)/2;
x5 = d/2;
xresolution = 1;
xarray = linspace(0,d/2,1+(d/2)*xresolution);

global D_NW nu_NWav nu_NWas F_NW D_SiO nu_SiOav nu_SiOas F_SiO
F_beam = 100;
difflength_NW = 4000;
nu_NWav = 0;
nu_NWas = 30;
D_NW = difflength_NW^2;
beammulti_NW = 1;
F_NW = F_beam * beammulti_NW;
difflength_SiO = 5000;
nu_SiOav = 90;
nu_SiOas = 0;
D_SiO = difflength_SiO^2;
```

```
beammulti_SiO = 1;
F_SiO = F_beam * beammulti_SiO;
xmesh = sort(cat(2,xarray,[x1 x2 x3 x4]));
yinit = [1; 1];
sol = bvpinit(xmesh,yinit);
sol = bvp5c(@(x,y,r) f(x,y,r), @bc, sol);
```

The obtained solution sol contains the adatom density distribution along the NWs geometry defines in the beginning of the code. The solution is an structure array with x and y vectors that can be plotted in Matlab in the usual way.

Analytical model

The constants used to obtain a solution that replicates the data are listed below, in arbitrary units. For simplicity, constants like k_B are grouped together with the activation energies of the transitions δ_g. These adatom transitions are normalized to the supplied flux of adatoms f to the surface, set arbitrarily to 1. These constants replicate the case for source growth mode presented in figure 4.13, evaluated in the equation 4.7. Other set of parameters can probably be found with a more realistic physical dependence between each other.

```
delta_{hcv}    = 1.405e4
c_{Gamma_des}  = 1070e7
c_{acac}       = 5.8e-3
c_{acs}        = 1e-10
c_{acv}        = 5e13
delta_{g_acac} = 15e3
delta_{g_acs}  = 5.8e3
delta_{g_acv}  = 3.55e4
c_{amam}       = 7e-3
c_{ams}        = 2e-8
c_{amv}        = 2e11
delta_{g_amam} = 13.3e3
delta_{g_ams}  = 5.68e3
delta_{g_amv}  = 3.2e4
```

DFT calculations

The DFT calculations are computed in the Quantum ESPRESSO software using the aiida-quantumespresso platform and plug-ins aiida-wanier90 and aiida-optimize. The code was written by Dominik Gresch. To perform the simulation several considerations were taken:

- Use of projector augmented-wave pseudopotentials from the pslibrary.
- Use of kinetic energy cutoffs of ≥ 45 Ry for wave-functions and ≥ 280 Ry for potentials and densities.
- **k**-point grids are ≤ 0.25 Å^{-1}.
- The Kwant package is used for the transport calculations in figure 5.4
- Use of the DFT+U method that allows to correct for the incorrect prediction of the vanishing gap in for InAs [182].

Bibliography

[1] Lillian Hoddeson. „The discovery of the point-contact transistor“. In: *Historical Studies in the Physical Sciences* 12.1 (1981), pp. 41–76.

[2] Bardeen John and Walter H Brattain. *Three-electrode circuit element utilizing semiconductive materials*. US Patent 2,524,035. Oct. 1950.

[3] Kahng Dawon. *Electric field controlled semiconductor device*. US Patent 3,102,230. Aug. 1963.

[4] Martin M Atalla. *Semiconductor devices having dielectric coatings*. US Patent 3,206,670. Sept. 1965.

[5] Robert H Crawford. *Mosfet in circuit design: metal-oxide-semiconductor field-effect transistors for discrete and integrated-circuit technology*. McGraw-Hill Companies, 1967.

[6] Robert H Dennard *et al.* „Design of ion-implanted MOSFET's with very small physical dimensions“. In: *IEEE Journal of Solid-State Circuits* 9.5 (1974), pp. 256–268.

[7] Robert N Noyce. *Semiconductor device-and-lead structure*. US Patent 2,981,877. Apr. 1961.

[8] Gordon E Moore *et al. Cramming more components onto integrated circuits*. McGraw-Hill New York. 1965.

[9] Peter Van Zant. *Microchip Fabrication*. 5th ed. McGraw-Hill Professional, 2004. ISBN: 9780071432412.

[10] Victor V Zhirnov *et al.* „Limits to binary logic switch scaling-a gedanken model“. In: *Proceedings of the IEEE* 91.11 (2003), pp. 1934–1939.

[11] RT Bate. „Quantum-mechanical limitations on device performance“. In: *VLSI Electronics Microstructure Science*. Vol. 5. Elsevier, 1982, pp. 359–386.

[12] Dmitri E Nikonov and Ian A Young. „Overview of beyond-CMOS devices and a uniform methodology for their benchmarking“. In: *Proceedings of the IEEE* 101.12 (2013), pp. 2498–2533.

[13] Mu-Chun Wang *et al.* „Channel Surface Integrity with 2.4nm High-k Gate Dielectric under DPN Treatment at Different Annealing Temperatures“. In: *2021 9th International Symposium on Next Generation Electronics (ISNE)*. 2021, pp. 1–4. DOI: 10.1109/ISNE48910.2021.9493656.

[14] IBM Source. *IBM unveils world's first 2 Nanometer chip technology, opening a new frontier for semiconductors*. May 2021. URL: https://newsroom.ibm.com/2021-05-06-IBM-Unveils-Worlds-First-2-Nanometer-Chip-Technology,-Opening-a-New-Frontier-for-Semiconductors.

[15] Eric Masanet *et al.* „Recalibrating global data center energy-use estimates“. In: *Science* 367.6481 (2020), pp. 984–986. DOI: 10.1126/science.aba3758.

[16] Azalia Mirhoseini *et al.* „A graph placement methodology for fast chip design“. In: *Nature* 594.7862 (2021), pp. 207–212.

[17] Peide Ye, Thomas Ernst, and Mukesh V Khare. „The last silicon transistor: nanosheet devices could be the final evolutionary step for Moore's Law“. In: *IEEE Spectrum* 56.8 (2019), pp. 30–35.

[18] Richard P Feynman. „Simulating physics with computers“. In: *Feynman and computation*. CRC Press, 2018, pp. 133–153.

[19] David Deutsch. „Quantum theory, the Church–Turing principle and the universal quantum computer“. In: *Proceedings of the Royal Society of London. A. Mathematical and Physical Sciences* 400.1818 (1985), pp. 97–117.

[20] Lieven MK Vandersypen *et al.* „Experimental realization of Shor's quantum factoring algorithm using nuclear magnetic resonance“. In: *Nature* 414.6866 (2001), pp. 883–887.

[21] Sam McArdle *et al.* „Quantum computational chemistry“. In: *Reviews of Modern Physics* 92.1 (2020), p. 015003.

[22] Isaac L Chuang, Neil Gershenfeld, and Mark Kubinec. „Experimental implementation of fast quantum searching“. In: *Physical review letters* 80.15 (1998), p. 3408.

[23] David P DiVincenzo. „The physical implementation of quantum computation“. In: *Fortschritte der Physik: Progress of Physics* 48.9-11 (2000), pp. 771–783.

[24] J Sherson *et al.* „Light qubit storage and retrieval using macroscopic atomic ensembles“. In: *Physical Review A* 74.1 (2006), p. 011802.

[25] Bruce E Kane. „A silicon-based nuclear spin quantum computer“. In: *nature* 393.6681 (1998), pp. 133–137.

[26] Ferdinand Kuemmeth *et al.* „Coupling of spin and orbital motion of electrons in carbon nanotubes“. In: *Nature* 452.7186 (2008), pp. 448–452.

[27] Rainer Blatt and David Wineland. „Entangled states of trapped atomic ions“. In: *Nature* 453.7198 (2008), pp. 1008–1015.

[28] Jonathan P Home *et al.* „Complete methods set for scalable ion trap quantum information processing“. In: *Science* 325.5945 (2009), pp. 1227–1230.

[29] JQ You and Franco Nori. „Superconducting circuits and quantum information“. In: *arXiv preprint quant-ph/0601121* (2006).

[30] Michel H Devoret and John M Martinis. „Implementing qubits with superconducting integrated circuits“. In: *Experimental aspects of quantum computing* (2005), pp. 163–203.

[31] Yuval Oreg, Gil Refael, and Felix Von Oppen. „Helical liquids and Majorana bound states in quantum wires“. In: *Physical review letters* 105.17 (2010), p. 177002.

[32] Stevan Nadj-Perge *et al.* „Observation of Majorana fermions in ferromagnetic atomic chains on a superconductor“. In: *Science* 346.6209 (2014), pp. 602–607.

[33] Frank Arute *et al.* „Quantum supremacy using a programmable superconducting processor“. In: *Nature* 574.7779 (2019), pp. 505–510.

[34] Source: IBM. *On "quantum supremacy"*. Aug. 2020. URL: https://www.ibm.com/blogs/research/2019/10/on-quantum-supremacy/.

[35] Erik Lucero *et al.* „High-fidelity gates in a single Josephson qubit“. In: *Physical review letters* 100.24 (2008), p. 247001.

[36] Emanuel Knill. „Quantum computing with realistically noisy devices“. In: *Nature* 434.7029 (2005), pp. 39–44.

[37] Eric R Anschuetz *et al.* „Variational quantum factoring“. In: *arXiv preprint arXiv:1808.08927* (2018).

[38] A Yu Kitaev. „Fault-tolerant quantum computation by anyons“. In: *Annals of Physics* 303.1 (2003), pp. 2–30.

[39] Tudor D Stanescu. *Introduction to topological quantum matter & quantum computation*. CRC Press, 2016, pp. 327–329.

[40] Bernard Field and Tapio Simula. „Introduction to topological quantum computation with non-Abelian anyons“. In: *Quantum Science and Technology* 3.4 (2018), p. 045004.

[41] Chetan Nayak *et al.* „Non-Abelian anyons and topological quantum computation“. In: *Reviews of Modern Physics* 80.3 (2008), p. 1083.

[42] Ettore Majorana. „Teoria simmetrica dell'elettrone e del positrone“. In: *Il Nuovo Cimento (1924-1942)* 14.4 (1937), pp. 171–184.

[43] Liang Fu and Charles L Kane. „Superconducting proximity effect and Majorana fermions at the surface of a topological insulator“. In: *Physical review letters* 100.9 (2008), p. 096407.

[44] Roman M Lutchyn, Jay D Sau, and S Das Sarma. „Majorana fermions and a topological phase transition in semiconductor-superconductor heterostructures“. In: *Physical review letters* 105.7 (2010), p. 077001.

[45] W Chang *et al.* „Hard gap in epitaxial semiconductor–superconductor nanowires“. In: *Nature nanotechnology* 10.3 (2015), pp. 232–236.

[46] P Krogstrup *et al.* „Epitaxy of semiconductor–superconductor nanowires“. In: *Nature materials* 14.4 (2015), pp. 400–406.

[47] Önder Gül *et al.* „Hard Superconducting Gap in InSb Nanowires“. In: *Nano Letters* 17.4 (2017), pp. 2690–2696.

[48] Sabbir A Khan *et al.* „Highly transparent gatable superconducting shadow junctions“. In: *ACS nano* 14.11 (2020), pp. 14605–14615.

[49] Martin Friedl *et al.* „Template-assisted scalable nanowire networks“. In: *Nano letters* 18.4 (2018), pp. 2666–2671.

[50] Roman M Lutchyn *et al.* „Majorana zero modes in superconductor-semiconductor heterostructures“. In: *Nature Reviews Materials* 3.5 (2018), pp. 52–68.

[51] Lucas Güniat, Philippe Caroff, and Anna Fontcuberta i Morral. „Vapor phase growth of semiconductor nanowires: key developments and open questions“. In: *Chemical reviews* 119.15 (2019), pp. 8958–8971.

[52] Thomas Kanne *et al.* „Epitaxial Pb on InAs nanowires for quantum devices“. In: *Nature Nanotechnology* (2021), pp. 1–6.

[53] Sasa Gazibegovic *et al.* „Epitaxy of advanced nanowire quantum devices“. In: *Nature* 548.7668 (2017), pp. 434–438.

[54] S Yokoyama *et al.* „Low-temperature selective growth of GaAs by alternately supplying molecular beam epitaxy“. In: *Journal of Crystal Growth* 95.1-4 (1989), pp. 32–34.

[55] A Okamoto and K Ohata. „Selective epitaxial growth of gallium arsenide by molecular beam epitaxy“. In: *Applied physics letters* 51.19 (1987), pp. 1512–1514.

[56] Filip Krizek *et al.* „Field effect enhancement in buffered quantum nanowire networks“. In: *Physical Review Materials* 2.9 (2018), p. 093401.

[57] Pavel Aseev *et al.* „Selectivity Map for Molecular Beam Epitaxy of Advanced III–V Quantum Nanowire Networks“. In: *Nano letters* 19.1 (2018), pp. 218–227.

[58] Asbjørn CC Drachmann *et al.* „Anodic oxidation of epitaxial superconductor-semiconductor hybrids“. In: *Physical Review Materials* 5.1 (2021), p. 013805.

[59] Fabrizio Nichele *et al.* „Scaling of Majorana zero-bias conductance peaks“. In: *Physical review letters* 119.13 (2017), p. 136803.

[60] Torsten Karzig *et al.* „Scalable designs for quasiparticle-poisoning-protected topological quantum computation with Majorana zero modes“. In: *Physical Review B* 95.23 (2017), p. 235305.

[61] Yu Liu *et al.* „Semiconductor–ferromagnetic insulator–superconductor nanowires: stray field and exchange field“. In: *Nano letters* 20.1 (2019), pp. 456–462.

[62] Mike G Astles. „Liquid-phase epitaxial growth of III-V compound semiconductor materials and their device applications“. In: *Crystal research and technology* 30.4 (1995).

[63] Crispin Hetherington *et al.* „In situ metal-organic chemical vapour deposition growth of III–V semiconductor nanowires in the Lund environmental transmission electron microscope“. In: *Semiconductor Science and Technology* 35.3 (2020), p. 034004.

[64] KY Cheng. „Development of molecular beam epitaxy technology for III–V compound semiconductor heterostructure devices“. In: *Journal of Vacuum Science & Technology A: Vacuum, Surfaces, and Films* 31.5 (2013), p. 050814.

[65] Karl W. Böer and Udo W. Pohl. „The Structure of Semiconductors“. In: *Semiconductor Physics*. Cham: Springer International Publishing, 2018, pp. 59–108. ISBN: 978-3-319-69150-3. DOI: 10.1007/978-3-319-69150-3_3.

[66] Koichi Momma and Fujio Izumi. „VESTA 3 for three-dimensional visualization of crystal, volumetric and morphology data“. In: *Journal of applied crystallography* 44.6 (2011), pp. 1272–1276.

[67] Patrick Ponath *et al.* „Preparation of a clean Ge (001) surface using oxygen plasma cleaning“. In: *Journal of Vacuum Science & Technology B, Nanotechnology and Microelectronics: Materials, Processing, Measurement, and Phenomena* 31.3 (2013), p. 031201.

[68] Udo W Pohl. *Epitaxy of semiconductors*. Springer, 2020.

[69] Yoshimi Horio, Yasuyuki Hashimoto, and Ayahiko Ichimiya. „A new type of RHEED apparatus equipped with an energy filter“. In: *Applied surface science* 100 (1996), pp. 292–296.

[70] BA Joyce. „Molecular beam epitaxy-fundamentals and current status“. In: *Contemporary Physics* 31.3 (1990), pp. 33–79.

[71] S Karthika, TK Radhakrishnan, and P Kalaichelvi. „A review of classical and nonclassical nucleation theories“. In: *Crystal Growth & Design* 16.11 (2016), pp. 6663–6681.

[72] XY Liu. „Heterogeneous nucleation or homogeneous nucleation?“ In: *The Journal of Chemical Physics* 112.22 (2000), pp. 9949–9955.

[73] FF Leal, SC Ferreira, and SO Ferreira. „Modelling of epitaxial film growth with an Ehrlich–Schwoebel barrier dependent on the step height“. In: *Journal of Physics: Condensed Matter* 23.29 (2011), p. 292201.

[74] RS Wagner and WC Ellis. „Vapor-liquid-solid mechanism of single crystal growth“. In: *Applied physics letters* 4.5 (1964), pp. 89–90.

[75] Frank Glas, Jean-Christophe Harmand, and Gilles Patriarche. „Why does wurtzite form in nanowires of III-V zinc blende semiconductors?“ In: *Physical review letters* 99.14 (2007), p. 146101.

[76] F Sebastian Bergeret *et al.* „Colloquium: Nonequilibrium effects in superconductors with a spin-splitting field“. In: *Reviews of Modern Physics* 90.4 (2018), p. 041001.

[77] Sabbir A Khan *et al.* „Multiterminal Quantized Conductance in InSb Nanocrosses“. In: *Advanced Materials* (2021), p. 2100078.

[78] L Desplanque *et al.* „In-plane InSb nanowires grown by selective area molecular beam epitaxy on semi-insulating substrate“. In: *Nanotechnology* 29.30 (2018), p. 305705.

[79] Akihiko Okamoto and Keiichi Ohata. „Selective epitaxial growth of InAs on GaAs by molecular beam epitaxy“. In: *Japanese journal of applied physics* 26.7A (1987), p. L1174.

[80] Daria V Beznasyuk *et al.* „The role of growth temperature on the electron mobility of InAs/$In_xGa_{1-x}As$ selective area grown nanowires“. In: *arXiv preprint arXiv:2103.15971* (2021).

[81] Pierre-Marie Coulon *et al.* „Selective area growth of Ga-polar GaN nanowire arrays by continuous-flow MOVPE: A systematic study on the effect of growth conditions on the array properties“. In: *physica status solidi (b)* 252.5 (2015), pp. 1096–1103.

[82] Katsumi Kishino, Hiroto Sekiguchi, and Akihiko Kikuchi. „Improved Ti-mask selective-area growth (SAG) by rf-plasma-assisted molecular beam epitaxy demonstrating extremely uniform GaN nanocolumn arrays“. In: *Journal of Crystal Growth* 311.7 (2009), pp. 2063–2068.

[83] Filip Krizek. „Semiconductor nanowire networks grown by Molecular Beam Epitaxy“. PhD thesis. PhD School of the Faculty of Science, University of Copenhagen, 2018.

[84] Krishna Seshan. *Handbook of Thin Film Deposition Techniques Principles, Methods, Equipment and Applications, Second Editon*. CRC Press, 2002.

[85] D Gräf *et al.* „Reaction of hydrofluoric acid and water with the GaAs (100) surface“. In: *Journal of Vacuum Science & Technology A: Vacuum, Surfaces, and Films* 8.3 (1990), pp. 1955–1960.

[86] S Verhaverbeke *et al.* „The etching mechanisms of SiO2 in hydrofluoric acid“. In: *Journal of the Electrochemical Society* 141.10 (1994), p. 2852.

[87] Keren J Kanarik, Samantha Tan, and Richard A Gottscho. „Atomic layer etching: rethinking the art of etch“. In: *The journal of physical chemistry letters* 9.16 (2018), pp. 4814–4821.

[88] Richard Wirth. „Focused Ion Beam (FIB) A novel technology for advanced application of micro-and nanoanalysis in geosciences and applied mineralogy“. In: *European Journal of Mineralogy* 16.6 (2004), pp. 863–876.

[89] OL Krivanek *et al.* „Towards sub-0.5 Å electron beams“. In: *Ultramicroscopy* 96.3-4 (2003), pp. 229–237.

[90] Johannes Schindelin *et al.* „Fiji: an open-source platform for biological-image analysis“. In: *Nature methods* 9.7 (2012), pp. 676–682.

[91] Mitsunori Kitta and Chie Fukada. „Scanning Spreading Resistance Microscopy: A Promising Tool for Probing the Reaction Interface of Li-Ion Battery Materials“. In: *Langmuir* 35.26 (2019), pp. 8726–8731.

[92] Xuezhi Ma *et al.* „Toward high-contrast atomic force microscopy-tip-enhanced Raman spectroscopy imaging: nanoantenna-mediated remote-excitation on sharp-tip silver nanowire probes“. In: *Nano letters* 19.1 (2018), pp. 100–107.

[93] Martin Espiñeira Cachaza *et al.* „Selective area growth rates of III-V nanowires“. In: *Physical Review Materials* 5.9 (2021), p. 094601.

[94] Tudor D Stanescu and Sumanta Tewari. „Majorana fermions in semiconductor nanowires: fundamentals, modeling, and experiment“. In: *Journal of Physics: Condensed Matter* 25.23 (2013), p. 233201.

[95] Stephan Plugge *et al.* „Majorana box qubits“. In: *New Journal of Physics* 19.1 (2017), p. 012001.

[96] Yoshiki Kato *et al.* „Selective growth of wurtzite GaN and AlxGa1- xN on GaN/sapphire substrates by metalorganic vapor phase epitaxy“. In: *Journal of crystal growth* 144.3-4 (1994), pp. 133–140.

[97] Muhammad Ali Johar *et al.* „Universal and scalable route to fabricate GaN nanowire-based LED on amorphous substrate by MOCVD“. In: *Applied Materials Today* 19 (2020), p. 100541.

[98] S Ambrosini *et al.* „Self-catalyzed GaAs nanowire growth on Si-treated GaAs (100) substrates“. In: *Journal of Applied Physics* 109.9 (2011), p. 094306.

[99] Martin Heiß *et al.* „Growth mechanisms and optical properties of GaAs-based semiconductor microstructures by selective area epitaxy“. In: *Journal of Crystal Growth* 310.6 (2008), pp. 1049–1056.

[100] L Desplanque *et al.* „Influence of nanoscale faceting on the tunneling properties of near broken gap InAs/AlGaSb heterojunctions grown by selective area epitaxy“. In: *Nanotechnology* 25.46 (2014), p. 465302.

[101] S Vaitiekėnas *et al.* „Selective-area-grown semiconductor-superconductor hybrids: A basis for topological networks“. In: *Physical review letters* 121.14 (2018), p. 147701.

[102] GLR Anselmetti *et al.* „End-to-end correlated subgap states in hybrid nanowires“. In: *Physical Review B* 100.20 (2019), p. 205412.

[103] M Fahed *et al.* „Selective area heteroepitaxy of GaSb on GaAs (001) for in-plane InAs nanowire achievement“. In: *Nanotechnology* 27.50 (2016), p. 505301.

[104] M Fahed *et al.* „Impact of P/In flux ratio and epilayer thickness on faceting for nanoscale selective area growth of InP by molecular beam epitaxy“. In: *Nanotechnology* 26.29 (2015), p. 295301.

[105] Gozde Tutuncuoglu *et al.* „Towards defect-free 1-D GaAs/AlGaAs heterostructures based on GaAs nanomembranes“. In: *Nanoscale* 7.46 (2015), pp. 19453–19460.

[106] Joon Sue Lee *et al.* „Selective-area chemical beam epitaxy of in-plane InAs one-dimensional channels grown on InP (001), InP (111) B, and InP (011) surfaces“. In: *Physical Review Materials* 3.8 (2019), p. 084606.

[107] G Bacchin and T Nishinaga. „Dependence of the degree of selectivity on the Al content during the selective area growth of AlGaAs on GaAs (0 0 1) by PSE/MBE“. In: *Journal of crystal growth* 191.4 (1998), pp. 599–606.

[108] Michael Wimmer *et al.* „Quantum point contact as a probe of a topological superconductor“. In: *New Journal of Physics* 13.5 (2011), p. 053016.

[109] Karsten Flensberg. „Tunneling characteristics of a chain of Majorana bound states“. In: *Physical Review B* 82.18 (2010), p. 180516.

[110] Z Yang *et al.* „Revealing large-scale homogeneity and trace impurity sensitivity of GaAs nanoscale membranes“. In: *Nano Letters* 17.5 (2017), pp. 2979–2984.

[111] M Fahed *et al.* „Threading dislocation free GaSb nanotemplates grown by selective molecular beam epitaxy on GaAs (001) for in-plane InAs nanowire integration“. In: *Journal of Crystal Growth* 477 (2017), pp. 45–49.

[112] Pavel Aseev *et al.* „Ballistic InSb nanowires and networks via metal-sown selective area growth“. In: *Nano letters* 19.12 (2019), pp. 9102–9111.

[113] Roy LM Op het Veld *et al.* „In-plane selective area InSb–Al nanowire quantum networks“. In: *Communications Physics* 3.1 (2020), pp. 1–7.

[114] Takeyoshi Sugaya, Yoshitaka Okada, and Mitsuo Kawabe. „Selective growth of GaAs by molecular beam epitaxy“. In: *Japanese journal of applied physics* 31.6A (1992), p. L713.

[115] A Okamoto and K Ohata. „Substrate temperature lowering in GaAs selective epitaxial growth by molecular-beam epitaxy“. In: *Journal of applied physics* 66.7 (1989), pp. 3413–3415.

[116] Peter Krogstrup *et al.* „Advances in the theory of III–V nanowire growth dynamics“. In: *Journal of Physics D: Applied Physics* 46.31 (2013), p. 313001.

[117] JH Neave *et al.* „Dynamics of film growth of GaAs by MBE from RHEED observations“. In: *Applied Physics A* 31.1 (1983), pp. 1–8.

[118] L Däweritz and R Hey. „Reconstruction and defect structure of vicinal GaAs (001) and AlxGa1- xAs (001) surfaces during MBE growth“. In: *Surface Science* 236.1-2 (1990), pp. 15–22.

[119] A Guillén-Cervantes *et al.* „GaAs surface oxide desorption by annealing in ultra high vacuum“. In: *Thin Solid Films* 373.1-2 (2000), pp. 159–163.

[120] Takuji Yamamura *et al.* „Influence of anisotropic diffusion of Ga atoms on GaAs growth on alternately inverted (100) substrates“. In: *Japanese journal of applied physics* 44.11L (2005), p. L1397.

[121] JL Roehl *et al.* „Binding sites and diffusion barriers of a Ga adatom on the GaAs (001)- c (4$\times$ 4) surface from first-principles computations“. In: *Physical Review B* 82.16 (2010), p. 165335.

[122] Marcin Mińkowski and Magdalena A Załuska–Kotur. „Diffusion of Ga adatoms at the surface of GaAs (001) c (4$\times$ 4) α and β reconstructions“. In: *Physical Review B* 91.7 (2015), p. 075411.

[123] E Tournie *et al.* „Surfactant-mediated molecular-beam epitaxy of III–V strained-layer heterostructures“. In: *Journal of crystal growth* 150 (1995), pp. 460–466.

[124] Chan Wuk Oh, Eunja Kim, and Young Hee Lee. „Kinetic role of a surfactant in island formation“. In: *Physical review letters* 76.5 (1996), p. 776.

[125] A Okamoto. „Selective epitaxial growth by molecular beam epitaxy“. In: *Semiconductor science and technology* 8.6 (1993), p. 1011.

[126] Taketomo Sato, Isao Tamai, and Hideki Hasegawa. „Growth kinetics and modeling of selective molecular beam epitaxial growth of GaAs ridge quantum wires on pre-patterned nonplanar substrates“. In: *Journal of Vacuum Science & Technology B: Microelectronics and Nanometer Structures Processing, Measurement, and Phenomena* 22.4 (2004), pp. 2266–2274.

[127] Maria Tchernycheva *et al.* „Au-assisted molecular beam epitaxy of InAs nanowires: Growth and theoretical analysis“. In: *Journal of Applied Physics* 102.9 (2007), p. 094313.

[128] Sergio Bietti *et al.* „Gallium surface diffusion on GaAs (001) surfaces measured by crystallization dynamics of Ga droplets“. In: *Journal of Applied Physics* 116.11 (2014), p. 114311.

[129] Theodore L Einstein. „Equilibrium shape of crystals“. In: *Handbook of Crystal Growth*. Elsevier, 2015, pp. 215–264.

[130] H Heinecke, M Wachter, and U Schöffel. „Facet formation and characterization of III–V structures grown on patterned surfaces“. In: *Microelectronics journal* 28.8-10 (1997), pp. 803–815.

[131] Karl Eberl, Pierre M Petroff, and Piet Demeester. *Low dimensional structures prepared by epitaxial growth or regrowth on patterned substrates*. Vol. 298. Springer Science & Business Media, 2012.

[132] I Eisele, H Baumgärtner, and W Hansch. „Self-Assembling Growth of Silicon Nanostructures with Micro Shadow Masks“. In: *Low Dimensional Structures Prepared by Epitaxial Growth or Regrowth on Patterned Substrates*. Springer, 1995, pp. 161–172.

[133] H Fujikura and H Hasegawa. „Fabrication of InP-based InGaAs ridge quantum wires utilizing selective molecular beam epitaxial growth on (311) A facets“. In: *Journal of electronic materials* 25.5 (1996), pp. 619–625.

[134] Xu-Qiang Shen, Daisuke Kishimoto, and Tatau Nishinaga. „Arsenic pressure dependence of surface diffusion of Ga on nonplanar GaAs substrates“. In: *Japanese journal of applied physics* 33.1R (1994), p. 11.

[135] Daniel Kandel and Efthimios Kaxiras. „Surfactant mediated crystal growth of semiconductors“. In: *Physical review letters* 75.14 (1995), p. 2742.

[136] Thomas F Kuech. „Surfactants in semiconductor epitaxy“. In: *AIP Conference Proceedings*. Vol. 916. 1. American Institute of Physics. 2007, pp. 288–306.

[137] CY Fong *et al.* „Surfactant-mediated growth of semiconductor materials“. In: *Modelling and Simulation in Materials Science and Engineering* 10.5 (2002), R61.

[138] Bert Voigtländer *et al.* „Modification of growth kinetics in surfactant-mediated epitaxy“. In: *Physical Review B* 51.12 (1995), p. 7583.

[139] RH Miwa *et al.* „Adsorption and dimer exchange processes in surfactant-mediated epitaxial growth of GaAs/InAs“. In: *Surface science* 415.1-2 (1998), pp. 20–28.

[140] Tobias Særkjær *et al.* „Collective formation of misfit dislocations at the critical thickness“. In: *arXiv preprint arXiv:2102.03587* (2021).

[141] Benjamin D Woods, Sankar Das Sarma, and Tudor D Stanescu. „Charge impurity effects in hybrid Majorana nanowires“. In: *arXiv preprint arXiv:2103.06880* (2021).

[142] Jay D Sau, Sumanta Tewari, and S Das Sarma. „Experimental and materials considerations for the topological superconducting state in electron-and hole-doped semiconductors: Searching for non-Abelian Majorana modes in 1D nanowires and 2D heterostructures“. In: *Physical Review B* 85.6 (2012), p. 064512.

[143] Seongjin Ahn *et al.* „Estimating disorder and its adverse effects in semiconductor Majorana nanowires“. In: *arXiv preprint arXiv:2109.00007* (2021).

[144] Loren Pfeiffer *et al.* „Electron mobilities exceeding 10 7 cm2/V s in modulation-doped GaAs“. In: *Applied Physics Letters* 55.18 (1989), pp. 1888–1890.

[145] Jin-Peng Xu *et al.* „Experimental detection of a Majorana mode in the core of a magnetic vortex inside a topological insulator-superconductor Bi 2 Te 3/NbSe 2 heterostructure“. In: *Physical review letters* 114.1 (2015), p. 017001.

[146] Hao Zhang *et al.* „Quantized majorana conductance“. In: *Nature* 556.7699 (2018), pp. 74–79.

[147] Hao Zhang *et al.* „Retraction note: Quantized majorana conductance“. In: *Nature* 591.7851 (2021), E30–E30.

[148] Paolo Giannozzi *et al.* „QUANTUM ESPRESSO: a modular and open-source software project for quantum simulations of materials“. In: *Journal of physics: Condensed matter* 21.39 (2009), p. 395502.

[149] Paolo Giannozzi *et al.* „Advanced capabilities for materials modelling with Quantum ESPRESSO“. In: *Journal of physics: Condensed matter* 29.46 (2017), p. 465901.

[150] C Stampfl and Chris G Van de Walle. „Energetics and electronic structure of stacking faults in AlN, GaN, and InN“. In: *Physical Review B* 57.24 (1998), R15052.

[151] JW Matthews. „Defects associated with the accommodation of misfit between crystals“. In: *Journal of Vacuum Science and Technology* 12.1 (1975), pp. 126–133.

[152] Jan H Van der Merwe. „Misfit dislocation generation in epitaxial layers“. In: *Critical Reviews in Solid State and Material Sciences* 17.3 (1991), pp. 187–209.

[153] Lars Vegard. „Die konstitution der mischkristalle und die raumfüllung der atome“. In: *Zeitschrift für Physik* 5.1 (1921), pp. 17–26.

[154] M Gandais *et al.* „Dislocation contrast by transmission electron microscopy A method for Burgers vector characterization if the invisibility criterion is not valid“. In: *Philosophical Magazine A* 45.3 (1982), pp. 387–400.

[155] Yadira Arroyo Rojas Dasilva *et al.* „Structural defects in cubic semiconductors characterized by aberration-corrected scanning transmission electron microscopy“. In: *Ultramicroscopy* 176 (2017), pp. 11–22.

[156] Nicolas Bologna *et al.* „Stair-rod dislocation cores acting as one-dimensional charge channels in GaAs nanowires“. In: *Physical Review Materials* 2.1 (2018), p. 014603.

[157] GR Booker *et al.* „Some comments on the interpretation of the 'kikuchi-like reflection patterns' observed by scanning electron microscopy“. In: *The Philosophical Magazine: A Journal of Theoretical Experimental and Applied Physics* 16.144 (1967), pp. 1185–1191.

[158] DG Coates. „Kikuchi-like reflection patterns obtained with the scanning electron microscope“. In: *The Philosophical Magazine: A Journal of Theoretical Experimental and Applied Physics* 16.144 (1967), pp. 1179–1184.

[159] G Naresh-Kumar *et al.* „Rapid nondestructive analysis of threading dislocations in wurtzite materials using the scanning electron microscope“. In: *Physical review letters* 108.13 (2012), p. 135503.

[160] G Naresh-Kumar *et al.* „Electron channeling contrast imaging studies of nonpolar nitrides using a scanning electron microscope“. In: *Applied Physics Letters* 102.14 (2013), p. 142103.

[161] Han Han *et al.* „Application of electron channeling contrast imaging to 3D semiconductor structures through proper detector configurations“. In: *Ultramicroscopy* 210 (2020), p. 112928.

[162] Joseph I Goldstein *et al. Scanning electron microscopy and X-ray microanalysis*. Springer, 2017, pp. 15–37.

[163] T Koshikawa and R Shimizu. „A Monte Carlo calculation of low-energy secondary electron emission from metals“. In: *Journal of Physics D: Applied Physics* 7.9 (1974), p. 1303.

[164] David C Joy, Dale E Newbury, and David L Davidson. „Electron channeling patterns in the scanning electron microscope“. In: *Journal of Applied Physics* 53.8 (1982), R81–R122.

[165] Ivo Konvalina and Ilona Müllerová. „The trajectories of secondary electrons in the scanning electron microscope“. In: *Scanning* 28.5 (2006), pp. 245–256.

[166] Han Han *et al.* „Enhancing the defect contrast in ECCI through angular filtering of BSEs“. In: *Ultramicroscopy* 210 (2020), p. 112922.

[167] A Vilalta-Clemente *et al.* „Cross-correlation based high resolution electron backscatter diffraction and electron channelling contrast imaging for strain mapping and dislocation distributions in InAlN thin films“. In: *Acta Materialia* 125 (2017), pp. 125–135.

[168] C Trager-Cowan *et al.* „Advances in electron channelling contrast imaging and electron backscatter diffraction for imaging and analysis of structural defects in the scanning electron microscope“. In: *IOP Conference Series: Materials Science and Engineering*. Vol. 891. 1. IOP Publishing. 2020, p. 012023.

[169] C Trager-Cowan *et al.* „Electron backscatter diffraction and electron channeling contrast imaging of tilt and dislocations in nitride thin films“. In: *Physical Review B* 75.8 (2007), p. 085301.

[170] Thermofisher. *Scanning electron Microscope: Verios 5 XHR: Thermo Fisher scientific - US*. Sept. 2020. URL: https://www.thermofisher.com/dk/en/home/electron-microscopy/products/scanning-electron-microscopes/verios-xhr-sem.html#specifications.

[171] Ch Schetelich, S Weber, and V Geist. „Dynamical X-Ray Diffraction at Decagonal Quasicrystals Observed by the Kossel Technique“. In: *physica status solidi (a)* 145.1 (1994), pp. 51–59.

[172] Ch Schetelich and V Geist. „Observation of X-Ray Kossel Patterns (“Gitterquelleninterferenzen”) from Quasicrystals“. In: *physica status solidi (a)* 136.2 (1993), pp. 283–289.

[173] Tadashi Otaka *et al. Electron beam apparatus*. US Patent 5,412,209. May 1995.

[174] Akira Yoshida, Yutaka Kaburagi, and Yoshihiro Hishiyama. „Chapter 5 - Scanning Electron Microscopy“. In: *Materials Science and Engineering of Carbon*. Ed. by Michio Inagaki and Feiyu Kang. Butterworth-Heinemann, 2016, pp. 71–93. ISBN: 978-0-12-805256-3. DOI: https://doi.org/10.1016/B978-0-12-805256-3.00005-2.

[175] Zhifeng Shao. „Extraction of secondary electrons in a newly proposed immersion lens“. In: *Review of scientific instruments* 60.4 (1989), pp. 693–699.

[176] Brendan J Griffin. „A comparison of conventional Everhart-Thornley style and in-lens secondary electron detectors—a further variable in scanning electron microscopy“. In: *Scanning* 33.3 (2011), pp. 162–173.

[177] I Müllerová and I Konvalina. „Collection of secondary electrons in scanning electron microscopes“. In: *Journal of microscopy* 236.3 (2009), pp. 203–210.

[178] Ivo Konvalina *et al.* „In-lens band-pass filter for secondary electrons in ultrahigh resolution SEM“. In: *Materials* 12.14 (2019), p. 2307.

[179] Linda E Franken *et al.* „A Technical Introduction to Transmission Electron Microscopy for Soft-Matter: Imaging, Possibilities, Choices, and Technical Developments“. In: *Small* 16.14 (2020), p. 1906198.

[180] Thermofisher Scientific. *FIB SEM Software: AutoScript 4 Software: Thermo FISHER scientific - US*. 2021. URL: https://www.thermofisher.com/dk/en/home/electron-microscopy/products/software-em-3d-vis/autoscript-4-software.html#features.

[181] Sankar Das Sarma and Haining Pan. „Disorder-induced zero-bias peaks in Majorana nanowires“. In: *Physical Review B* 103.19 (2021), p. 195158.

[182] Vivaldo Leiria Campo Jr and Matteo Cococcioni. „Extended DFT+ U+ V method with on-site and inter-site electronic interactions“. In: *Journal of Physics: Condensed Matter* 22.5 (2010), p. 055602.